eISSN 2234-2591

Ewha Medical Journal

Vol. 49, No. 3, 2026

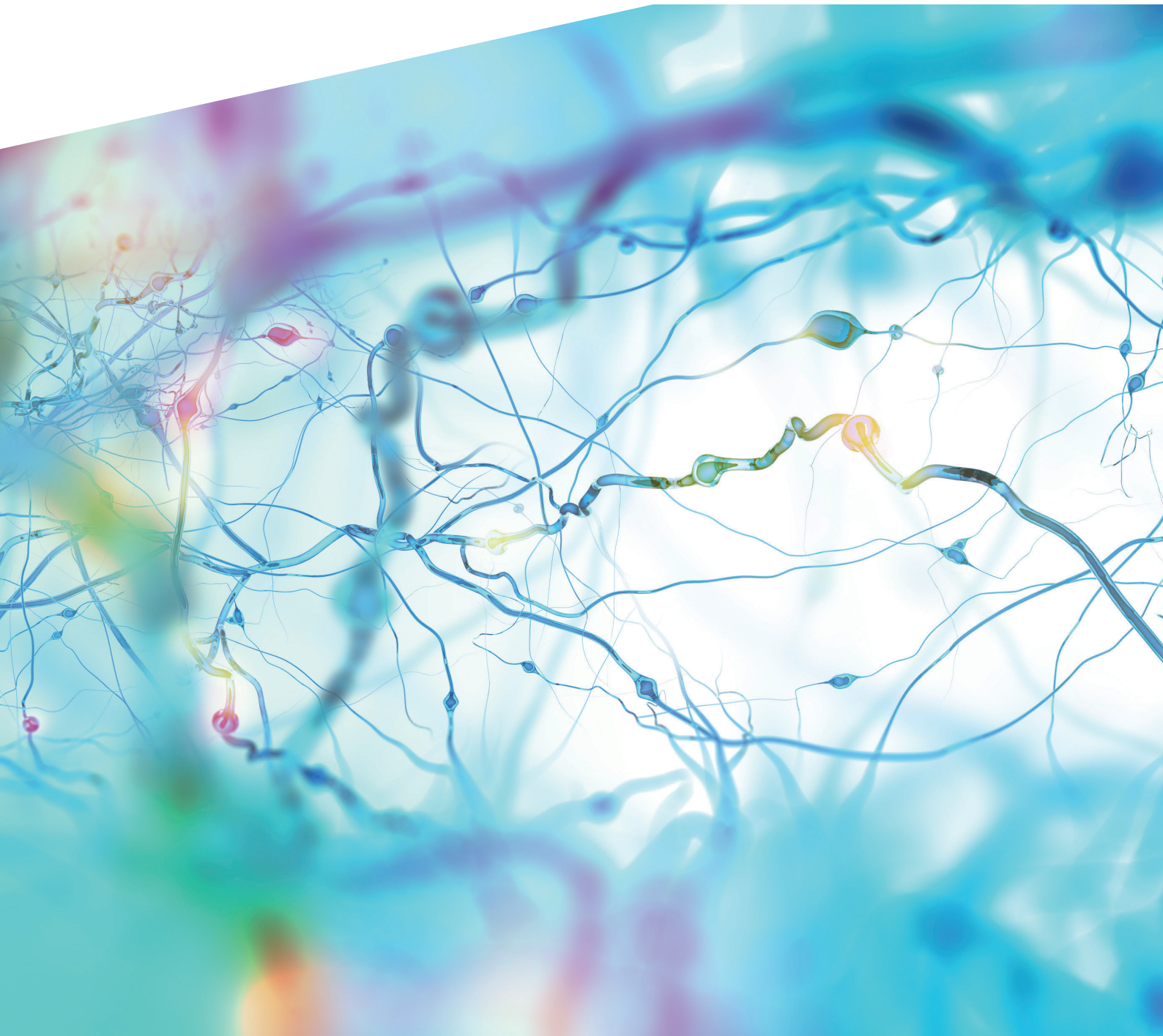

Ewha Medical Journal

eISSN 2234-2591

Vol. 49, No. 3, July 2026

Aims & scope

Aims

Ewha Medical Journal aims to provide medical professionals with essential healthcare information and fundamental medical knowledge. The journal will contribute to improving and serving human society based on the Christian values of education, truth, goodness, and beauty. Additionally, the journal strives to nurture young editors, enabling them to demonstrate exceptional women's editorial leadership and provide innovative learning methods.

Scope

Its scope includes:

- Up-to-date medical knowledge and skills essential for patient care
- Preparing for the future of medicine
- Effective interprofessional communication
- Ensuring gender equity and diversity
- Medical education materials
- Sharing data and protocols

Regional scope

The journal primarily focuses on Korea but welcomes submissions from researchers worldwide.

Copyright & Open access policy

Publisher Ewha Womans University College of Medicine
Editor-in-Chief Ji Yeon Byun

Published by Ewha Womans University College of Medicine and Ewha Medical Research Institute
25, Magokdong-ro 2-gil, Gangseo-gu, Seoul 07804, Korea
Tel: +82-2-6986-6094, Fax: +82-2-6986-7026, E-mail: editor@e-emj.org

Editorial office Ewha Medical Research Institute
25, Magokdong-ro 2-gil, Gangseo-gu, Seoul 07804, Korea
Tel: +82-2-6986-6094, Fax: +82-2-6986-7026, E-mail: editor@e-emj.org

Printing correspondence by M2PI
#805, 26 Sangwon 1-gil, Seongdong-gu, Seoul 04779, Korea
Tel: +82-2-6966-4930, Fax: +82-2-6966-4945, E-mail: support@m2-pi.com

· The subscription is free. For inquiries, please contact the editorial office (Tel: +82-2-6986-6094, E-mail: editor@e-emj.org). All the contents are also available at the EMJ website (https://www.e-emj.org).

Editorial board

eISSN 2234-2591

Contents

Ewha Medical Journal

Vol. 49, No. 3, July 2026

eISSN: 2234-2591
Open Access

Editorial

Ewha Med J 2026;49(3):e17
https://doi.org/10.12771/emj.2026.01508

The Ewha Medical Journal

In this issue: July 2026

Ji Yeon Byun *

Department of Dermatology, Ewha Womans University College of Medicine, Seoul, Korea

The articles in this issue of the *Ewha Medical Journal* address vaccine safety, artificial intelligence (AI), perioperative pain management, rare tumors, procedural complications, and diagnostic imaging. Together, they highlight the importance of clinical vigilance and the responsible integration of innovation into patient care.

"SKYVaricella (a live attenuated varicella vaccine) safety issues revisited" examines concerns regarding herpes zoster following administration of a live attenuated varicella vaccine developed in Korea. The article emphasizes the need for timely pharmacovigilance, transparent communication, and continuous reassessment of vaccine benefits and risks.

"Clinical phenotypes and clustering patterns of human toxocariasis in PubMed-indexed case reports" presents an AI-assisted systematic scoping review. It illustrates how AI can support literature screening, data extraction, and pattern recognition in evidence synthesis, while reaffirming that such AI-generated outputs require methodological transparency and careful human verification.

A randomized study evaluates ultrasound-guided bilateral rectus sheath block after robotic single-site gynecologic surgery. The technique reduced early postoperative pain and rescue fentanyl use, supporting its role in multimodal perioperative analgesia.

Two case reports illustrate the diagnostic challenges posed by rare malignancies. A report of primary breast leiomyosarcoma emphasizes the integration of histopathologic and immunohistochemical findings to distinguish this uncommon tumor from other spindle-cell neoplasms. Another describes appendiceal mucinous adenocarcinoma presenting as bilateral ovarian masses and mimicking advanced ovarian cancer, highlighting the importance of considering a gastrointestinal primary in bilateral ovarian mucinous tumors.

A case of pneumocephalus with suspected cerebrospinal fluid leakage after epiduroscopic epidural neuroplasty illustrates an uncommon procedural complication. The persistent headache and its subsequent improvement after an epidural blood patch suggested occult dural injury, reminding clinicians to consider intracranial complications following epidural procedures.

"Unrecognized tooth aspiration mimicking a hilar lesion in a patient with COVID-19 pneumonia" illustrates how the attribution of persistent hypoxemia and asymmetric breath sounds to viral pneumonia delayed the recognition of an aspirated tooth causing bronchial obstruction. The case provides an instructive example of anchoring bias and offers valuable radiologic and clinical lessons, particularly because the aspirated tooth mimicked a hilar lesion on chest imaging.

Finally, "Artificial intelligence as a pragmatic adjunct to molecular classification in endometrial cancer" considers AI-assisted histopathologic assessment where comprehensive molecular testing is limited. Such approaches require external validation, standardized workflows, and appropriate clinical oversight.

Collectively, these articles demonstrate that medical progress requires both innovation and scrutiny. Emerging technologies and clinical techniques must be rigorously evaluated, while careful observation and diagnostic openness remain fundamental to safe and effective patient care.

ORCID

Ji Yeon Byun: https://orcid.org/0000-0003-4519-9474

*Corresponding email: jybyun@ewha.ac.kr
Received: July 21, 2026 Accepted: July 21, 2026

Authors' contribution

All work was completed by Ji Yeon Byun.

Conflict of interest

Ji Yeon Byun has served as the editor of the *Ewha Medical Journal* since January 2026. However, she was not involved in the peer review process or decision-making for this article. No other potential conflicts of interest relevant to this article were reported.

Funding

None.

Data availability

Not applicable.

Acknowledgments

None.

Supplementary materials

None.

eISSN: 2234-2591
Open Access

Opinion

Ewha Med J 2026;49(3):e18
https://doi.org/10.12771/emj.2026.01263

The Ewha Medical Journal

SKYVaricella (a live attenuated varicella vaccine) safety issues revisited

Joowon Lee*

Infectious Disease Control Division, Citizens' Health Bureau, Seoul Metropolitan Government, Seoul, Korea

Context

SKYVaricella is a live attenuated varicella-zoster virus vaccine, developed by the Korean manufacturer, SK Bioscience. The Ministry of Food and Drug Safety (MFDS) first approved it in 2018, and the World Health Organization (WHO) granted prequalification in 2019. It is currently one of 4 WHO prequalified varicella vaccines. In its phase 3 trial, the vaccine demonstrated immunogenicity non-inferior to Varivax, but it has not been evaluated for protective efficacy, durability of immune response, long-term safety beyond 26 weeks, or adverse events occurring in fewer than 1 in 330 recipients [1].

A reported fatal case of disseminated vaccine-virus varicella in a SKYVaricella-vaccinated child prompted a joint safety assessment by the Korea Disease Control and Prevention Agency (KDCA) and the MFDS in 2024 [2]. The agencies concluded that SKYVaricella did not cause the fatal case and that no immediate safety concern warranted removal from the National Immunization Program (NIP) [3]. However, they identified an increased risk of herpes zoster (HZ) in SKYVaricella-vaccinated children. They announced plans to strengthen risk management, but no detailed risk minimizing actions or follow-up updates in benefit-risk assessment have been released.

SK Bioscience updated the vaccine's risk management plan (RMP) in August 2024. The revision removed most of misclassified safety concerns from the initial RMP and added HZ as an important potential risk [4,5]. It also introduced educational materials for patients and physicians as additional risk minimization measures (RMMs), although the materials did not describe HZ characteristics in vaccinated children [6]. Despite acknowledging the new safety concern in the RMP, the manufacturer has not properly updated the product information and continues to assert that no new safety concern exists [7].

Since the KDCA and MFDS press briefing, new evidence has emerged. Kim et al. [8] reported a case series of 23 children who developed HZ after SKYVaricella vaccination between February 2021 and March 2024; 43.4% required hospitalization. At the population level, Lee [9] conducted an ecological study using Korean National Health Insurance Service data and estimated 6,484 excess HZ cases potentially due to SKYVaricella vaccination in Korean children under 5 years of age from January 2019 to June 2024. Although these studies describe the frequency, seriousness, and public health impact of HZ in this population, Korean authorities have not commented on the findings, and it remains unclear whether they have re-evaluated the vaccine's risk-benefit profile in light of this new information.

Objective

Korean authorities and the manufacturer appear to have publicly denied—or only ambiguously acknowledged—the emerging safety concern of HZ [3,7]. Despite this, they have initiated new studies to evaluate the HZ risk associated with SKYVaricella. This article reviews those studies and examines their implications for managing SKYVaricella-related HZ risk.

Overview of the risk management process and SKYVaricella

Medicinal products receive regulatory approval once they demonstrate sufficient safety data to support a favorable risk-benefit balance for their intended indications. After commercial

*Corresponding email: joowon.lee@seoul.go.kr
Received: March 27, 2026 Accepted: April 20, 2026

launch, additional safety data accumulate through routine use and expansion of indications. Because these data are large in volume and diverse in type, regulators and manufacturers apply predefined thresholds or criteria to screen for potential issues. Safety information that meets these criteria is flagged as a "signal" for further assessment. When an in-depth evaluation suggests a reasonable causal association between a signal and a medicinal product, the detected signal is classified as an identified or potential risk. If this risk is considered significant in terms of impact on public health or on individuals, it is designated as an important identified risk or an important potential risk. Important identified or important potential risks are defined as safety concerns [10,11].

Risk management for medicinal products focuses on safety concerns, which are the primary drivers of a product's risk-benefit balance. When available information sufficiently characterizes a safety concern, routine (e.g., changes to product information) RMMs alone or a combination of routine and additional (e.g., dear healthcare professional letter) RMMs are implemented. When available information is insufficient to characterize a safety concern and proper risk management is therefore not feasible, additional pharmacovigilance activities (e.g., clinical trials, epidemiological studies) are required to collect further data alongside the implementation of RMMs (Fig. 1) [10].

The risk management approach for SKYVaricella is inconsistent. Regulators and the manufacturer acknowledged an increased HZ risk but denied that it constitutes a new safety concern [3,7]. The manufacturer introduced educational materials as additional RMMs but omitted essential information (i.e., information recommended by good pharmacovigilance guidelines) about HZ risk [6,12], and it did not update the product information [13], which is a routine RMM. At the same time, the regulatory authorities and manufacturer initiated 3 studies that probably function as additional pharmacovigilance activities, despite their official position that HZ is not a safety concern.

Review of new SKYVaricella studies

In November 2024, the KDCA issued a call for proposals for an outsourced research project titled "Investigation of the characteristics of children with herpes zoster in Korea for vaccine safety analysis." Korea University was selected to conduct the study, which was scheduled for completion in December 2025, but no results have been released [14]. In January 2026, researchers published the cohort profile of the Korean Varicella Immunization Monitoring Scheme. The paper described a national cohort designed to monitor the long-term effectiveness of varicella vaccines in the NIP and noted that long-term effects on HZ incidence would be evaluated in the future. The KDCA provided raw data and research funding for this publication. The study used varicella vaccination record data from the National Immunization Registry (NIR) maintained by the KDCA and varicella infection event

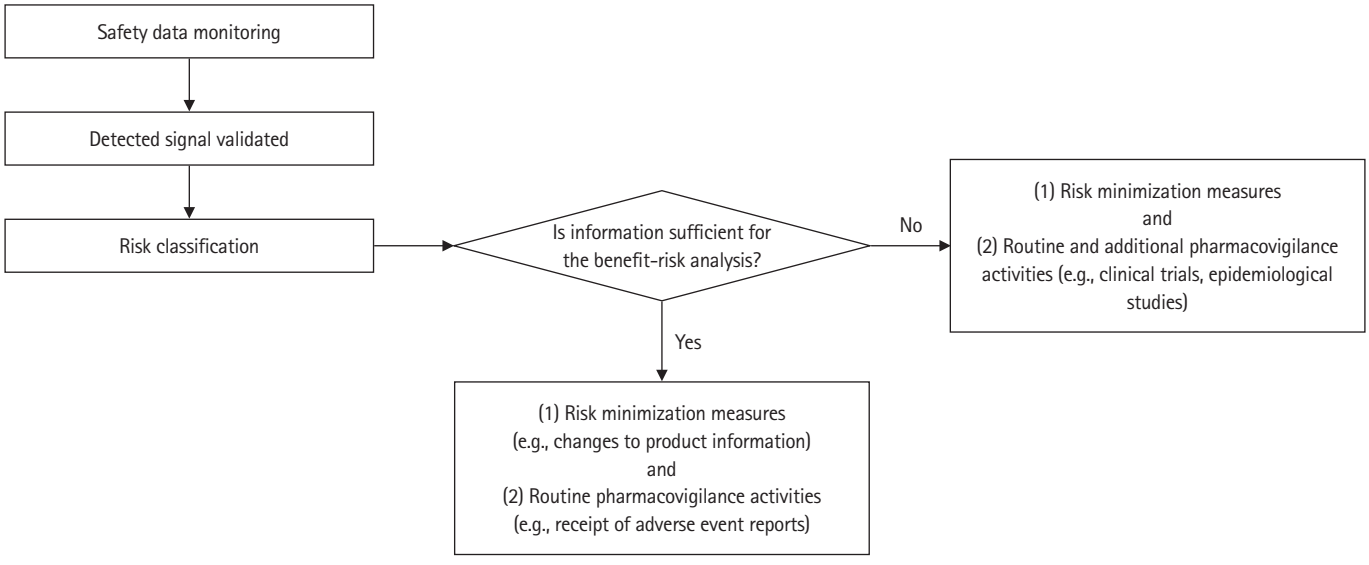

Fig. 1. Risk management flow per the International Council for Harmonisation of Technical Requirements for Pharmaceuticals for Human Use and Good Pharmacovigilance Practices guidelines. This figure summarizes the overall risk management process from safety data monitoring to risk minimization activities and pharmacovigilance activities. Once a detected signal is assessed as valid, it qualifies as either an identified or potential risk. For important identified or important potential risks, appropriate risk minimization activities are implemented to maintain a favorable risk-benefit balance of a medicinal product. When available information is insufficient to characterize these risks, additional pharmacovigilance activities such as clinical trials or epidemiological studies are required to collect more safety information.

data from the Health Insurance Review and Assessment Service (HIRA). Varicella infection events were retrieved using the International Classification of Diseases, 10th Revision (ICD-10) code B01.x. All datasets were linked at the individual level [15]. The manufacturer also launched a company-sponsored phase 3 clinical trial (ClinicalTrials.gov registration number NCT07415252) to compare the immunogenicity of the lower-potency versions of SKYVaricella with that of Varivax. In the trial, the 2 investigational products are defined as mid- and low-potency versions of SKYVaricella [16]. Although SK Bioscience stated that the trial aims to support a 2-dose regimen of SKYVaricella for global market expansion [17], the current dose of SKYVaricella is not being studied for its immunogenicity as a 2-dose regimen in the trial (Table 1).

These 3 studies reveal several aspects of the Korean authorities' and manufacturer's risk management approach: First, implicit acknowledgement of the risk. Despite official denials, commissioning multiple safety studies for a domestically developed product seems unprecedented in Korean regulatory history and suggests recognition of the issue's significance. Second, a delayed assessment. The cohort study will evaluate HZ risk in the future [15], even though 7 years of follow-up data for SKYVaricella-vaccinated children already exist. Similar to the cohort study using varicella infection event data, HZ risk can be evaluated using data from the NIR and the 7-year HZ event data from the HIRA, which can be retrieved using the ICD-10 code B02.x. In addition, the phase 3 trial will collect HZ data for 15 months after vaccination, but given the expected incidence rate (i.e., 14 cases per 100,000 person-years for Varivax), HZ onset time after vaccination (i.e., the median onset after vaccination was 605 days for disseminated skin HZ and 260 days for localized HZ), and sample size (i.e., 780 subjects), the total number of HZ cases will be too small to support meaningful comparisons (all SKYVaricella groups would be 2 or fewer, and the Varivax group would be less than 1) [8,16,18]. Third, a potential dose modification. The manufacturer appears to be pursuing a lower-potency formulation, similar to the Suduvax and Barycela sequence, in which a higher-titer version of Suduvax was developed after concerns about its low effectiveness [9,19,20]. SKYVaricella's current dose demonstrated adequate immunogenicity and acceptable safety in its pivotal trial, making a dose-modification trial without a formal regulatory reassessment unusual.

In summary, the regulatory authorities and manufacturer appear to be delaying a clear evaluation of HZ risk while simultaneously developing a lower-titer version of SKYVaricella.

Table 1. Studies launched or planned after the emergence of SKYVaricella safety issues

No.	Study title	Primary study objective	HZ-related objective	Study funder	Study period
1	Investigation of the characteristics of children with HZ in Korea for vaccine safety analysis	Analysis of the origins of varicella-zoster virus in children with HZ, comparison of clinical characteristics by origin, collection of clinical specimens of HZ and genomic analysis	Primary objectives are HZ-related.	The KDCA is a funder and Korea University has conducted the study.	The study period was supposed to be from December 18, 2024 to December 17, 2025. Study results have not been published yet.
2	Cohort profile: Korean Varicella Immunization Monitoring (K-VIM) Scheme: a national cohort of children born 2011–2022	To assess the long-term effectiveness of the current varicella vaccines in the NIP and to evaluate the real-world impact of 1-dose versus 2-dose vaccination schedules	To evaluate potential long-term effects on HZ incidence in the vaccinated cohort.	The KDCA provided the raw data and research funding. Authors were researchers in Korea University.	The cohort profile introduction was published on January 22, 2026. A future study plan has not been disclosed.
3	A phase III, randomized, double-blinded, active-controlled, multinational, multicenter study to assess the safety and immunogenicity of a 2-dose regimen of SKYVaricella (NBP608) in children aged 12 months to 12 years	Immunogenicity comparisons between mid and low-potency versions of SKYVaricella and Varivax	HZ is designated as an adverse event of special interest and will be monitored for 15 months after the first vaccination.	SK Bioscience is a study funder and sponsor.	The study is planned from June 5, 2026 to January 2, 2028.

The table summarizes studies launched or planned by Korean authorities or the manufacturer after the emergence of SKYVaricella safety issues, probably aiming to collect additional herpes zoster risk information.
HZ, herpes zoster; KDCA, Korea Disease Control and Prevention Agency; NIP, National Immunization Program.

Conclusion

The new studies initiated by Korean regulatory authorities and the manufacturer following the emergence of safety concerns about SKYVaricella reflect an effort to collect additional data on HZ in the SKYVaricella-vaccinated population. These studies could represent a positive step toward addressing the newly identified risk. However, because the stakeholders have not implemented appropriate RMMs for several years—and because the ongoing studies will not yield meaningful data in the near term—significant concerns remain. The new phase 3 clinical trial, in particular, requires scrutiny, as pursuing a 2-dose regimen is difficult to justify for a vaccine lacking evidence of protective efficacy and of durable immunogenicity.

Effective management of the emerging HZ risk associated with SKYVaricella should include the following actions: (1) Base continued inclusion in the NIP on a valid, updated risk-benefit analysis. (2) Disclose detailed information about the HZ risk transparently and promptly. (3) Ensure consistency across routine RMMs, additional RMMs, and additional pharmacovigilance activities. (4) Implement corrective and preventive actions to reduce similar future cases and minimize public health impact, thereby strengthening Korea's vaccine safety management system.

ORCID

Joowon Lee: https://orcid.org/0009-0005-7015-8238

Authors' contribution

Conceptualization: JWL. Methodology/formal analysis/validation: JWL. Project administration: JWL. Writing–original draft: JWL. Writing–review & editing: JWL.

Conflict of interest

No potential conflict of interest relevant to this article was reported.

Funding

None.

Data availability

Not applicable.

Acknowledgments

None.

Supplementary materials

None.

References

1. Ministry of Food and Drug Safety. Approval report for a biological medicinal product (SKYVaricella) [Internet]. SK Bioscience; 2018 [cited 2026 Mar 21]. Available from: https://nedrug.mfds.go.kr/pbp/CCBBB01/getItemDetailCache?cacheSeq=201802323aupdateTs2024-05-17%2009:20:08.0b
2. Kang HM, Kang KR, Kim YJ, Kang JH, Lee SY. A booster administration of the OKA/SK strain causes fatal disseminated varicella in an immunocompetent child. J Med Virol 2023;95:e29108. https://doi.org/10.1002/jmv.29108
3. Korea Disease Control and Prevention Agency (KDCA); Ministry of Food and Drug Safety. Announcement of joint public-private investigation results on the safety of varicella vaccine [Internet]. KDCA; 2024 [cited 2026 Mar 21]. Available from: https://www.kdca.go.kr/kdca/2848/subview.do?enc=Zm5jdDF8QEB8JTJGYmJzJTJGa2RjYSUyRjQyJTJGMjE0OTAyJTJGYXJ0Y2xWaWV3LmRvJTNGcGFzc3dvcmQlM0QlMjZyZ3NCZ25kZVN0ciUzRCUyNmZpbmRPcG53cmQlM0QlMjZmaW5kV29yZCUzRCVFQiVBRiVCQyVFQSVCNCU4MCUyNnJnc0VuZGRlU3RyJTNEJTI2ZmluZFR5cGUlM0RzaiUyNmZpbmRDbFNlcSUzRCUyNnBhZ2UlM0QxJTI2
4. SK Bioscience. The summary of the risk management plan [Internet]. SK Bioscience; 2024 [cited 2026 Mar 21]. Available from: https://nedrug.mfds.go.kr/pbp/CCBBB01/getRmpInfo?itemSeq=201802323
5. Lee J. Varicella vaccine safety: absence of evidence is not evidence of absence. J Korean Med Sci 2024;39:e245. https://doi.org/10.3346/jkms.2024.39.e245
6. SK Bioscience. Guidance for healthcare professionals [Internet]. SK Bioscience; 2024 [cited 2026 Apr 12]. Available from: https://nedrug.mfds.go.kr/pbp/CCBBB01/getRmpDownload?itemSeq=201802323&submitListKind=K
7. Kang SG, Kim HY. The importance of accurate communication for public health benefits and commitment to safety monitoring. J Med Virol 2025;97:e70297. https://doi.org/10.1002/jmv.70297
8. Kim YJ, Oh D, Kim J, Son J, Moon JY, Kim YK, Ahn B, Kang KR, Park D, Kang HM. Heightened incidence of adverse events associated with a live attenuated varicella vaccine strain that lacks critical genetic polymorphisms in open reading frame 62. Clin Microbiol Infect 2024;30:1466-1473. https://doi.org/10.1016/j.cmi.2024.08.018
9. Lee J. The impact of a varicella vaccine introduction on the incidence of herpes zoster in Korean children, an ecological study. Infect Dis (Lond) 2026;58:126-133. https://doi.org/10.1080/

23744235.2025.2555896
10. European Medicines Agency (EMA). Guideline on good pharmacovigilance practices (GVP): Module V–risk management systems (Rev. 2) [Internet]. EMA; 2024 [cited 2026 Mar 21]. Available from: https://www.ema.europa.eu/en/documents/scientific-guideline/guideline-good-pharmacovigilance-practices-module-v-risk-management-systems-rev-2_en.pdf
11. Council for International Organizations of Medical Sciences (CIOMS). Practical aspects of signal detection in pharmacovigilance: report of CIOMS Working Group VIII. CIOMS; 2010.
12. European Medicines Agency (EMA). Guideline on good pharmacovigilance practices: Module XV–safety communication (Rev. 1) [Internet]. EMA; 2017 [cited 2026 Apr 12]. Available from: https://www.ema.europa.eu/en/documents/scientific-guideline/guideline-good-pharmacovigilance-practices-module-xv-safety-communication-rev-1_en.pdf
13. SK Bioscience. Product information, SKYVaricella [Internet]. SK Bioscience; 2024 [cited 2026 Apr 12]. Available from: https://nedrug.mfds.go.kr/pbp/CCBBB01/getItemDetailCache?cacheSeq=201802323aupdateTs2026-03-25%2019:36:59.32028b
14. Korea Disease Control and Prevention Agency (KDCA). [Outsourced project] Call for proposals: "Investigation of the characteristics of children with herpes zoster in Korea for vaccine safety analysis" [Internet]. KDCA; 2024 [cited 2026 Mar 21]. Available from: https://www.kdca.go.kr/kdca/2858/subview.do?enc=Zm5jdDF8QEB8JTJGYmJzJTJGa2RjYSUyRjUxJTJGMjI0NTIxJTJGYXJ0Y2xWaWV3LmRvJTNGcGFzc3dvcmQlM0QlMjZyZ3NCZ25kZVN0ciUzRCUyNmZpbmRPcG53cmQlM0QlMjZmaW5kV29yZCUzRCVFQiU4QyU4MCVFQyU4MyU4MSVFRCU4RiVBQyVFQyVBNyU4NCUyNnJnc0VuZGRlU3RyJTNEJTI2ZmluZFR5cGUlM0RzaiUyNmZpbmRDbFNlcSUzRCUyNnBhZ2UlM0QxJTI2
15. Shim YK, Lee YH, Choe YJ, Yoon Y, Kim YK. Cohort profile: Korean Varicella Immunization Monitoring (K-VIM) Scheme: a national cohort of children born 2011-2022. Epidemiol Health 2026;48:e2026005. https://doi.org/10.4178/epih.e2026005
16. SK Bioscience. SkyVaricella (NBP608) vaccine with lower potencies in healthy children aged 12 months to 12 years [Internet]. SK Bioscience; 2026 [cited 2026 Mar 21]. Available from: https://clinicaltrials.gov/study/NCT07415252?intr=nbp608&rank=1
17. SK Bioscience. SK Bioscience submits IND for phase 3 clinical trial of 2-dose varicella vaccine [Internet]. SK Bioscience; 2025 [cited 2026 Apr 12]. Available from: https://www.skbioscience.com/en/news/news_01_01?mode=2&id=319&page=2
18. Merck Sharp & Dohme (UK) Limited. Summary of product characteristics: Varivax [Internet]. Merck; 2026 [cited 2026 Apr 12]. Available from: https://www.medicines.org.uk/emc/product/5582/smpc
19. Lee YH, Choe YJ, Cho SI, Kang CR, Bang JH, Oh MD, Lee JK. Effectiveness of varicella vaccination program in preventing laboratory-confirmed cases in children in Seoul, Korea. J Korean Med Sci 2016;31:1897-1901. https://doi.org/10.3346/jkms.2016.31.12.1897
20. Umit Z, Sahbudak Bal Z, Zeytinoglu A, Gulbahar Aydogan T, Bag O, Guner Ozenen G, Ozkinay F, Kurugol Z. The comparison of seroconversion rates among different varicella vaccines administered Turkish children; MAV/06 and vOka. Hum Vaccin Immunother 2021;17:4190-4193. https://doi.org/10.1080/21645515.2021.1967037

eISSN: 2234-2591
Open Access

Review article

Ewha Med J 2026;49(3):e19
https://doi.org/10.12771/emj.2026.01221

The Ewha Medical Journal

Clinical phenotypes and clustering patterns of human toxocariasis in PubMed-indexed case reports: an Antigravity-assisted systematic scoping review

Eun Hee Ha*

College of Medicine, Hallym University, Chuncheon, Korea

Purpose: This study aimed to characterize co-occurrence patterns, statistical associations, and phenotypic clusters of clinical manifestations reported in human toxocariasis case reports indexed in PubMed from 2005 through 2025, inclusive.

Methods: PubMed-indexed case reports from 2005 through 2025 were identified using the query ("Toxocariasis" OR "Toxocara") AND "Case Reports" [Publication Type] AND 2005:2025[dp] AND ffrft[Filter]. Free full-text articles were retrieved through PubMed Central and other links indexed in PubMed using the ffrft filter. After 7 nonhuman reports and 5 reports without objective diagnostic confirmation were excluded, 139 case reports were included. Antigravity was used to support data extraction, standardization, statistical analysis, and figure generation. Clinical features were mapped to standardized symptom and organ-involvement variables. Pairwise co-occurrence was assessed using 2×2 contingency tables and Fisher's exact test; association strength was measured using Pearson correlation coefficients; and k-means clustering was used to identify distinct clinical phenotypes.

Results: Four principal clusters were identified: subclinical disease, ocular larva migrans, visceral larva migrans, and neurotoxocariasis/multisystemic disease. The ocular larva migrans and visceral larva migrans clusters were largely distinct, whereas ocular features were frequently co-reported in the neurotoxocariasis/multisystemic cluster. Eosinophilia was strongly associated with systemic manifestations, including fever, dyspnea, cough, pruritus, hepatomegaly, headache, and meningitis, but was not significantly associated with ocular features. Neurotoxocariasis-related features, including headache, meningitis, and seizures, clustered closely.

Conclusion: This artificial intelligence-assisted scoping review identified exploratory clinical association and clustering patterns in human toxocariasis case reports. These findings may support clinical awareness, but they require validation in curated clinical datasets before they are used for diagnosis, risk stratification, or practice guidance.

Keywords: Toxocariasis; Parasitology; PubMed; Cluster analysis; Artificial intelligence

Introduction

Background/rationale

Toxocariasis is a prevalent zoonotic parasitosis caused by *Toxocara canis* or *Toxocara cati* infection and can present with diverse clinical manifestations, which may contribute to missed or delayed diagnosis [1]. Although toxocariasis is often asymptomatic, it is traditionally classified into 2 well-defined clinical syndromes: visceral larva migrans, which involves systemic larval migration through major organs, and ocular larva migrans, which specifically affects the eye and optic nerve [2]. In addition to these classical syndromes, individual case reports have described atypical manifestations of toxocariasis, including pleural effusion [3]. Although some studies have examined associations between specific toxocariasis manifestations and related clinical features, large-scale systematic analyses evaluating the broader clinical patterns among classical and atypical manifestations reported in toxocariasis case reports remain limited.

*Corresponding email: 20237117@hallym.ac.kr
Received: February 28, 2026 Revised: June 6, 2026 Accepted: June 10, 2026

Objectives

This study aimed to elucidate correlations and clustering patterns among diverse clinical manifestations reported in toxocariasis case reports indexed in PubMed from 2005 through 2025, inclusive. Specifically, it addressed the following question: What symptoms and organ-involvement patterns are reported in toxocariasis case reports, and how do they cluster?

Methods

Ethics statement

This was a literature-based study; therefore, institutional review board approval and informed consent were not required.

Study design

This systematic scoping review was reported in accordance with the Preferred Reporting Items for Systematic Reviews and Meta-Analyses Extension for Scoping Reviews guidelines, which are available at https://www.prisma-statement.org/scoping.

Protocol/registration

No review protocol was registered for this scoping review.

Eligibility criteria, information sources, and search strategy

Human toxocariasis case reports indexed in PubMed between January 1, 2005, and December 31, 2025, were identified (n=151) using the query ("Toxocariasis"[Title/Abstract] OR "Toxocara"[Title/Abstract]) AND "Case Reports" [Publication Type] AND 2005:2025[dp] AND ffrft[Filter]. Free full-text articles were retrieved through PubMed Central or other free full-text links provided in PubMed using the ffrft filter. Seven nonhuman case reports involving cats, dogs, a foal, an opossum, or other animals were excluded using Antigravity-supported screening. Subsequently, 5 reports were excluded because objective diagnostic confirmation, such as positive serology, larval identification, histopathologic confirmation, or other explicit diagnostic evidence, could not be verified. The final 139 human case reports were used for data analysis and generation of the results (Dataset 1). All inclusion and exclusion decisions were supported by algorithmic extraction logic and cross-verified by the author.

The final 139 human case reports were analyzed after the following variables had been extracted into a structured CSV format: PubMed identifier, patient age, sex, chief complaint, associated symptoms, eosinophil count, and final diagnosis. Standardization followed a predefined pipeline: free-text symptom descriptors were first normalized into canonical labels and then mapped to Medical Subject Headings (MeSH) terms when applicable, whereas organ involvement was coded separately using explicit evidence statements, such as imaging findings or specialist examination findings, rather than symptom keywords alone.

Selection of sources of evidence

Retrieved records were screened sequentially for human case-report status, relevance to toxocariasis, and objective diagnostic confirmation. For diagnostic confirmation, the mere mention of a diagnostic modality, such as "ELISA performed," was not considered sufficient unless confirmatory results or definitive diagnostic statements were explicitly reported. Nonhuman reports were excluded, as were reports describing suspected or insufficiently documented toxocariasis without clear diagnostic evidence, such as serology, larval identification, histopathology, biopsy findings, or other explicit confirmation. Antigravity supported the initial screening by applying predefined inclusion and exclusion logic, and the author manually verified the artificial intelligence-generated decisions by reviewing titles, abstracts, and full texts. Ambiguous records were assessed conservatively and excluded when the diagnosis or human case-report status could not be confirmed. The final set included 139 confirmed human toxocariasis case reports. Exclusion reasons are summarized in Fig. 1

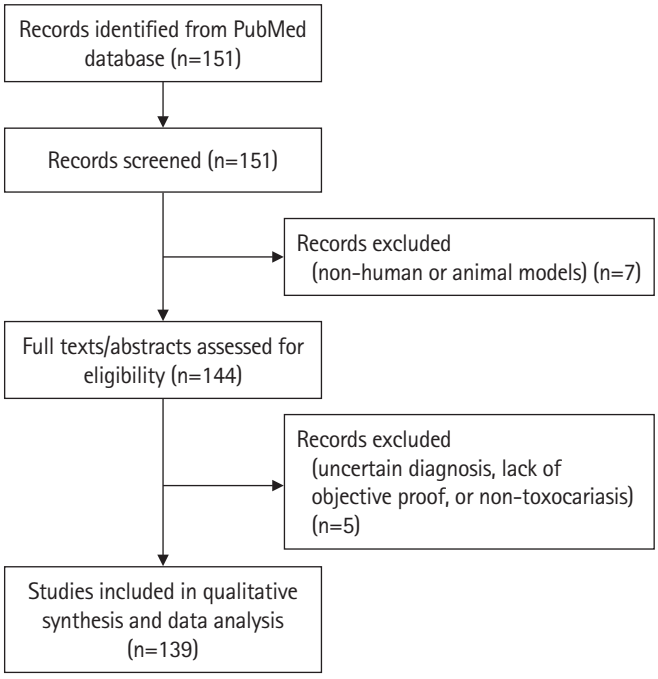

Fig. 1. Flow diagram of the case-report selection process for data analysis, reported according to the Preferred Reporting Items for Systematic Reviews and Meta-Analyses Extension for Scoping Reviews guideline.

and Supplement 1.

Data charting process

A structured CSV-based charting form was developed to extract bibliographic information, patient characteristics, clinical manifestations, eosinophil count or eosinophilia status, organ involvement, diagnostic evidence, final diagnosis, inclusion status, and extraction source. Antigravity generated preliminary extraction outputs from titles and abstracts and then refined these outputs using the retrieved free full-text articles.

Pilot charting was conducted to refine variable definitions, identify false-negative extractions, and standardize heterogeneous clinical terminology. Free-text symptom descriptions were mapped to standardized symptom labels and organ-involvement domains. Missing values were coded as "not reported," "not available," or "unable to extract." The author manually verified the artificial intelligence-generated charting outputs against the original sources and corrected misclassified or incomplete variables. The finalized charted dataset of 139 confirmed human case reports was then used for association analysis, correlation analysis, and k-means clustering.

Data items

Operational definitions were designed to minimize circularity between symptom variables and organ-involvement variables. Organ-involvement variables were coded only when reports explicitly indicated organ involvement, such as through imaging findings, specialist examinations, or diagnostic statements, and were not assigned solely on the basis of symptom terms that were coded separately as symptoms, including cough, dyspnea, headache, seizures, and meningitis.

- Age: expressions such as "years old" and "months old."
- Organ_Eye: Keywords "eye," "ocular," "retina," "vision," "uveitis," "macula," "blindness," "optic."
- Organ_Liver: Keywords "liver," "hepatic," "hepatomegaly."
- Organ_Lung: Keywords "lung," "pulmonary," "pleura/pleural," "pneumon-," "infiltrate," "consolidation," "effusion," "ARDS," "respiratory failure."
- Organ_CNS: Keywords "brain," "central nervous system," "CNS," "cerebral," "intracranial," "encephal-," "myel-," "spinal," "CSF," "meningeal enhancement."
- Organ_Heart: Keywords "heart," "cardiac," "myocarditis."

Because some organ variables partially overlapped with symptom terminology, symptom–organ pairs with direct definitional overlap were not interpreted as independent associations. Non-standard symptom expressions were mapped to MeSH terms. For example, pyrexia, shortness of breath, vision loss, and itching were mapped to fever, dyspnea, blindness, and pruritus, respectively. Eosinophilia values were extracted from full-text sentences that explicitly contained numeric laboratory thresholds or diagnostic terminology such as hypereosinophilia. Manual confirmation by the author identified data that had been misclassified by the artificial intelligence agent. Prompts instructed Antigravity to reevaluate missing data and extract additional information from the full texts.

Critical appraisal of individual sources

Formal methodological quality or risk-of-bias appraisal of individual case reports was not performed. Because this scoping review aimed to map clinical manifestations and clustering patterns rather than synthesize treatment effects or estimate pooled prevalence, no case report was excluded on the basis of reporting quality. However, eligibility required objective diagnostic confirmation of toxocariasis, and artificial intelligence-generated extraction outputs were manually checked by the author.

Synthesis of results

Three exploratory analyses were performed using the finalized binary clinical-feature matrix: (1) pairwise association testing with Fisher's exact test and odds ratios, (2) pairwise correlation analysis using phi/Pearson's r for binary features, and (3) k-means clustering to identify phenotypic patterns. Symptoms and organ-involvement variables were coded as present or absent for each included case report. Variables reported in fewer than 2 cases were excluded from pairwise analysis to reduce instability from sparse cells.

For pairwise association analysis, 2×2 contingency tables were constructed for a prespecified set of clinically relevant feature pairs ($n = 39$) that met the minimum frequency requirement, with each feature reported in at least 2 cases. Fisher's exact test was used to assess departure from independence. Odds ratios and 95% confidence intervals were calculated to estimate the direction, magnitude, and precision of associations. Directional interpretation was not inferred from the Fisher's exact test P-value alone. "Positive" indicated higher observed co-occurrence than expected under independence, generally corresponding to an odds ratio greater than 1; "negative" indicated lower observed co-occurrence than expected, generally corresponding to an odds ratio less than 1. Given the exploratory nature of this scoping review, Bonferroni or false discovery rate corrections were not applied to individual P-values because the primary goal was pattern identification rather than hypothesis testing. Unadjusted P-values should therefore

be interpreted with caution. Confidence intervals for odds ratios were computed using an exact method; therefore, nominal P-values and confidence intervals may not align perfectly after rounding, particularly for sparse tables.

Pearson correlation coefficients were calculated between binary feature pairs. For 2 binary variables, Pearson's r is equivalent to the phi coefficient. Correlation heatmaps summarized association strength and direction, whereas Fisher's exact test summarized statistical evidence against independence. K-means clustering was then applied to the binary clinical-feature matrix, with k = 4 selected on the basis of clinical interpretability and data-driven validation metrics, including the elbow method and silhouette score (Supplement 2). This analysis identified 4 clinically interpretable phenotypic groups: subclinical disease, ocular larva migrans, visceral larva migrans, and neurotoxocariasis/multisystemic disease. Analyses were performed using Python libraries, including pandas, SciPy, and scikit-learn. The source code for the Antigravity-supported analysis used in this study is available in Supplement 3.

Results

Selection of sources

The case-report selection process for data analysis is shown in Fig. 1.

Characteristics of sources of evidence

The final evidence set included 139 confirmed human toxocariasis case reports indexed between 2005 and 2025. The included reports contained patient-level information on age, sex, chief complaint, associated symptoms, eosinophil count or eosinophilia status, organ involvement, diagnostic evidence, and final diagnosis. Full-text articles were used for extraction. The reports covered diverse clinical presentations, including ocular larva migrans, visceral larva migrans, neurotoxocariasis or multisystemic disease, and subclinical or oligosymptomatic presentations. Detailed source-level characteristics and inclusion status are summarized in Supplement 1.

Critical appraisal of sources of evidence

No formal appraisal was performed; therefore, no appraisal results are presented.

Results of individual sources

Individual source-level charting results are presented in Supplement 1. The charted variables included PubMed identifier, title, patient age, sex, chief complaint, associated symptoms, eosinophil count or eosinophilia status, final diagnosis, raw abstract, and inclusion status. The included reports covered heterogeneous toxocariasis manifestations, including ocular, visceral, neurologic, cardiopulmonary, hepatic, and subclinical or oligosymptomatic presentations. Aggregate co-occurrence, association, and clustering findings are reported separately below.

Synthesis of results

Pairwise co-occurrence and association analysis

Pairwise co-occurrence and association analyses were performed using the binary clinical-feature matrix derived from the 139 included human toxocariasis case reports. Table 1 presents co-occurrence counts, odds ratios, 95% confidence intervals, Fisher's exact test P-values, and directional classifications for selected pairs of toxocariasis-related clinical features. Directional classification was based on observed-versus-expected co-occurrence under independence and the corresponding odds ratio, not on the Fisher's exact test P-value alone.

The highest co-occurrence counts were observed for eosinophilia with fever, blindness with uveitis, dyspnea with eosinophilia, cough with eosinophilia, eosinophilia with pruritus, and eosinophilia with headache. Pairs classified as positive showed higher observed co-occurrence than expected under independence and odds ratios greater than 1. Pairs classified as negative showed lower observed co-occurrence than expected under independence and odds ratios less than 1. Fisher's exact test was used to assess the nominal statistical significance of departure from independence.

The "Interpretation" column reflects observed-versus-expected co-occurrence, not a direct output of Fisher's exact test. Fisher's exact test provides the P-value for independence. Because many feature pairs were sparse, odds ratios and confidence intervals were estimated using exact methods and are reported with rounding. In rare instances, different feature pairs can yield numerically similar estimates after rounding. The underlying 2 × 2 tables for all reported pairs are provided in Supplement 4. An infinite odds ratio indicates a zero-cell count in the corresponding 2 × 2 table, and the Haldane-Anscombe correction was not applied.

To summarize nominal evidence against independence, clinical-feature pairs were grouped according to Fisher's exact test P-values. P-values were classified into descriptive tiers ($0.01 < P \leq 0.05$ and $P < 0.01$) without adjustment for multiple comparisons; these tiers were intended for descriptive reporting only (Table 2). These classifications were used only to summarize the distribution of P-values across feature pairs.

Cluster analysis

Table 1. Co-occurrence counts, ORs, 95% CIs, and Fisher's exact test results for pairwise associations between toxocariasis-related clinical features

Feature 1	Feature 2	Co-occurrence count	OR (95% exact CI)	P-value	Interpretation
Eosinophilia	Fever	40	7.04 (2.44–24.56)	< 0.0001	Positive
Blindness	Uveitis	32	Inf (31.00–Inf)	< 0.0001	Positive
Dyspnea	Eosinophilia	25	Inf (4.41–Inf)	< 0.0001	Positive
Cough	Eosinophilia	24	17.45 (2.62–732.42)	0.0001	Positive
Eosinophilia	Pruritus	24	17.45 (2.62–732.42)	0.0001	Positive
Eosinophilia	Headache	22	7.60 (1.71–69.05)	0.0019	Positive
Fever	Hepatomegaly	21	12.83 (4.30–42.38)	< 0.0001	Positive
Dyspnea	Fever	19	10.72 (3.57–35.58)	< 0.0001	Positive
Asthma	Eosinophilia	18	12.00 (1.76–510.18)	0.0034	Positive
Cough	Dyspnea	18	39.31 (10.84–148.27)	< 0.0001	Positive
Cough	Fever	17	6.53 (2.33–19.19)	< 0.0001	Positive
Eosinophilia	Myocarditis	17	Inf (2.59–Inf)	0.0006	Positive
Fever	Headache	17	7.55 (2.60–23.46)	< 0.0001	Positive
Fever	Pruritus	15	4.20 (1.55–11.57)	0.0019	Positive
Asthma	Fever	13	5.96 (1.89–20.51)	0.0009	Positive
Headache	Meningitis	13	18.23 (5.28–64.50)	< 0.0001	Positive
Blindness	Strabismus	12	25.80 (3.52–1,115.25)	< 0.0001	Positive
Cough	Hepatomegaly	12	6.09 (2.08–17.48)	0.0003	Positive
Fever	Myocarditis	12	6.47 (1.91–24.92)	0.0007	Positive
Asthma	Cough	11	10.41 (3.13–34.77)	< 0.0001	Positive
Asthma	Dyspnea	11	10.41 (3.13–34.77)	< 0.0001	Positive
Asthma	Pruritus	11	10.41 (3.13–34.77)	< 0.0001	Positive
Dyspnea	Hepatomegaly	11	4.81 (1.64–13.69)	0.0016	Positive
Hepatomegaly	Pruritus	11	4.81 (1.64–13.69)	0.0016	Positive
Cough	Pruritus	10	4.40 (1.46–12.73)	0.0035	Positive
Dyspnea	Myocarditis	10	10.19 (2.92–36.00)	< 0.0001	Positive
Strabismus	Uveitis	10	15.76 (3.57–93.60)	< 0.0001	Positive
Fever	Seizures	9	7.58 (1.74–45.25)	0.0020	Positive
Headache	Seizures	8	13.88 (3.18–68.27)	< 0.0001	Positive
Meningitis	Seizures	8	19.17 (4.21–96.45)	< 0.0001	Positive
Eosinophilia	Hepatomegaly	22	2.85 (0.95–10.27)	0.0462	Positive
Eosinophilia	Meningitis	18	5.88 (1.30–54.03)	0.0108	Positive
Blindness	Headache	14	2.84 (1.05–7.81)	0.0351	Positive
Fever	Meningitis	11	3.06 (1.04–9.10)	0.0361	Positive
Cough	Headache	9	3.71 (1.21–10.87)	0.0156	Positive
Asthma	Headache	7	3.53 (1.02–11.36)	0.0234	Positive
Dyspnea	Seizures	5	3.82 (0.86–15.46)	0.0411	Positive
Blindness	Myocarditis	2	0.19 (0.02–0.89)	0.0297	Negative
Hepatomegaly	Uveitis	2	0.22 (0.02–0.98)	0.0400	Negative

OR, odds ratio; CI, confidence interval.

K-means clustering with k = 4 identified 4 phenotypic clusters among the 139 included case reports (Table 3). Cluster 1 included 62 cases and was labeled subclinical disease. The only distinguishing feature reported in more than 15% of cases in this cluster was eosinophilia. Cluster 2 included 29 cases and was labeled ocular larva migrans. The distinguishing features were blindness, uveitis, eosinophilia, and strabismus. Cluster 3 included 30 cases and was labeled visceral larva migrans. The distinguishing features were fever, eosinophilia, hepatomegaly, dyspnea, cough, asthma, pruritus, myocarditis, and headache. Cluster 4 included 18 cases and was labeled neurotoxocariasis/multisystemic disease. The distinguishing features were eosinophilia, blindness, meningitis,

Table 2. Descriptive tiers of nominal pairwise associations between toxocariasis-related clinical features

Feature 1	Feature 2	P-value	Nominal P-value tier
Asthma	Cough	< 0.0001	Nominal (P < 0.01)
Asthma	Dyspnea	< 0.0001	Nominal (P < 0.01)
Asthma	Eosinophilia	0.0034	Nominal (P < 0.01)
Asthma	Fever	0.0009	Nominal (P < 0.01)
Asthma	Headache	0.0234	Nominal (0.01 < P ≤ 0.05)
Asthma	Pruritus	< 0.0001	Nominal (P < 0.01)
Blindness	Headache	0.0351	Nominal (0.01 < P ≤ 0.05)
Blindness	Myocarditis	0.0297	Nominal (0.01 < P ≤ 0.05)
Blindness	Strabismus	< 0.0001	Nominal (P < 0.01)
Blindness	Uveitis	< 0.0001	Nominal (P < 0.01)
Cough	Dyspnea	< 0.0001	Nominal (P < 0.01)
Cough	Eosinophilia	0.0001	Nominal (P < 0.01)
Cough	Fever	0.0001	Nominal (P < 0.01)
Cough	Headache	0.0156	Nominal (0.01 < P ≤ 0.05)
Cough	Hepatomegaly	0.0003	Nominal (P < 0.01)
Cough	Pruritus	0.0035	Nominal (P < 0.01)
Dyspnea	Eosinophilia	< 0.0001	Nominal (P < 0.01)
Dyspnea	Fever	< 0.0001	Nominal (P < 0.01)
Dyspnea	Hepatomegaly	0.0016	Nominal (P < 0.01)
Dyspnea	Myocarditis	0.0001	Nominal (P < 0.01)
Dyspnea	Seizures	0.0411	Nominal (0.01 < P ≤ 0.05)
Eosinophilia	Fever	< 0.0001	Nominal (P < 0.01)
Eosinophilia	Headache	0.0019	Nominal (P < 0.01)
Eosinophilia	Hepatomegaly	0.0462	Nominal (0.01 < P ≤ 0.05)
Eosinophilia	Meningitis	0.0108	Nominal (0.01 < P ≤ 0.05)
Eosinophilia	Myocarditis	0.0006	Nominal (P < 0.01)
Eosinophilia	Pruritus	0.0001	Nominal (P < 0.01)
Fever	Headache	< 0.0001	Nominal (P < 0.01)
Fever	Hepatomegaly	< 0.0001	Nominal (P < 0.01)
Fever	Meningitis	0.0361	Nominal (0.01 < P ≤ 0.05)
Fever	Myocarditis	0.0007	Nominal (P < 0.01)
Fever	Pruritus	0.0019	Nominal (P < 0.01)
Fever	Seizures	0.0020	Nominal (P < 0.01)
Headache	Meningitis	< 0.0001	Nominal (P < 0.01)
Headache	Seizures	0.0001	Nominal (P < 0.01)
Hepatomegaly	Pruritus	0.0016	Nominal (P < 0.01)
Hepatomegaly	Uveitis	0.0400	Nominal (0.01 < P ≤ 0.05)
Meningitis	Seizures	< 0.0001	Nominal (P < 0.01)
Strabismus	Uveitis	< 0.0001	Nominal (P < 0.01)

headache, fever, seizures, cough, dyspnea, asthma, pruritus, myocarditis, hepatomegaly, and strabismus.

The high prevalence of blindness in Cluster 4 suggests that some ocular larva migrans cases may have overlapped with this predominantly systemic/neurotoxocariasis cluster. This overlap reflects the hard boundaries imposed by k-means clustering; therefore, these programmatic clusters should be interpreted with the understanding that ocular larva migrans and neurotoxocariasis have distinct pathophysiological mechanisms.

Heatmap-based synthesis

Fig. 2 presents the co-occurrence counts for pairs of toxocariasis-associated clinical features. The diagonal represents self-co-occurrence and was set to zero by design to improve visualization of off-diagonal values. Higher co-occurrence counts are represented by darker cells.

Fig. 3 presents the statistical significance of pairwise associations using $-\log_{10}$-transformed P-values derived from Fisher's exact test. Lower P-values correspond to higher $-\log_{10}$-transformed P-values and darker cells in the heatmap.

Fig. 4 presents Pearson correlation coefficients between binary clinical features. For 2 binary variables, Pearson's r is equivalent to the phi coefficient. The correlation heatmap was used to summarize the strength and direction of association between feature pairs, whereas Fisher's exact test was used to assess departure from independence.

Discussion

Summary of evidence

This Antigravity-assisted systematic scoping review summarized co-occurrence, association, correlation, and clustering patterns among clinical features reported in 139 human toxocariasis case reports indexed in PubMed. The findings suggest that reported manifestations of human toxocariasis can be organized into several clinically recognizable phenotypic patterns, including subclinical or oligosymptomatic presentations, ocular larva migrans, visceral larva migrans, and neurotoxocariasis/multisystemic disease.

The pairwise association and clustering results indicated that ocular and visceral phenotypes were relatively distinct in the included case reports. Ocular features, particularly blindness, uveitis, and strabismus, tended to cluster together, whereas systemic features such as fever, dyspnea, cough, hepatomegaly, pruritus, and eosinophilia aligned more closely with visceral or multisystemic presentations. These findings are consistent with the established clinical distinction between ocular larva migrans and visceral larva migrans [2]. However, because the data were derived from case reports rather than a prospectively assembled clinical cohort, these patterns should be interpreted as descriptive and hypothesis-generating.

In pairwise Fisher's exact tests, eosinophilia was not statistically significantly associated with ocular features; however, eosinophilia was reported in a subset of ocular cases, and multivariate clus-

Table 3. Summary of the 4 phenotypic clusters identified by k-means clustering

Cluster	Clinical label	No. of cases	Distinguishing symptoms or features (prevalence > 15%)	Descriptive feature profile
1	Subclinical disease	62	Eosinophilia (48.4%)	Characterized by mild, atypical, or incompletely documented presentations.
2	Ocular larva migrans	29	Blindness (100.0%), uveitis (100.0%), eosinophilia (55.2%), strabismus (31.0%)	Characterized by concentrated ocular inflammation and subsequent severe visual impairment.
3	Visceral larva migrans	30	Fever (93.3%), eosinophilia (86.7%), hepatomegaly (63.3%), dyspnea (46.7%), cough (40.0%), asthma (33.3%), pruritus (33.3%), myocarditis (33.3%), headache (16.7%)	Distinguished by a pronounced systemic inflammatory presentation, including fever, together with major liver and cardiopulmonary involvement.
4	Neurotoxocariasis/ multisystemic disease	18	Eosinophilia (100.0%), blindness (83.3%), meningitis (77.8%), headache (77.8%), fever (72.2%), seizures (55.6%), cough (50.0%), dyspnea (44.4%), asthma (38.9%), pruritus (33.3%), myocarditis (16.7%), hepatomegaly (16.7%), strabismus (16.7%)	Distinguished by central nervous system involvement accompanied by multisystemic manifestations. Ocular features were also frequent, including blindness in 83.3% of cases.

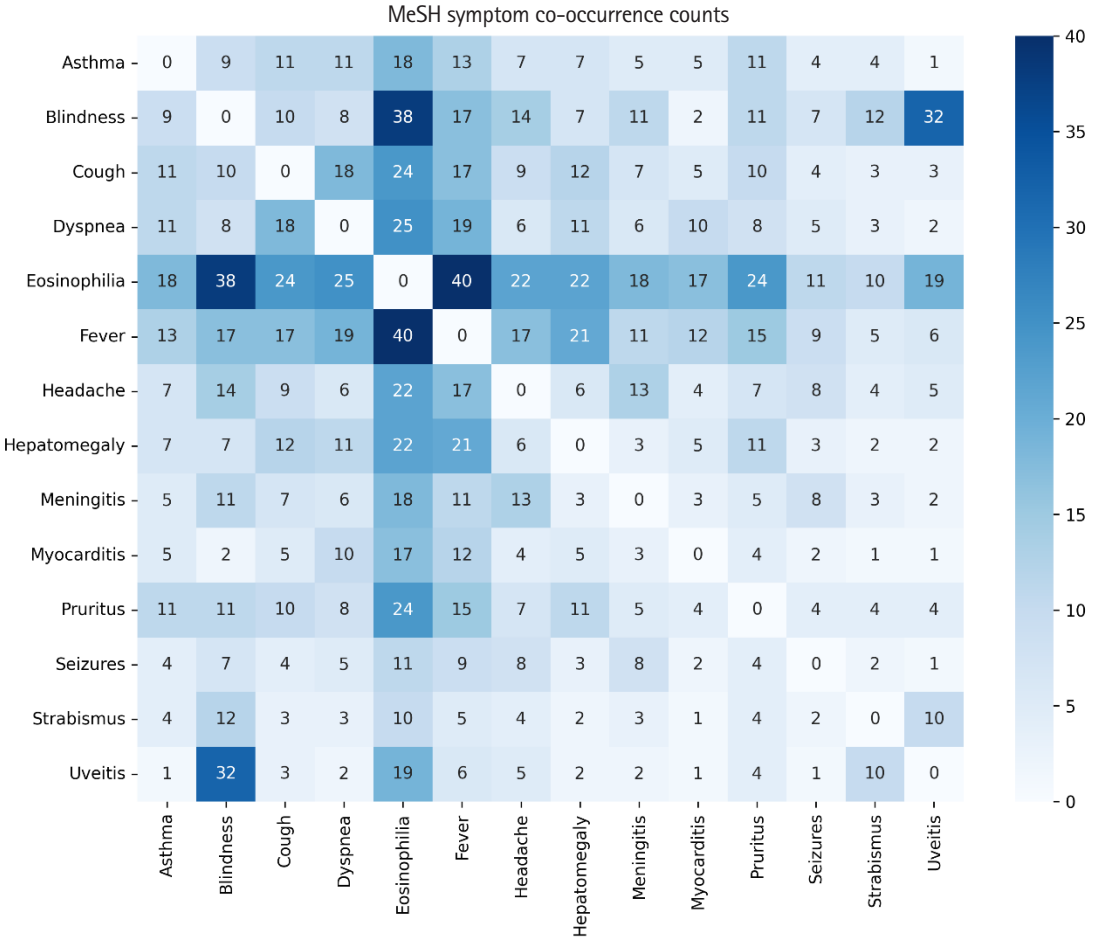

Fig. 2. Heatmap of co-occurrence counts for toxocariasis-associated clinical features.

tering can group cases with partial overlap across domains. This discrepancy reflects the difference between univariate, feature-by-feature association testing and clustering, which groups cases according to overall similarity across multiple features.

This finding suggests that eosinophilia may be more informative for systemic toxocariasis presentations than for isolated ocular disease. Previous reports have also described variability in eosinophilia among patients with ocular toxocariasis [4,5]. Nevertheless, the presence of eosinophilia in some cases assigned to the ocular larva migrans cluster indicates that ocular-predominant cases may

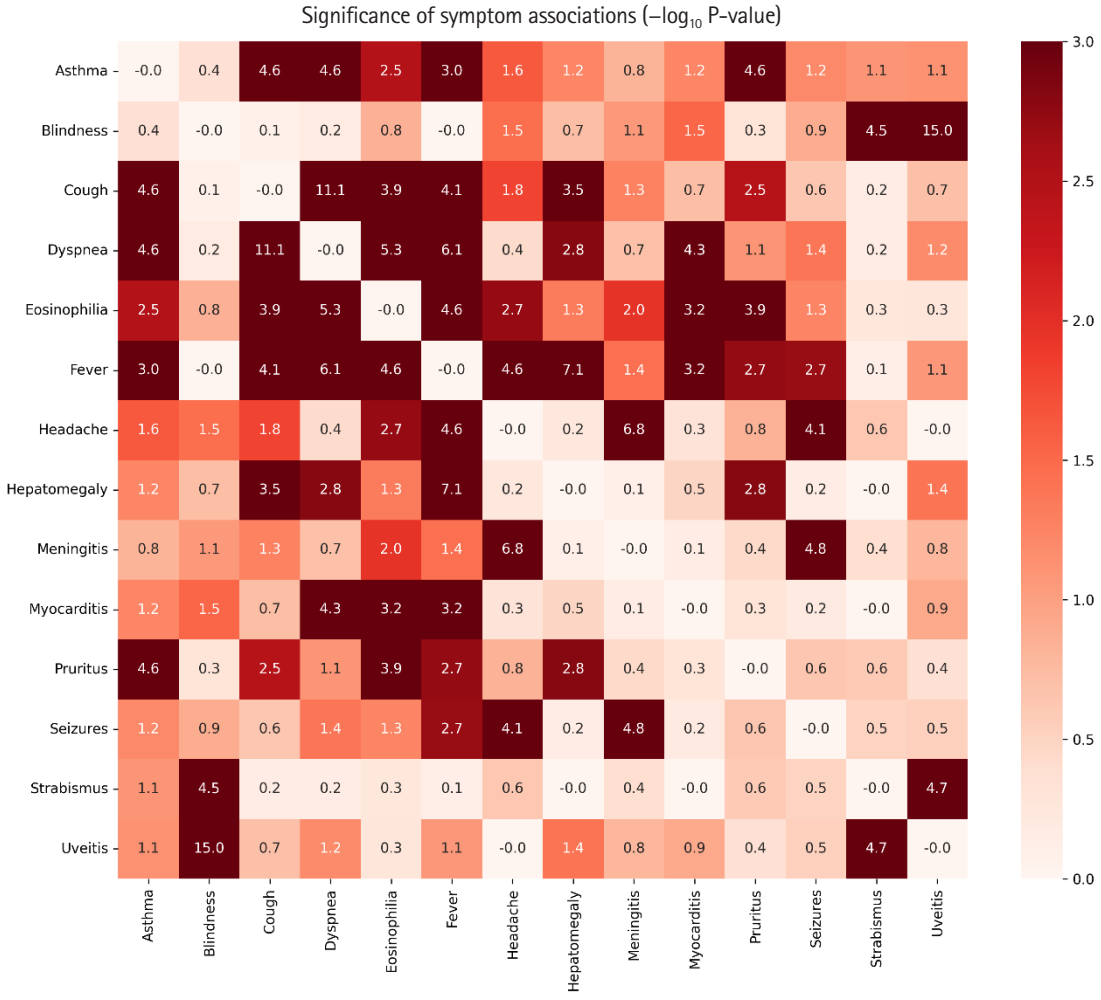

Fig. 3. Heatmap of $-\log_{10}$-transformed P-values for associations between toxocariasis-associated symptoms and features, calculated using Fisher's exact test.

overlap with systemic manifestations. Therefore, eosinophilia should not be used alone to distinguish ocular from visceral toxocariasis.

The neurotoxocariasis/multisystemic cluster included central nervous system features, including headache, meningitis, and seizures, alongside systemic and ocular manifestations. This pattern suggests that neurotoxocariasis reported in the case-report literature may often occur in a broader multisystemic clinical context rather than as an isolated neurologic presentation. The observed clustering pattern should be interpreted cautiously because k-means clustering groups cases according to overall feature similarity and does not assign strict clinical diagnoses.

The complementary use of Fisher's exact test, odds ratios, Pearson correlation coefficients, and k-means clustering provided different perspectives on the same binary clinical-feature matrix. Fisher's exact test assessed departure from independence, odds ratios estimated the direction and magnitude of associations, Pearson correlation coefficients summarized association strength, and k-means clustering identified exploratory phenotypic groupings. These methods support descriptive pattern recognition but do not establish causality, diagnostic performance, or clinical prediction.

Limitations

This study has several limitations. First, the analysis was restricted to case reports indexed in PubMed and filtered by free full-text availability, which may have introduced database, language, publication, and full-text availability biases. Mild, asymptomatic, or common presentations may have been underrepresented because case reports typically emphasize unusual or severe manifestations. Second, data were extracted from published narratives rather than standardized clinical records. Symptoms, eosinophil counts, diagnostic methods, organ involvement, treatment, and outcomes

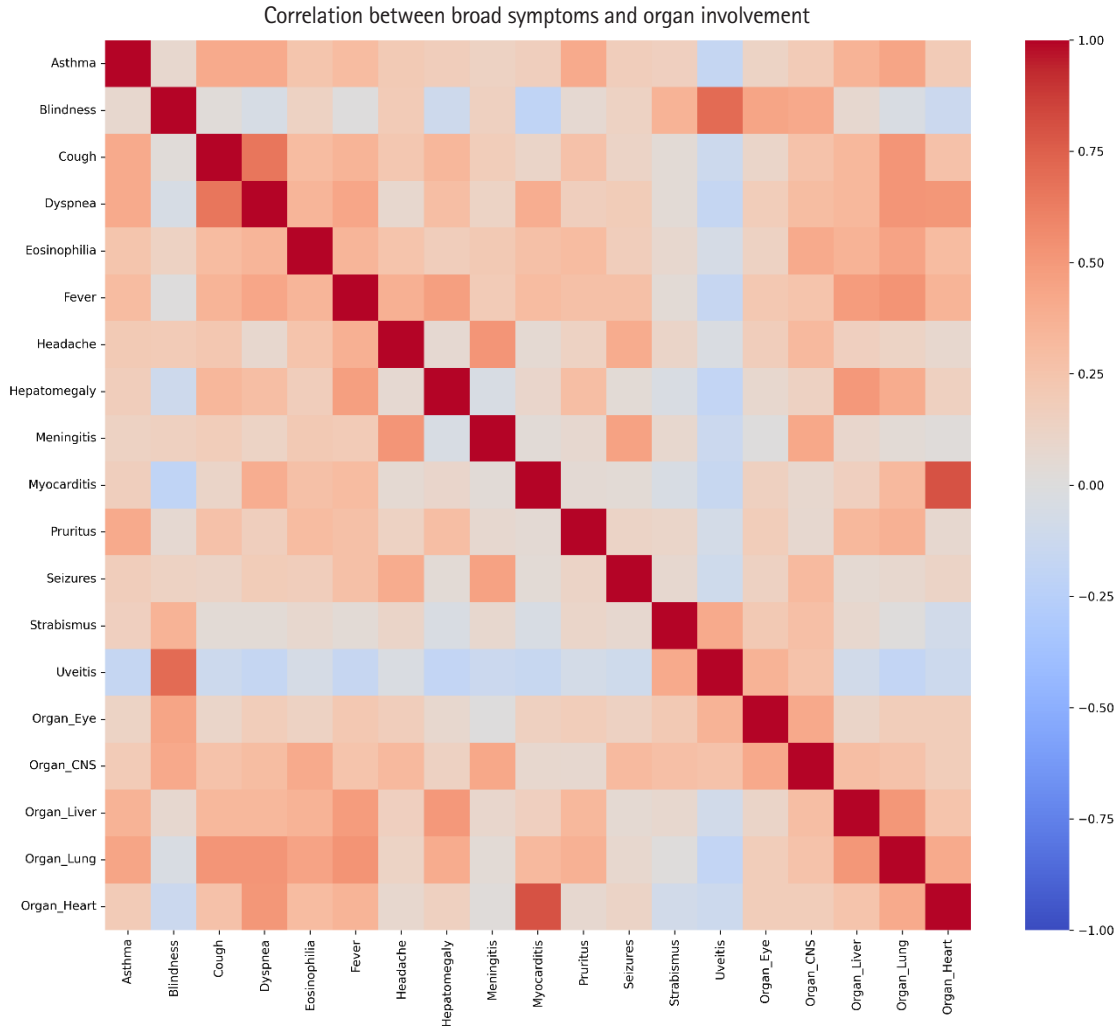

Fig. 4. Heatmap of Pearson correlation coefficients, equivalent to phi coefficients for binary clinical features, between toxocariasis-associated symptoms and organ-involvement variables.

were reported inconsistently, and unreported findings could not always be distinguished from true absence. Third, binary coding of heterogeneous clinical descriptions enabled association and clustering analyses but reduced clinical granularity and may have introduced misclassification during symptom mapping. Fourth, the statistical analyses were exploratory. Multiple pairwise comparisons were performed, P-values were interpreted descriptively, and odds ratios or confidence intervals may be unstable for sparse feature pairs. Pearson correlation coefficients for binary variables are also influenced by marginal prevalence. Fifth, k-means clustering grouped reports according to overall feature similarity rather than strict clinical diagnosis; therefore, clusters should be interpreted as exploratory phenotypic patterns, not validated disease subtypes. Finally, artificial intelligence-assisted extraction may have missed or misclassified information despite human verification and requires independent validation in curated datasets.

Suggestions for future research

Future studies should validate these exploratory findings using larger and more systematically curated datasets. Searches should be expanded beyond PubMed and PubMed Central to include additional bibliographic databases and regional literature sources, such as KoreaMed. Including non–free full-text reports may reduce selection bias and improve representativeness.

Further research should also standardize data extraction for age, sex, exposure history, diagnostic method, eosinophil count, organ involvement, treatment, and clinical outcome. Age-specific analyses may be useful because ocular larva migrans and visceral larva migrans may differ by age group [2]. Exposure-related variables, including geophagia, ingestion of raw animal liver, and regional dietary practices, should also be considered because such factors have been described in previous studies [6-11].

Future analyses should compare artificial intelligence-assisted ex-

traction with independent manual extraction to quantify the sensitivity, specificity, and error patterns of the workflow. Prospective clinical datasets or registry-based studies would be needed to determine whether the observed phenotypic patterns can support diagnosis, risk stratification, or clinical decision-making.

Conclusion

This Antigravity-assisted systematic scoping review identified exploratory co-occurrence, association, correlation, and clustering patterns among clinical manifestations reported in human toxocariasis case reports. The findings suggest relative separation between ocular and visceral phenotypes, frequent alignment of eosinophilia with systemic manifestations, and a multisystemic pattern among neurotoxocariasis-related reports. However, the results should be interpreted as hypothesis-generating rather than diagnostic or practice-guiding evidence. Artificial intelligence-assisted approaches may support data extraction and pattern recognition in scoping reviews, but human verification and validation against independently curated clinical datasets are required before clinical application.

ORCID

Eun Hee Ha: https://orcid.org/0009-0007-7137-0331

Authors' contribution

All work was completed by Eun Hee Ha.

Conflict of interest

The commercial program mentioned in this study is discussed for informational purposes and not for promotion. No other potential conflicts of interest relevant to this article were reported.

Funding

This work was supported by a student research grant from Hallym University College of Medicine (HLMC 2025-12-1). The funder had no role in study design, data collection and analysis, or manuscript preparation.

Data availability

Data files are available from Harvard Dataverse: https://doi.org/10.7910/DVN/33GBYE

Dataset 1. Data from the final 139 toxocariasis articles used for analysis.

Acknowledgments

None.

Supplementary materials

Supplementary files are available from Harvard Dataverse: https://doi.org/10.7910/DVN/33GBYE

Supplement 1. Table of toxocariasis case reports indexed in the NCBI PubMed database (2005–2025) containing the following categories: PMID, title, patient age, sex, chief complaint, associated symptoms, eosinophil count, final diagnosis, raw abstract, organ involvement, symptoms (MeSH), and inclusion status.

Supplement 2. Elbow method and silhouette score cluster-validation metrics supporting the selection of $k = 4$ as the optimal number of phenotypic clusters for the k-means analysis.

Supplement 3. Python code used for the data analysis in this study. All figures and Markdown files were generated using Antigravity.

Supplement 4. The underlying 2×2 contingency tables detailing the observed absolute cell counts (mutual presence, singular presence, and mutual absence) for all pairwise combinations of the analyzed toxocariasis-related clinical features.

References

1. Stensvold CR, Nielsen HV, Petersen E. Toxocariasis. Ugeskr Laeger 2011;173:186-189.
2. Yoshida A, Hombu A, Wang Z, Maruyama H. Larva migrans syndrome caused by Toxocara and Ascaris roundworm infections in Japanese patients. Eur J Clin Microbiol Infect Dis 2016;35:1521-1529. https://doi.org/10.1007/s10096-016-2693-x
3. Minamii T, Nishioka H. Case report: Toxocariasis manifesting as eosinophilic pleural effusion. Am J Trop Med Hyg 2024;110:687-690. https://doi.org/10.4269/ajtmh.23-0343
4. Paul M, Stefaniak J, Twardosz-Pawlik H, Pecold K. The co-occurrence of Toxocara ocular and visceral larva migrans syndrome: a case series. Cases J 2009;2:6881. https://doi.org/10.1186/1757-1626-2-6881
5. Choi KD, Choi JH, Choi SY, Jung JH. Toxocara optic neuropathy: clinical features and ocular findings. Int J Ophthalmol 2018;11:520-523. https://doi.org/10.18240/ijo.2018.03.26
6. Huynh TM, Tran KQ, Dinh TH, Vo MM, Pham TQ, Vo TD. Atypical Toxocara canis-induced hepatic visceral larva migrans: diagnostic challenges and literature review. Korean J Gastroenterol 2024;83:247-252. https://doi.org/10.4166/kjg.2024.051
7. Pieroni F, Massei F, Micheletti MV, Luti L, De Marco E, Ludovisi A, Casazza G, Bruschi F. Toxocariasis in a child with autism spectrum disorder. Int J Environ Res Public Health 2021;18:283. https://doi.org/10.3390/ijerph18010283
8. Sayas I, Álvarez P, Pajuelo R, Luque W, Tassara C. Atypical presentation of infant toxocariasis: about a case. Rev Chilena Infec-

tol 2021;38:698-701. https://doi.org/10.4067/s0716-10182021000500698
9. Üblagger D, Auer H, Bezakova M, Kirchlechner V. Toxocarosis in a patient with autism spectrum disorder presenting with severe hypereosinophilia and acute respiratory distress: a case report. Parasitol Res 2024;123:99. https://doi.org/10.1007/s00436-024-08119-y
10. Noh Y, Hong ST, Yun JY, Park HK, Oh JH, Kim YE, Jeon BS. Meningitis by Toxocara canis after ingestion of raw ostrich liver. J Korean Med Sci 2012;27:1105-1108. https://doi.org/10.3346/jkms.2012.27.9.1105
11. Yoshikawa M, Ouji Y, Nishiofuku M, Moriya K, Kasahara K, Mikasa KI, Mizuno Y, Nakamura T, Ogawa S, Ishizaka S, Akao N. Visceral toxocariasis from regular consumption of raw cow liver. Intern Med 2008;47:1289-1290. https://doi.org/10.2169/internalmedicine.47.1191

eISSN: 2234-2591
Open Access

Original article

Ewha Med J 2026;49(3):e20
https://doi.org/10.12771/emj.2026.01396

The Ewha Medical Journal

Effect of ultrasound-guided bilateral rectus sheath block on postoperative pain control after robotic single-site gynecologic surgery: a randomized controlled study

Sunyoung Moon[1], Sooyoung Cho[1*], Youn Jin Kim[1], Seunghee Yoo[1], Jong Wha Lee[1], Hye-Won Oh[1], Eunbi Cho[2]

[1]*Department of Anesthesiology and Pain Medicine, Ewha Womans University College of Medicine, Seoul, Korea*
[2]*Department of Anesthesiology and Pain Medicine, Ewha Womans University Medical Center Mokdong Hospital, Seoul, Korea*

Purpose: Rectus sheath block (RSB) is a simple abdominal wall block that can be readily applied. This study evaluated the postoperative analgesic efficacy of ultrasound-guided bilateral RSB in robotic single-site gynecologic surgery.
Methods: Sixty patients were randomly assigned to the RSB group (n=30) or the control group (n=30). After induction of general anesthesia, patients in the RSB group received ultrasound-guided bilateral RSB with 30 mL of 0.25% ropivacaine. Pain intensity was assessed using a verbal numerical rating scale (VNRS) at 0, 1, 6, 12, 24, and 48 hours postoperatively. Intravenous patient-controlled analgesia was provided to all patients, and fentanyl was administered as rescue analgesia on request.
Results: VNRS scores at 0, 1, and 6 hours were significantly lower in the RSB group than in the control group (all P<0.05). Rescue fentanyl use in the post-anesthesia care unit was also significantly lower in the RSB group than in the control group (19.8±21.0 μg vs. 46.3±27.6 μg, P<0.001). Subgroup analysis showed that RSB was associated with lower VNRS scores in patients undergoing ovarian surgery or myomectomy, whereas no significant difference was observed in patients undergoing hysterectomy.
Conclusion: Ultrasound-guided bilateral RSB reduced early postoperative pain and rescue analgesic requirements after robotic single-site gynecologic surgery.

Keywords: Nerve block; Postoperative pain; Robotic surgical procedures

Introduction

Multimodal analgesia has become a cornerstone of postoperative pain management [1,2]. In abdominal surgery, regional blocks such as the transversus abdominis plane (TAP) block, rectus sheath block (RSB), and quadratus lumborum block are effective components of this approach [3,4]. Postoperative abdominal pain has somatic and visceral components [5,6]. TAP block and RSB primarily target somatic pain, whereas systemic analgesics address broader postoperative pain, including the visceral component [2,3]. Combining these modalities can improve the quality of postoperative recovery [1].

Over the past decade, laparoscopic and robotic surgeries have become increasingly common. Although these minimally invasive approaches can reduce postoperative discomfort, patients may still experience substantial pain [5,7]. The sensory blockade produced by RSB is usually confined to the midline; however, our previous study demonstrated clinical benefit even in laparoscopic gynecologic surgeries involving multiple lateral incisions [8]. Because bilateral RSB-induced somatic analgesia can reduce pain after gynecologic laparoscopy, the present study evaluated the efficacy of bilateral RSB in single-site robotic surgery, which requires only a single periumbilical incision. We hypothesized that ultrasound-guided bilateral RSB would reduce early postoperative pain after robotic single-site gynecologic surgery. The primary objective was to compare the verbal numerical rating scale

*Corresponding email: sooyoung.cho@ewha.ac.kr
Received: May 18, 2026 Revised: June 9, 2026 Accepted: June 10, 2026

(VNRS) pain score at 6 hours postoperatively between the RSB and control groups. Secondary objectives were to compare VNRS scores at other time points, rescue analgesic requirements, fentanyl consumption through intravenous patient-controlled analgesia (IV-PCA), and the time to the first rescue analgesic request.

Methods

Study design and patient selection

This prospective, randomized, observer-blinded clinical trial was conducted from May 2015 to January 2017. After approval by the Institutional Review Board of Ewha Womans University Medical Center (EUMC 2015-01-024-002) and registration at ClinicalTrials.gov (NCT02450084), 60 patients provided written informed consent and were enrolled in the study. The inclusion criteria were age 21–60 years and scheduled robotic single-site gynecologic surgery. The exclusion criteria were gynecologic cancer surgery, American Society of Anesthesiologists (ASA) physical status III or higher, a history of abdominal surgery, allergy to local anesthetics, particularly ropivacaine, opioid tolerance, coagulopathy, infection at the needle insertion site, and inability to cooperate with the study protocol.

Randomization and anesthesia protocol

Patients were randomly allocated to the RSB group or the control group (n = 30 each) using a computer-generated randomization table. General anesthesia was induced with intravenous glycopyrrolate 0.2 mg, midazolam 3 mg, 1% propofol 2 mg/kg, fentanyl 1 μg/kg, and rocuronium 0.6 mg/kg. After endotracheal intubation, anesthesia was maintained with 2%–3% sevoflurane at an FiO_2 of 0.5 to maintain a bispectral index value between 40 and 60. Additional fentanyl boluses of 0.5–1 μg/kg were administered to maintain blood pressure and heart rate within 20% of the baseline values recorded in the operating room.

Procedure for ultrasound-guided bilateral RSB

Ultrasound-guided bilateral RSB was performed by a single experienced anesthesiologist once each patient's vital signs had stabilized following intubation. Following the protocol established in our previous study [8], a 38-mm, 6–13-MHz linear transducer (Sonosite M-Turbo; Sonosite) was placed transversely immediately lateral to the umbilicus. A 22G Tuohy needle was inserted using an in-plane technique and advanced from the medial to the lateral side of the transducer. After the needle reached the plane between the rectus muscle and the posterior rectus sheath, 15 mL of 0.25% ropivacaine was injected. Successful placement was confirmed by real-time ultrasound visualization of a hypoechoic local anesthetic pocket. The procedure was then repeated on the contralateral side.

Postoperative pain management and assessment

On arrival at the post-anesthesia care unit (PACU), all patients received IV-PCA, which was continued for 48 hours postoperatively. The IV-PCA solution consisted of fentanyl 800 μg and ramosetron hydrochloride 0.3 mg in normal saline, for a total volume of 100 mL. To evaluate and compare patient-demand opioid consumption more accurately, the background continuous infusion was minimized. Because the IV-PCA device required a minimum continuous infusion setting, it was programmed to the lowest possible rate, 0.8 μg/hr (0.1 mL/hr). The device was also set to deliver a 16-μg (2.0-mL) bolus dose with a 15-minute lockout interval. Portable IV-PCA pumps (Accumate 1100; Woo Young Medical Co. Ltd.) recorded the timing and frequency of each patient's bolus attempts.

In addition to IV-PCA, rescue analgesics were administered when postoperative pain was inadequately controlled. During the PACU period, including the 0- and 1-hour postoperative assessments, intravenous fentanyl was administered as rescue analgesia. After transfer to the general ward, intravenous ketorolac 30 mg was administered as rescue analgesia whenever the patient reported a VNRS score of 4 or higher or requested additional analgesia.

Postoperative pain intensity was assessed at 6 time points. The first 2 assessments were performed in the PACU: immediately on arrival (time 0) and 1 hour later (time 1). Pain was assessed using the VNRS, which ranges from 0, indicating no pain, to 10, indicating the most severe pain imaginable. To maintain objectivity, all assessments were performed by an interviewer blinded to group assignment. After transfer to the ward, the blinded interviewer obtained VNRS scores at 6, 12, 24, and 48 hours postoperatively.

Outcomes

The primary outcome was the between-group difference in VNRS score at 6 hours postoperatively. This time point was selected based on our previous finding that the analgesic duration of RSB is approximately 6 hours [8]. Secondary outcomes were VNRS scores at 0, 1, 12, 24, and 48 hours; rescue fentanyl dose in the PACU; the proportion of patients requiring rescue analgesics; time to the first rescue analgesic request; the cumulative number of rescue analgesic doses; and the cumulative fentanyl dose infused through IV-PCA up to 48 hours.

Sample size calculation and statistical analysis

The sample size was calculated based on an anticipated 33% reduction in pain at 6 hours. Power analysis, assuming 90% power

and a type I error rate of 0.05, indicated that 27 patients were required per group. To allow for a potential 10% dropout rate, 30 patients were enrolled in each group, for a total sample size of 60.

Statistical analysis was performed using SPSS for Windows ver. 18.0 (SPSS Inc.). Continuous variables were analyzed using Student's t-test, and categorical variables were compared using the chi-square test or Fisher's exact test, as appropriate. A P-value < 0.05 was considered statistically significant.

Results

A total of 60 patients were enrolled in the study (Fig. 1). Demographic characteristics and operative data did not differ significantly between the 2 groups (Table 1).

Postoperative pain and analgesic consumption in the PACU

The primary outcome, the VNRS score at 6 hours postoperatively, was significantly lower in the RSB group than in the control group (3.0 ± 1.7 vs. 4.1 ± 1.9, $P = 0.026$). VNRS scores were also significantly lower in the RSB group than in the control group at 0, 1, and 6 hours postoperatively ($P < 0.001$, $P = 0.001$, and $P = 0.026$, respectively) (Table 2, Fig. 2). Although intraoperative fentanyl requirements did not differ significantly between the groups, rescue fentanyl use in the PACU was significantly lower in the RSB group (19.8 ± 21.0 μg vs. 46.3 ± 27.6 μg, $P < 0.001$). The proportion of patients requiring rescue analgesics in the PACU was also significantly lower in the RSB group ($P = 0.009$).

The mean time to the first request for rescue analgesia was significantly longer in the RSB group than in the control group (35.4 minutes vs. 12.9 minutes, $P = 0.002$). Although the cumulative number of rescue analgesic doses was significantly lower in the RSB group at all time points, the total fentanyl dose infused through IV-PCA during the 48-hour postoperative period did not differ significantly between the groups (230.7 ± 207.8 μg in the control group vs. 260.8 ± 189.4 μg in the RSB group, $P = 0.560$). In the IV-PCA data (Table 2), no significant between-group differences were observed in the number of bolus attempts or delivered boluses, except for the number of delivered boluses at 1 hour.

Subgroup analysis by surgery type

In the subgroup analysis, VNRS scores were significantly lower in the RSB group for up to 1 hour postoperatively among patients undergoing ovarian surgery ($n = 11$ in the RSB group, $n = 8$ in the

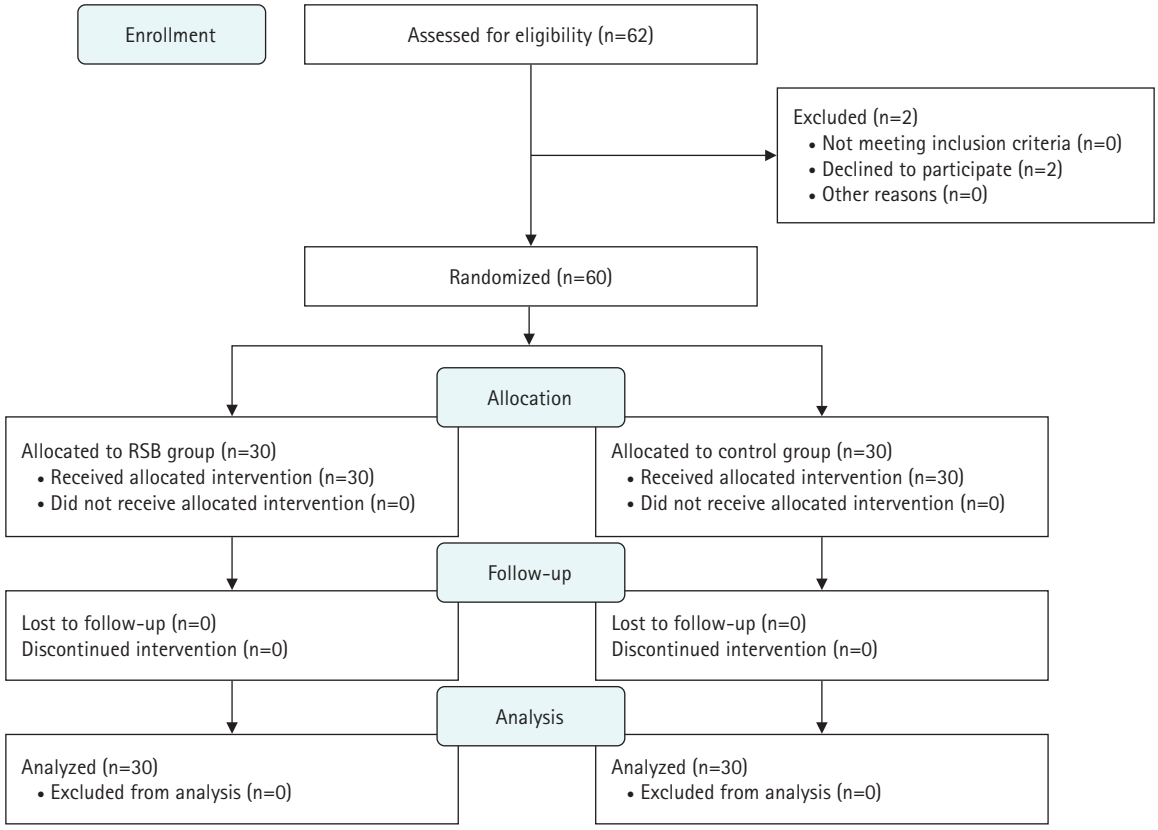

Fig. 1. Consolidated Standards of Reporting Trials (CONSORT) flow diagram.

Table 1. Demographic and operation-related data

Characteristic	Control group (n = 30)	RSB group (n = 30)	P-value
Age (yr)	35.4 ± 9.8	34.3 ± 8.2	0.629
ASA PS			0.573
I	20	22	
II	10	8	
Body mass index (kg/m^2)	21.4 ± 2.8	22.1 ± 4.5	0.432
Operation type			0.676
Ovarian surgery	8	11	
Hysterectomy	6	6	
Myomectomy	16	13	
Adhesiolysis			0.592
Yes	12	10	
No	18	20	
Operation time (min)	117.0 ± 48.5	123.2 ± 54.0	0.642
Anesthesia time (min)	159.2 ± 49.1	164.1 ± 52.6	0.709
Intraoperative fentanyl dose (μg)	146.0 ± 39.4	158.6 ± 40.6	0.231
Rescue analgesics in PACU			0.009
Yes	27	17	
No	3	13	
Rescue fentanyl dose in the PACU (μg)	46.3 ± 27.6	19.8 ± 21.0	< 0.001
Time to the first rescue analgesic request (min)	12.9 ± 17.9	35.4 ± 29.0	0.002

Values are presented as mean±standard deviation or number of patients. The RSB group received ultrasound-guided bilateral rectus sheath block with 30 mL of 0.25% ropivacaine.
RSB, rectus sheath block; ASA PS, American Society of Anesthesiologists physical status classification; PACU, post-anesthesia care unit.

Table 2. Intravenous patient-controlled analgesia and rescue analgesic data

Variable	Control (n = 30)	RSB (n = 30)	P-value
VNRS			
0 hr	6.4 ± 2.1	4.0 ± 2.7	< 0.001
1 hr	5.5 ± 2.1	3.8 ± 1.6	0.001
6 hr	4.1 ± 1.9	3.0 ± 1.7	0.026
12 hr	3.1 ± 1.5	2.7 ± 1.6	0.270
24 hr	2.5 ± 1.3	2.0 ± 1.2	0.130
48 hr	1.9 ± 1.1	1.7 ± 1.3	0.390
Total dose of fentanyl infused via IV-PCA (μg)			
1 hr	24.8 ± 16.7	17.3 ± 15.4	0.077
6 hr	84.3 ± 59.5	84.3 ± 74.4	1.000
12 hr	123.7 ± 106.6	120.5 ± 115.3	0.912
24 hr	171.7 ± 167.0	182.4 ± 176.0	0.811
48 hr	230.7 ± 207.8	260.8 ± 189.4	0.560
Cumulative no. of delivered IV-PCA boluses			
1 hr	1.5 ± 1.0	1.0 ± 0.9	0.042
6 hr	4.7 ± 3.5	5.2 ± 4.8	0.669
12 hr	6.5 ± 5.8	6.7 ± 6.7	0.886
24 hr	8.3 ± 8.3	11.9 ± 12.5	0.190
48 hr	10.8 ± 10.9	15.3 ± 13.4	0.152
Cumulative no. of IV-PCA bolus attempts			
1 hr	4.8 ± 13.7	2.2 ± 3.7	0.326
6 hr	11.0 ± 16.5	15.1 ± 41.6	0.615
12 hr	13.1 ± 19.4	19.2 ± 45.4	0.499
24 hr	15.7 ± 23.5	24.8 ± 49.2	0.368
48 hr	18.8 ± 26.7	28.4 ± 48.9	0.349
No. of rescue analgesic doses			
0 hr	0.7 ± 0.5	0.0 ± 0.2	< 0.001
1 hr	1.7 ± 0.9	0.8 ± 0.8	< 0.001
6 hr	2.4 ± 1.1	1.5 ± 1.0	0.001
12 hr	3.0 ± 1.4	1.8 ± 1.3	0.001
24 hr	3.6 ± 1.8	2.0 ± 1.5	< 0.001
48 hr	3.8 ± 2.1	2.1 ± 1.5	0.001

Values are presented as mean±standard deviation. The RSB group received ultrasound-guided bilateral rectus sheath block with 30 mL of 0.25% ropivacaine.
RSB, rectus sheath block; VNRS, verbal numerical rating scale; IV-PCA, intravenous patient-controlled analgesia.

control group; P = 0.013 at 0 hours and P = 0.007 at 1 hour). Among patients undergoing myomectomy (n = 13 in the RSB group, n = 16 in the control group), VNRS scores were significantly lower in the RSB group at 0, 1, 6, and 24 hours postoperatively (P = 0.007, P = 0.015, P = 0.008, and P = 0.048, respectively). In contrast, no significant differences in VNRS scores were observed at any time point in the hysterectomy subgroup (n = 6 per group) (Fig. 2).

Discussion

This study evaluated the effect of RSB on postoperative pain and analgesic requirements in patients undergoing single-incision robotic gynecologic surgery. RSB reduced immediate postoperative pain in the PACU, decreased rescue fentanyl requirements, and delayed the first request for rescue analgesia. However, the total fentanyl dose infused through IV-PCA over the 48-hour study period did not differ between groups.

In this study, the RSB group had significantly lower VNRS scores at 0, 1, and 6 hours postoperatively than the control group, as well as lower rescue fentanyl use in the PACU and a longer time to the first rescue analgesic request. Single-site surgery requires a major periumbilical incision in an area innervated primarily by the anterior cutaneous branches of the lower thoracic nerves (T7–T11) [9,10]. In an RSB, local anesthetic is injected between the rectus abdominis muscle and the posterior rectus sheath, where it

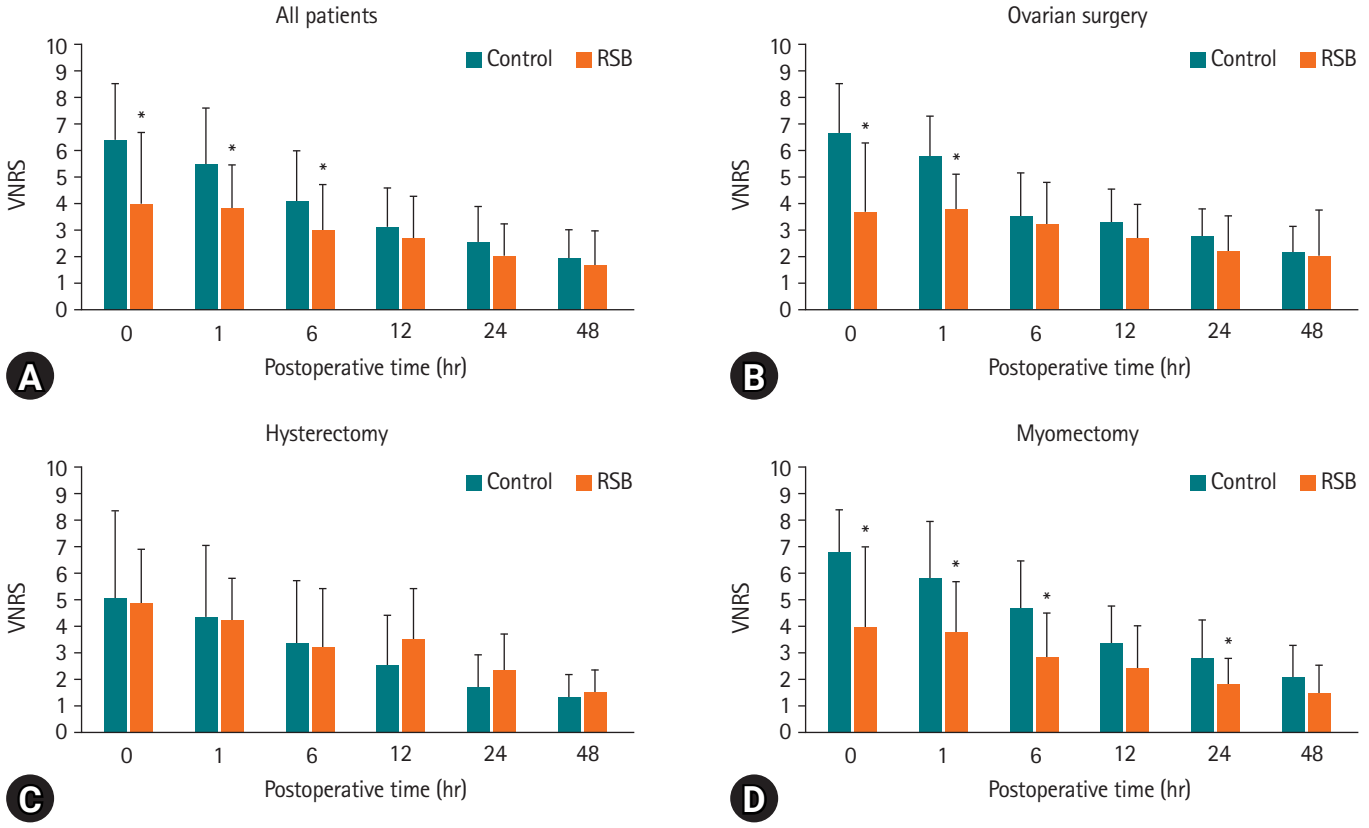

Fig. 2. (A–D) Postoperative pain intensity measured using a verbal numerical rating scale (VNRS) over time. Pain scores were assessed at 0, 1, 6, 12, 24, and 48 hours postoperatively in the rectus sheath block (RSB) and control groups. VNRS scores are presented for the overall study population and for subgroups defined by surgery type: ovarian surgery, myomectomy, and hysterectomy. *P<0.05.

blocks these nerves and reduces somatic pain from the skin and muscles of the abdominal wall [2,3,8,10]. Previous studies have also reported that RSB is effective for early postoperative pain management, particularly within 6–12 hours after surgery, and can reduce opioid consumption after major abdominal surgery; the early postoperative findings of the present study are consistent with these reports [7,11-14].

Despite the clear analgesic effect observed in the PACU, the total fentanyl dose infused through IV-PCA over 48 hours did not differ significantly between the 2 groups. Two factors may explain this finding. First, the effect of the local anesthetic used for single-injection RSB generally begins to wane after 6–12 hours [10,11]. Second, from an anatomical perspective, RSB blocks somatic pain from the abdominal wall but does not block visceral pain originating from intra-abdominal organs. Robotic gynecologic surgery may induce substantial visceral pain, potentially comparable to somatic pain, because of pneumoperitoneum, traction, and resection of internal organs during the procedure. In the early postoperative period, somatic pain at the incision site is likely to predominate, which may make the effect of RSB more apparent. As incisional pain subsides and visceral pain becomes a larger contributor to the overall pain experience, opioid requirements may become similar between groups.

The subgroup analysis illustrates the potential indications and limitations of RSB. Although the RSB group had significantly lower pain scores among patients who underwent myomectomy or ovarian surgery, no significant difference in pain scores was observed at any time point in the hysterectomy subgroup. This difference may reflect variation in the intensity of visceral pain across surgical procedures and differences in neural innervation pathways. Hysterectomy requires extensive manipulation and resection of the uterus and upper vagina, which may produce marked visceral pain transmitted through the lumbar splanchnic nerves (T12–L2) and pelvic splanchnic nerves (S2–S4) [15]. Major gynecologic surgeries can involve a substantial visceral pain component; therefore, the analgesic effects of abdominal wall blocks alone, such as RSB or TAP block, may be less apparent [3,15]. Thus, even if RSB reduces incision-site pain in patients undergoing hysterectomy, the overall VNRS score may not decrease if intense pelvic visceral pain remains insufficiently controlled [8,15].

In contrast, myomectomy and ovarian surgery generally involve less deep pelvic traction and no vaginal cuff suturing, which may result in a smaller visceral pain component. Consequently, postoperative pain may remain better controlled for up to 24 hours in these surgical settings, even after the analgesic effect of RSB has waned.

Although pain scores were significantly lower in the RSB group up to 6 hours postoperatively, total fentanyl consumption appeared to converge with that in the control group after this time point (Table 2). This pattern may reflect rebound pain, in which previously suppressed pain becomes more intense as the effect of a single-injection local anesthetic block resolves [16]. Rebound pain after peripheral nerve block resolution can cause marked pain and increase the need for systemic analgesics, including opioids. It has been described as a major contributor to increased reliance on systemic analgesia after nerve block resolution. Therefore, although single-injection RSB is effective for reducing immediate postoperative pain, it may not fully prevent a compensatory increase in IV-PCA use after block resolution, which may limit its opioid-sparing effect over a longer postoperative period.

This study has several limitations. First, it was conducted at a single institution and included a relatively small sample; in particular, the hysterectomy subgroup was small, which limited statistical power and generalizability. Second, the 48-hour follow-up period precluded assessment of patient and surgeon satisfaction and longer-term recovery outcomes. Third, because pain was assessed using a single VNRS score, somatic and visceral pain could not be evaluated separately. Fourth, the objective success of RSB could not be confirmed by postoperative sensory testing. Because the block was performed after induction of general anesthesia, sensory blockade could only have been assessed in the PACU. This assessment was deliberately omitted for several reasons: patient responses immediately after surgery may have been inaccurate because of residual anesthetic effects; sensory testing could have compromised patient blinding to group allocation; and, most importantly, applying sensory stimuli, such as pinprick or cold testing, near the surgical site could have caused unnecessary additional pain, particularly in the control group. In addition, neither a clinically meaningful basal opioid infusion nor routine nonopioid analgesics, such as nonsteroidal anti-inflammatory drugs or acetaminophen, were administered as part of a fixed multimodal regimen, to isolate the analgesic effect of RSB on patient-driven opioid demand. Consequently, a substantial proportion of patients, including 17 of 30 in the RSB group, still required rescue analgesics in the PACU. The benefit of RSB might therefore be more clearly demonstrated when RSB is incorporated into a nonopioid-based multimodal analgesic regimen. Future large-scale, multicenter studies should address these limitations and evaluate somatic and visceral pain separately.

In conclusion, RSB was a useful component of multimodal analgesia for robotic single-site gynecologic surgery. It reduced pain and decreased rescue analgesic use during the immediate postoperative PACU period. Future research should evaluate adjuvants that may prolong the duration of RSB or examine RSB in combination with additional analgesic therapies that can address substantial visceral pain.

ORCID

Sunyoung Moon: https://orcid.org/0009-0005-5706-6937
Sooyoung Cho: https://orcid.org/0000-0002-0232-766X
Youn Jin Kim: https://orcid.org/0000-0001-9189-5839
Seunghee Yoo: https://orcid.org/0000-0002-6811-7198
Jong Wha Lee: https://orcid.org/0000-0003-3574-191X
Hye-Won Oh: https://orcid.org/0000-0001-9819-5915
Eunbi Cho: https://orcid.org/0009-0005-6335-0512

Authors' contribution

Conceptualization: SC, YJK. Data curation: SM, SC, SY, HWO, EC. Formal analysis: SC, SY, HWO, EC. Investigation: SC, SY. Methodology: SC, YJK. Supervision: YJK. Writing–original draft: SM, SC. Writing–review & editing: SC, YJK, SY, JWL, HWO, EC.

Conflict of interest

No potential conflict of interest relevant to this article was reported.

Funding

None.

Data availability

The datasets generated and/or analyzed during the current study are not publicly available, but are available from the corresponding author on reasonable request.

Acknowledgments

None.

Supplementary materials

None.

References

1. Cheng C, Wang J, Cao Y, Gu E, Liu X. Effect of rectus sheath

block on postoperative quality of recovery after transabdominal midline gynecological surgery: a randomized controlled trial. J Pain Res 2024;17:2155-2163. https://doi.org/10.2147/JPR.S460367
2. Yoo SH, Beak MH, Lee DH, Kim WJ. Effect of perineural dexamethasone as an adjuvant to ropivacaine in rectus sheath block for radical cystectomy: a randomized controlled trial. J Clin Med 2025;14:5186. https://doi.org/10.3390/jcm14155186
3. Chin KJ, McDonnell JG, Carvalho B, Sharkey A, Pawa A, Gadsden J. Essentials of our current understanding: abdominal wall blocks. Reg Anesth Pain Med 2017;42:133-183. https://doi.org/10.1097/AAP.0000000000000545
4. Smith BE, Suchak M, Siggins D, Challands J. Rectus sheath block for diagnostic laparoscopy. Anaesthesia 1988;43:947-948. https://doi.org/10.1111/j.1365-2044.1988.tb05658.x
5. Fu H, Fu Y, Xu X, Gao Y. Ultrasound-guided rectus sheath block combined with butorphanol for single-incision laparoscopic cholecystectomy: what is the optimal dose of ropivacaine? J Pain Res 2020;13:2609-2615. https://doi.org/10.2147/JPR.S265418
6. Topçu HO, Cavkaytar S, Kokanalı K, Guzel AI, Islimye M, Doganay M. A prospective randomized trial of postoperative pain following different insufflation pressures during gynecologic laparoscopy. Eur J Obstet Gynecol Reprod Biol 2014;182:81-85. https://doi.org/10.1016/j.ejogrb.2014.09.003
7. Shim JW, Jung S, Moon HW, Lee JY, Park J, Lee HM, Kim YS, Hong SH, Chae MS. Rectus sheath block for acute pain management after robot-assisted prostatectomy. Asian J Surg 2022;45:1843-1848. https://doi.org/10.1016/j.asjsur.2021.10.035
8. Cho S, Kim YJ, Jeong K, Moon HS. Ultrasound-guided bilateral rectus sheath block reduces early postoperative pain after laparoscopic gynecologic surgery: a randomized study. J Anesth 2018;32:189-197. https://doi.org/10.1007/s00540-018-2457-0
9. Urmale Kusse A, Legesse M, Assefa A, Tila M, Sintayhu A, Mequanint A, Markos M, Kussia W, Dendir G, Gebremedhin TD, Sidamo T, Obsa MS. Postoperative analgesic effectiveness of ultrasound-guided bilateral erector spinae plane block vs. rectus sheath block for midline abdominal surgery in a low- and middle-income country: a randomised controlled trial. Anaesthesia 2024;79:1292-1299. https://doi.org/10.1111/anae.16421
10. Abbawy M, Okoh D, Binuraj A, Holden F, Fox B, Sachdeva R, Pooni J, Singh M, Allen T, Ganguly S, Gao-Smith F, Veenith T. The role of the rectus sheath block in modern perioperative care for midline laparotomy: a review of the evidence. Front Anesthesiol 2026;5:fanes.2026. https://doi.org/10.3389/fanes.2026.1725241
11. Hamid HK, Ahmed AY, Alhamo MA, Davis GN. Efficacy and safety profile of rectus sheath block in adult laparoscopic surgery: a meta-analysis. J Surg Res 2021;261:10-17. https://doi.org/10.1016/j.jss.2020.12.003
12. Azemati S, Khosravi MB. An assessment of the value of rectus sheath block for postlaparoscopic pain in gynecologic surgery. J Minim Invasive Gynecol 2005;12:12-15. https://doi.org/10.1016/j.jmig.2004.12.013
13. Yoon JP, Kim HY, Jung J, Lee J, Park S, Byeon GJ. Analgesic effect of ultrasound-guided transversus abdominis plane block with or without rectus sheath block in laparoscopic cholecystectomy: a randomized, controlled trial. BMC Anesthesiol 2024;24:203. https://doi.org/10.1186/s12871-024-02590-x
14. Hamill JK, Liley A, Hill AG. Rectus sheath block for laparoscopic appendicectomy: a randomized clinical trial. ANZ J Surg 2015;85:951-956. https://doi.org/10.1111/ans.12950
15. Kim D, Bang S, Chung J, Shin HJ, Lee E. Rectus sheath block provides superior analgesia over quadratus lumborum block in single-port total laparoscopic hysterectomy: a prospective, randomized trial. Korean J Anesthesiol 2025 Aug 22 [Epub]. https://doi.org/10.4097/kja.25174
16. Lavand'homme P. Rebound pain after regional anesthesia in the ambulatory patient. Curr Opin Anaesthesiol 2018;31:679-684. https://doi.org/10.1097/ACO.0000000000000651

eISSN: 2234-2591
Open Access

Case report

Ewha Med J 2026;49(3):e21
https://doi.org/10.12771/emj.2026.01249

The Ewha Medical Journal

Primary breast leiomyosarcoma—pathological challenges and immunohistochemical insights into the diagnosis of a rare tumor: a case report

Ashwini Pitambra[1], Ashutosh Rath[1*], Immanuel Pradeep[1], Krishna Ramavath[2], Chandramouli Ramalingam[3]

[1]*Department of Pathology and Laboratory Medicine, All India Institute of Medical Sciences, Bibinagar, India*
[2]*Department of General Surgery, All India Institute of Medical Sciences, Bibinagar, India*
[3]*Department of Radiation Oncology, All India Institute of Medical Sciences, Bibinagar, India*

Primary leiomyosarcoma of the breast is an extremely rare malignancy, accounting for less than 1% of all breast tumors. Diagnosis is challenging because its morphology overlaps with that of other spindle cell lesions, and standardized treatment guidelines are currently unavailable. A 44-year-old woman presented with a rapidly enlarging, firm, 15×15 cm mass in the left breast. She had previously undergone surgery elsewhere, with diagnoses of leiomyoma and desmoid-type fibromatosis. Imaging demonstrated a lobulated mass without evidence of metastasis. Excision revealed pleomorphic spindle cells arranged in intersecting fascicles, with necrosis and dermal invasion. Primary breast leiomyosarcoma was confirmed by immunohistochemistry, which demonstrated smooth muscle actin and desmin positivity and negative staining for pancytokeratin, p63, S100, CD34, and BCL2. The patient underwent modified radical mastectomy followed by adjuvant radiotherapy and chemotherapy. Primary breast leiomyosarcoma is a rare entity that remains diagnostically challenging. Immunohistochemistry is essential for accurate diagnosis, and optimal management requires a dedicated multidisciplinary approach.

Keywords: Leiomyosarcoma; Spindle cell tumor; Immunohistochemistry; Case reports

Introduction

Background

Primary leiomyosarcoma of the breast is an extremely rare malignant mesenchymal tumor, comprising less than 1% of breast neoplasms. It presents substantial diagnostic and therapeutic challenges because available data are limited and standardized treatment guidelines are lacking [1]. The tumor is thought to arise from smooth muscle cells of the nipple–areolar complex, vessel walls, or mesenchymal stem cells with smooth muscle differentiation [2]. Patients typically present with a rapidly enlarging, painless breast mass, and the diagnosis is often established only after excisional histopathological evaluation because core biopsy and cytology may be misleading [3].

Immunohistochemistry is essential for distinguishing leiomyosarcoma from other spindle cell lesions of the breast [4]. Because of its rarity, treatment strategies are usually extrapolated from soft tissue sarcoma protocols [5]. Although the prognosis may be relatively favorable, biological behavior is unpredictable, with ongoing risks of recurrence and metastasis [6]. Reporting such cases is important for improving diagnostic accuracy and informing management of this rare tumor.

Objectives

This case of primary leiomyosarcoma of the breast highlights the diagnostic challenges associated with this entity and the critical role of immunohistochemistry in establishing the correct diagnosis. This report also describes the management approach used in the absence of standardized guidelines and contributes to the understanding of the clinicopathological features and outcomes of this uncommon spindle cell tumor of the breast.

*Corresponding email: ashutosh.path@aiimsbibinagar.edu.in
Received: March 5, 2026 Revised: April 17, 2026 Accepted: April 24, 2026

Case presentation

Ethics statement

Written informed consent was obtained from the patient for publication of this case report and the accompanying images. All patient-related information has been anonymized to protect privacy and confidentiality in accordance with institutional and international research ethics guidelines. No identifying personal data have been disclosed.

Patient information

A 44-year-old woman presented with an enlarging, firm lump in the upper outer quadrant of the left breast, measuring 15×15 cm, with overlying erythema and a previous surgical scar (Fig. 1). She had a history of recurrent breast lesions, including prior diagnoses of leiomyoma and desmoid-type fibromatosis at an outside facility; both lesions had been managed with lumpectomy. Fine-needle aspiration cytology (FNAC), also performed elsewhere, suggested proliferative breast disease with atypia and prompted further evaluation. The smears could not be reviewed.

Diagnostic assessment

Ultrasonography suggested a Breast Imaging Reporting and Data System category 4B lesion. Positron emission tomography–computed tomography (PET-CT), performed at an outside facility, revealed a 14.8 cm heterogeneously enhancing tumor with lobulated margins and central necrosis. The lesion closely abutted the skin but showed no invasion of the pectoral muscle or adjacent fat planes. Axillary lymph nodes showed no abnormal fluorodeoxyglucose (FDG) uptake and had preserved fatty hila, indicating no metastatic involvement. No additional FDG-avid lesions or tumor deposits were identified elsewhere in the body, suggesting no evidence of disease at other sites.

Core biopsy revealed a malignant spindle cell tumor composed of elongated cells arranged in fascicles, with moderate pleomorphism and 8–10 mitotic figures per 10 high-power fields (HPFs). The differential diagnoses included borderline or malignant phyllodes tumor, metaplastic carcinoma, and other mesenchymal tumors. Immunohistochemistry could not be performed on the biopsy specimen to further characterize the tumor.

The patient underwent left modified radical mastectomy; the resected specimen measured 24×20×11 cm. The tumor measured 15×15×10 cm, occupied a substantial portion of the breast, and was associated with overlying skin ulceration (Fig. 2). Microscopic evaluation confirmed a malignant spindle cell tumor with infiltrative margins. The spindle cells were arranged in fascicles and showed pleomorphic, hyperchromatic, elongated nuclei, high mitotic activity (11 per 10 HPFs; 6/mm^2), and necrosis (Fig. 3A–D). No epithelial component was identified. The tumor invaded the dermis but showed no vascular or lymphatic invasion, and all 9 dissected lymph nodes were uninvolved.

Immunohistochemistry demonstrated positivity for smooth muscle actin (SMA) and desmin, supporting smooth muscle differentiation, whereas staining for pancytokeratin, p63, BCL2, S100, and CD34 was negative (Fig. 4A, B). The Ki-67 labeling index was 15% (Fig. 4C). Based on the histopathological and immunohistochemical findings, the tumor was diagnosed as primary leiomyosarcoma of the breast, grade 2, according to the French Federation of Cancer Centers Sarcoma Group grading system.

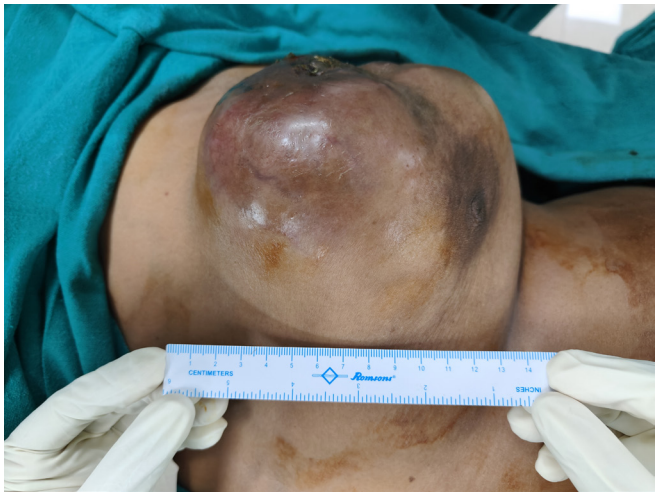

Fig. 1. Clinical image showing a 15×15 cm left breast mass in the upper outer quadrant with overlying erythema and a pre-existing surgical scar.

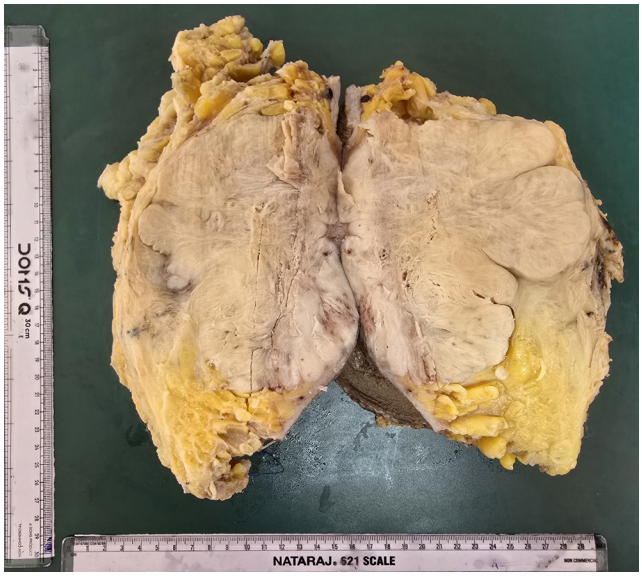

Fig. 2. Gross cut surface showing a firm, gray-white tumor with a whorled appearance.

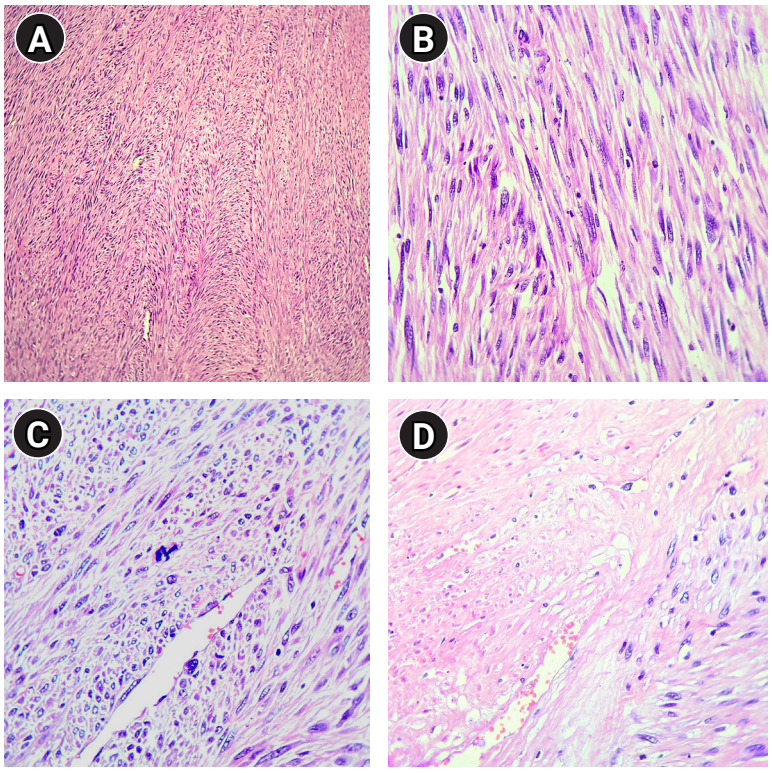

Fig. 3. Histopathological features of primary breast leiomyosarcoma. (A) Interlacing fascicles of spindle cells (hematoxylin and eosin [H&E], ×40). (B) Pleomorphic spindle cells with hyperchromatic nuclei and nuclear atypia (H&E, ×400). (C) Atypical mitotic figure (arrow) (H&E, ×400). (D) Area of tumor necrosis with adjacent viable pleomorphic spindle cells (H&E, ×400).

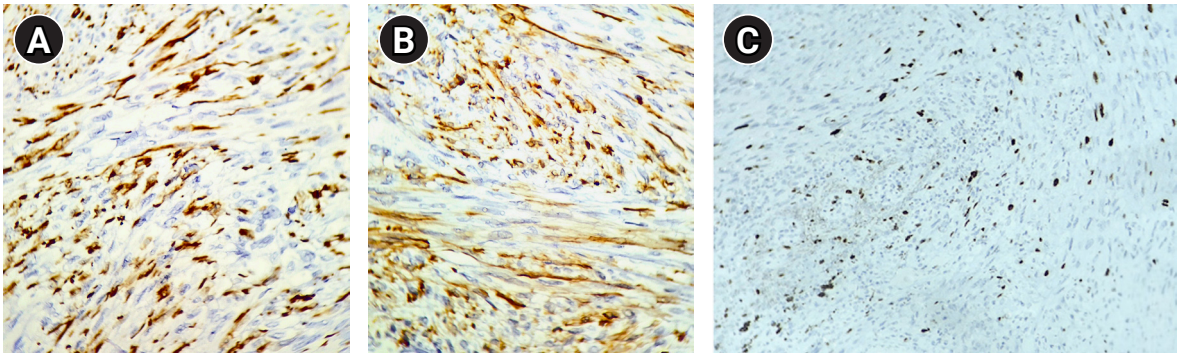

Fig. 4. Immunohistochemical staining of the tumor. (A) Desmin-positive tumor cells (×400). (B) Smooth muscle actin-positive tumor cells (×400). (C) Ki-67 labeling index of 15% in tumor cells (×400).

Therapeutic intervention and follow-up

Given the high-grade features, large tumor size (> 10 cm; pT3), and moderate proliferative activity, a multimodal treatment approach was planned. Because no standardized treatment guidelines exist specifically for primary breast leiomyosarcoma, management was extrapolated from established soft tissue sarcoma protocols after multidisciplinary team discussion, consistent with current oncological practice for rare sarcomas [1,5]. Adjuvant radiotherapy (60 Gy in 30 fractions) was administered to the chest wall because of the close surgical margins (0.3 cm) and to reduce the risk of local recurrence. Ultrasonography performed after completion of radiotherapy showed a postoperative hypoechoic collection suggestive of a seroma, measuring 3.3 × 0.6 cm, at the surgical scar site, with no evidence of calcification or vascularity. Subsequently, whole-body FDG PET-CT showed FDG-avid thickening and subcutaneous fat stranding in the left chest wall, with a maximum standardized uptake value of 5.3. Close follow-up of the lesion was advised. The patient then underwent 6 cycles of doxorubicin, ifosfamide, and mesna (AIM) chemotherapy. She tolerated radiotherapy and chemotherapy well. Supportive

care included mesna for uroprotection during ifosfamide therapy and granulocyte colony-stimulating factor support with pegfilgrastim or filgrastim to prevent neutropenia. Ultrasonography performed after completion of 2 chemotherapy cycles showed mild subcutaneous edema at the skin incision site and no postoperative collection. At follow-up after completion of chemotherapy, a local clinical examination showed no evidence of disease. The patient was advised to undergo PET-CT as part of follow-up assessment of disease status.

Discussion

Primvary sarcomas are rare tumors that may arise in any organ; however, occurrence in the breast is exceptionally uncommon, accounting for nearly 1% of breast malignancies and fewer than 5% of all soft tissue sarcomas [1]. The clinical presentation is often nonspecific, and most patients present with an enlarging, painless breast mass, as in the present case. Reported tumor sizes range from 0.3 to 16 cm, with a mean size of 4.7 cm [2]. Although these tumors predominantly affect women, rare cases have also been reported in men [3].

The tumor is believed to arise from smooth muscle cells of the lactiferous ducts, blood vessels, or erector pili muscles in the periareolar region [4]. Secondary cases may develop after prior radiotherapy or in the setting of chronic lymphedema [5]. Imaging modalities such as mammography and ultrasonography generally lack specificity and may lead to misclassification as fibroadenoma or phyllodes tumor, further complicating diagnosis [6].

The patient's previous outside diagnoses of leiomyoma and desmoid-type fibromatosis warrant consideration. Because the original slides from these lesions were not available for review, definitive retrospective reclassification was not possible. Synchronous or metachronous tumors are very rare. A literature search identified no reports of synchronous or metachronous breast spindle cell neoplasms with differing histologic diagnoses. Therefore, the prior diagnoses may have reflected sampling error or may have been rendered without immunohistochemical support.

The initial cytological evaluation in this case reportedly showed spindle-shaped cells arranged in fascicles with blunt-ended nuclei. However, FNAC has substantial diagnostic limitations in such cases because of cytomorphological overlap with other spindle cell lesions of the breast [7]. Under the Yokohama System for Reporting Breast Fine-Needle Aspiration Biopsy Cytopathology, spindle cell tumors may be classified as "suspicious for malignancy" or "malignant," depending on the degree of cellular atypia and the presence of mitotic activity or necrosis [8]. The absence of epithelial elements in the smears, together with pleomorphic spindle cells in clusters, may support classification in the "malignant" category. According to the World Health Organization Reporting System for Soft Tissue Cytopathology, such a lesion may be categorized as a soft tissue neoplasm of uncertain malignant potential if only mildly pleomorphic spindle cells are observed. However, if significant nuclear atypia is present, the tumor would be categorized as "suspicious for malignancy." If mitotic figures and/or necrosis are evident, although these features are often difficult to appreciate cytologically, the lesion would be classified as "malignant" [9].

Several spindle cell lesions should be considered in the cytological differential diagnosis. Metaplastic carcinoma may mimic sarcoma cytologically, with pleomorphic spindle cells, vacuolated cytoplasm, and occasional epithelial clusters. Malignant phyllodes tumor, a relatively more common entity in this setting, should be carefully excluded. It typically shows atypical spindle nuclei within stromal fragments and numerous naked nuclei in a hypercellular background. In contrast, leiomyosarcoma is more likely to show cohesive clusters and fascicles of pleomorphic spindle cells. Undifferentiated pleomorphic sarcoma shows marked pleomorphism and bizarre multinucleated giant cells [10]. Benign spindle cell lesions, such as fibromatosis, show bland, uniform spindle cells without significant pleomorphism or mitotic activity; accurate identification is therefore important to avoid overtreatment. Thus, FNAC alone is often insufficient for a definitive diagnosis, and histological confirmation by core needle or excisional biopsy, together with immunohistochemistry, is required [11].

Core needle biopsy was subsequently performed in this case. Although core biopsy provides better architectural assessment than FNAC, diagnostic limitations remain, particularly because primary sarcomas such as leiomyosarcoma lack ductal epithelial elements. This absence can create diagnostic uncertainty and make it difficult to distinguish sarcoma from metaplastic carcinoma, which often contains an epithelial component. Therefore, correlation with definitive excisional histopathology and immunohistochemistry is essential [12].

Histopathological examination of the surgical specimen in leiomyosarcoma typically shows intersecting fascicles of spindle cells with eosinophilic cytoplasm, elongated blunt-ended nuclei, moderate to severe nuclear atypia, brisk mitotic activity, and/or necrosis [13]. In the present case, no lymph node involvement was identified, consistent with the general observation that nodal metastasis is uncommon in breast leiomyosarcoma [2].

Because of overlapping histological appearances, several benign and malignant spindle cell tumors of the breast must be excluded. Fibromatosis typically shows uniform, bland spindle cells with β-catenin and SMA positivity but is negative for desmin and S100

Table 1. Comparative immunohistochemical profiles of spindle cell lesions in the differential diagnosis of primary breast leiomyosarcoma

Entity	SMA	Desmin	h-caldesmon	Pan-CK	p63	S100	CD34	β-catenin
LMS	+	+	+	–	–	–	–	–
Metaplastic carcinoma	+	–	–	+	+	–	–	–
Malignant phyllodes tumor	V	–	–	–	–	–	+	V
Fibromatosis	+	–	–	–	–	–	–	+ (nuclear)
MPNST	–	–	–	–	–	+ (focal)	V	–
This case	+	+	ND	–	–	–	–	ND

SMA, smooth muscle actin; Pan-CK, pancytokeratin; LMS, leiomyosarcoma; +, positive; –, negative; V, variable; MPNST, malignant peripheral nerve sheath tumor; ND, not done.

[14]. Nodular fasciitis is characterized by plump spindle cells in a myxoid stroma, with SMA positivity and negative β-catenin and S100 expression. Myofibroblastoma is usually well circumscribed and is immunoreactive for desmin, CD34, estrogen receptor, and progesterone receptor [15].

Among malignant differential diagnoses, metaplastic carcinoma is particularly challenging because it may show a monophasic spindle cell pattern that histologically mimics sarcoma. It is usually positive for cytokeratin and p63 and negative for S100. Malignant phyllodes tumor demonstrates stromal overgrowth and scant epithelial elements, with CD34 and SMA positivity. Malignant peripheral nerve sheath tumor (MPNST) shows wavy spindle cells with frequent mitoses and is positive for S100 and SOX10 [10]. In addition, neurotrophic tyrosine receptor kinase fusion-positive sarcomas may show minimal pleomorphism and fascicular architecture and require molecular confirmation because of potential therapeutic implications [16]. In the present case, adequate sampling and immunohistochemistry were decisive in confirming the diagnosis. The tumor showed diffuse immunoreactivity for SMA and desmin, supporting smooth muscle lineage. Negative immunostaining for pancytokeratin, p63, BCL2, S100, and CD34 helped exclude metaplastic carcinoma, phyllodes tumor, and MPNST. Fibromatosis was not favored in the present case because of marked nuclear pleomorphism, necrosis, and mitotic activity. Table 1 summarizes the key immunohistochemical profiles of the main spindle cell lesions in the differential diagnosis.

Surgical excision with clear margins remains the mainstay of treatment. Modified radical mastectomy was performed in the present case and is the most frequently adopted approach. Wide local excision may be feasible for smaller tumors. Achieving negative surgical margins is critical because it substantially reduces local recurrence rates [1]. The roles of chemotherapy and radiotherapy are not well established because of limited evidence. However, anthracycline-based chemotherapy is often used in high-risk or metastatic cases, whereas radiotherapy may be considered for positive margins or larger tumors [17]. In the present case, radiotherapy was selected because of the close surgical margins and large tumor size, and AIM chemotherapy was selected because of the high-grade histology and large tumor burden, following general soft tissue sarcoma management principles in the absence of breast leiomyosarcoma-specific guidelines [1].

The prognosis of breast leiomyosarcoma is generally favorable compared with that of other soft tissue sarcomas. However, hematogenous metastasis occurs in approximately 25% of cases, most commonly involving the lungs, liver, and bones. Metastases may develop years after initial treatment, emphasizing the need for long-term surveillance [2]. Because of the rarity of this tumor, current treatment protocols are largely extrapolated from soft tissue sarcoma guidelines, underscoring the need for additional studies and accumulated case experience to guide standardized management [1].

In conclusion, primary leiomyosarcoma of the breast is a rare malignancy that poses significant diagnostic and therapeutic challenges. Accurate diagnosis relies on histopathological and immunohistochemical evaluation because conventional imaging and cytology may be inconclusive. Given the absence of standardized treatment guidelines, management is generally adapted from soft tissue sarcoma protocols, with complete surgical excision remaining the mainstay of treatment. Owing to the risk of recurrence and metastasis, multidisciplinary management and long-term follow-up are essential to optimize patient outcomes.

ORCID

Ashwini Pitambra: https://orcid.org/0009-0009-7138-4439
Ashutosh Rath: https://orcid.org/0000-0001-6255-8286
Immanuel Pradeep: https://orcid.org/0000-0002-9652-0179
Krishna Ramavath: https://orcid.org/0000-0002-1670-3902
Chandramouli Ramalingam: https://orcid.org/0009-0003-5131-1212

Authors' contribution

AP and AR contributed to manuscript preparation and histo-

pathological diagnosis. IP assisted in histopathological diagnosis. KR was involved in surgical management and provided clinical images. CR contributed radiation oncology expertise. All authors participated in manuscript drafting and revision, and all have read and approved the final manuscript.

Conflict of interest

No potential conflict of interest relevant to this article was reported.

Funding

No external funding was received for this study.

Data availability

Not applicable.

Acknowledgments

None.

Supplementary materials

None.

References

1. Alimi A, Abbassi H, Abid S, Dinari A, Khlifi A, Hidar S, Boughizane S, Khairi H. Leiomyosarcoma of the breast: case report and review of the literature. Eur J Breast Health 2025;21:277-280. https://doi.org/10.4274/ejbh.galenos.2025.2024-10-8
2. Masadah R, Anwar F, Nelwan BJ, Faruk M. Primary leiomyosarcoma of the breast: a case report and literature review. Int J Surg Case Rep 2023;106:108290. https://doi.org/10.1016/j.ijscr.2023.108290
3. Ely Cheikh T, Hamza K, Hicham B, Fatiha EM, Hajar EO, Mustapha B, Mohamed E, Mohamed E. Leiomyosarcoma of the male breast: case report. Ann Med Surg (Lond) 2021;67:102495. https://doi.org/10.1016/j.amsu.2021.102495
4. Sethi E, Misra S, Ahuja A. Primary leiomyosarcoma with osteosarcomatous differentiation of the breast. Autops Case Rep 2024;14:e2024476. https://doi.org/10.4322/acr.2024.476
5. Hayashi S, Kitada M, Matsuda Y, Ishibashi K, Takahashi N. Leiomyosarcoma arising in irradiated region after breast-conserving surgery: a case report. Surg Case Rep 2015;1:76. https://doi.org/10.1186/s40792-015-0072-y
6. Khan M, Siddiqui B, Rafey M, Hassan M, Faridi S. A rare case report of primary breast leiomyosarcoma presenting clinicoradiologically as phyllodes tumour. Indian J Pathol Oncol 2025;12:86-89. https://doi.org/10.18231/j.ijpo.2025.019
7. Jun Wei X, Hiotis K, Garcia R, Hummel Levine P. Leiomyosarcoma of the breast: a difficult diagnosis on fine-needle aspiration biopsy. Diagn Cytopathol 2003;29:172-178. https://doi.org/10.1002/dc.10359
8. Yu W, Gan Q, Gong Y. The Yokohama system for reporting breast cytopathology. J Clin Transl Pathol 2023;3:99-105. https://doi.org/10.14218/JCTP.2023.00006
9. Bui MM. World Health Organization Reporting System for Soft Tissue Cytopathology: a concise review with a practical diagnostic approach. J Clin Transl Pathol 2025;5:72-78. https://doi.org/10.14218/JCTP.2025.00016
10. Rakha EA, Brogi E, Castellano I, Quinn C. Spindle cell lesions of the breast: a diagnostic approach. Virchows Arch 2022;480:127-145. https://doi.org/10.1007/s00428-021-03162-x
11. Gupta RK, Kenwright D, Naran S, Lallu S, Fauck R. Fine needle aspiration cytodiagnosis of leiomyosarcoma of the breast: a case report. Acta Cytol 2000;44:1101-1105. https://doi.org/10.1159/000328606
12. Sandhya B, Babu V, Parthasarathy G, Kate V, Ananthakrishnan N, Krishnan R. Primary leiomyosarcoma of the breast: a case report and review of literature. Indian J Surg 2010;72:286-288. https://doi.org/10.1007/s12262-010-0092-6
13. Tharwani ZH, Habib Z, Ahmed Y, Ishrat S, Nashwan AJ. A rare case of high-grade spindle cell sarcoma of the breast: a case report. Case Rep Oncol 2024;17:217-224. https://doi.org/10.1159/000536125
14. Ni Y, Tse GM. Spindle cell lesions of the breast: a diagnostic algorithm. Arch Pathol Lab Med 2023;147:30-37. https://doi.org/10.5858/arpa.2022-0048-RA
15. Hou Y, Li Z. Spindle cell lesions of the breast. Hum Pathol Rep 2021;26:300565. https://doi.org/10.1016/j.hpr.2021.300565
16. Schwartz CJ, Ye J, Devine WP, Chen YY. NTRK-fusion spindle cell tumour in the breast: expanding the differential of challenging spindle cell lesions on core biopsy. Histopathology 2025;86:1018-1021. https://doi.org/10.1111/his.15421
17. Samenova D, Midlenko A, Khamzina Y, Kaldybayev M, Khamzina S. Primary leiomyosarcoma of the breast: a successful surgical treatment in a 45-year-old woman. Am J Case Rep 2023;24:e939437. https://doi.org/10.12659/AJCR.939437

eISSN: 2234-2591
Open Access

Case report

Ewha Med J 2026;49(3):e22
https://doi.org/10.12771/emj.2026.01347

The Ewha Medical Journal

Metastatic appendiceal mucinous adenocarcinoma presenting as bilateral ovarian masses mimicking advanced ovarian cancer: a case report

Naina Kumar[1*], Gunvanti Rathod[2], Annapurna Srirambhatla[3], Mishu Mangla[1], Nireesha Bukke[1], Pooja Tejappa Rathod[1]

[1]*Department of Obstetrics and Gynecology, All India Institute of Medical Sciences, Bibinagar, India*
[2]*Department of Pathology, All India Institute of Medical Sciences, Bibinagar, India*
[3]*Department of Radiodiagnosis, All India Institute of Medical Sciences, Bibinagar, India*

Appendiceal mucinous adenocarcinoma is a rare gastrointestinal malignancy that may metastasize to the ovaries and closely mimic advanced primary ovarian cancer, creating diagnostic and therapeutic challenges. A 61-year-old postmenopausal woman presented with postmenopausal bleeding, abdominal distension, abdominal pain, and weight loss. Imaging demonstrated bilateral adnexal masses with omental caking and ascites, suggestive of advanced ovarian malignancy. Cancer antigen 125 was elevated, and carcinoembryonic antigen (CEA) levels were markedly increased. She had a history of acute appendicitis 1 year earlier. Biopsy revealed mucinous adenocarcinoma with signet-ring cells. Endoscopic evaluation was unremarkable. Despite neoadjuvant chemotherapy for presumed ovarian cancer, the disease progressed, necessitating cytoreductive surgery. Histopathological examination demonstrated bilateral mucinous adenocarcinoma with peritoneal spread. Immunohistochemistry showed positivity for cytokeratin 20, caudal-type homeobox 2, and special AT-rich sequence-binding protein 2 and negativity for cytokeratin 7 and paired-box gene 8, supporting an appendiceal origin. She was started on fluorouracil, leucovorin, and oxaliplatin chemotherapy. Metastatic appendiceal carcinoma can closely resemble primary ovarian malignancy. Bilateral mucinous ovarian tumors with elevated CEA levels and poor chemotherapy response should prompt evaluation for a gastrointestinal primary tumor.

Keywords: Appendiceal carcinoma; Metastasis; Mucinous adenocarcinoma; Primary ovarian cancer; Signet-ring cells; Case reports

Introduction

Metastatic involvement of the ovaries most commonly arises from primary tumors of the gastrointestinal (GI) tract and can masquerade as primary ovarian neoplasms, creating a substantial diagnostic challenge [1,2]. Appendiceal tumors are a rare and heterogeneous group of neoplasms, accounting for approximately 0.9%–1.4% of all appendectomy specimens [3]. They are often discovered incidentally during appendectomy or on subsequent histopathological evaluation. Although their exact etiology remains unclear, chronic inflammation, mucosal hyperplasia, and underlying genetic alterations have been implicated. The risk increases with advancing age, and a slight female predominance has been reported [3].

Within this spectrum, appendiceal mucinous neoplasms represent a distinctive subtype, with ovarian metastases reported in nearly 50% of affected patients [4]. When metastatic spread to the ovaries occurs, these lesions frequently mimic primary mucinous ovarian tumors, creating considerable diagnostic difficulty. This difficulty reflects their nonspecific clinical presentation, overlapping radiological features, similar histomorphological findings, and substantial immunohistochemical overlap with primary ovarian tumors [1,2].

Overall, metastatic tumors constitute approximately 5%–30%

*Corresponding email: drnainakumar@gmail.com
Received: February 21, 2026 Revised: June 5, 2026 Accepted: June 5, 2026

of all malignant ovarian neoplasms [2]. Secondary mucinous ovarian tumors most commonly originate from the breast, colon, and stomach, whereas the appendix accounts for approximately 3%–7% of metastatic cases [2].

Against this background, we report a case that was initially treated as primary ovarian carcinoma on the basis of clinical and radiological findings but was ultimately diagnosed as metastatic mucinous adenocarcinoma of probable appendiceal origin. This case underscores the diagnostic challenges in differentiating primary from secondary ovarian tumors.

Case presentation

A 61-year-old postmenopausal woman (para 4, with 3 living children) presented to the gynecology outpatient department with postmenopausal bleeding for 2–3 days. She reported a similar self-limited episode 5 months earlier. The bleeding was associated with progressively worsening abdominal pain and distension for the preceding 2 months, along with decreased appetite, bloating, and weight loss. She had no history of rectal bleeding, vomiting, or altered bowel habits. She had no significant history of hypertension, diabetes mellitus, or other chronic comorbidities. There was no family history of ovarian, breast, or GI malignancy in first- or second-degree relatives.

She had undergone laparoscopic appendiceal biopsy 1 year earlier for abdominal pain at a private hospital. Preoperative contrast-enhanced computed tomography (CECT) at that time showed a thickened appendix with periappendiceal inflammatory changes and a cystic collection suggestive of an appendicular abscess. The remaining organs, including the liver, gallbladder, spleen, adrenal glands, pancreas, kidneys, bowel, urinary bladder, uterus, and ovaries, were normal. A small 1×1.2-cm fibroid was observed in the fundal region. Intraoperatively, only an appendiceal biopsy was obtained, and appendectomy was not performed. Histopathological examination revealed acute nonspecific inflammation, after which her symptoms improved with antibiotics.

Clinical examination

On general examination, the patient was conscious and oriented, with an average build and a body mass index of 21.6 kg/m^2. There was no pallor, icterus, or pedal edema. Vital signs were stable: blood pressure, 110/80 mm Hg; pulse rate, 79 beats/min; and respiratory rate, 16 breaths/min. Cardiovascular and respiratory examinations were unremarkable.

Abdominal examination revealed a firm abdominopelvic mass corresponding to a 24–26-week gravid uterus. The mass was predominantly solid, had restricted mobility, and showed no side-to-side movement.

Local examination showed thinned and atrophic labia majora and minora, consistent with estrogen-deficient vulvar changes. Speculum examination revealed a normal-appearing vagina and cervix. Bimanual examination demonstrated a bulky uterus, equivalent to 8–10 weeks' gestational size, displaced anteriorly by a large, predominantly solid mass measuring approximately 10×12 cm. The mass occupied the pouch of Douglas and extended into both fornices, more prominently on the right than on the left, and was densely adherent to the posterior surface of the uterus.

Investigations

Pelvic ultrasonography (USG) revealed a retroflexed uterus measuring 7.4×3.7 cm, with an endometrial thickness (ET) of 8 mm. A large, heterogeneously hypoechoic solid pelvic mass measuring 15.9×9.7×11 cm with increased internal vascularity was noted. Neither ovary was visualized separately, and mild ascites was present. These findings were suggestive of ovarian malignancy.

CECT of the abdomen and pelvis showed a large, lobulated, heterogeneously hypodense pelvic mass measuring 10.6×9.9×8.9 cm, with peripheral enhancement and nonenhancing cystic/necrotic areas. The lesion abutted the uterus posteriorly, the bladder inferiorly, and the iliac vessels and ureters laterally, with loss of the intervening fat plane between the lesion and bladder. Moderate ascites was present, along with thickened nodular omentum suggestive of omental caking. Neither ovary was visualized separately. The uterus measured 82×32×38 mm and contained a small fibroid measuring 23×23×32 mm. The liver, gallbladder, spleen, pancreas, and kidneys appeared normal. Overall, the findings were consistent with advanced ovarian malignancy with peritoneal carcinomatosis.

Magnetic resonance imaging (MRI) of the abdomen and pelvis revealed a uterus measuring 80×26×40 mm, with a 23×24-mm intramural fibroid in the fundal region and an ET of 6.3 mm. MRI characterized the lesion as a large, irregular, lobulated, solid-cystic mass measuring 11.5×10×8.9 cm. The mass was T1 hypointense and T2 hyperintense, with diffusion restriction, an apparent diffusion coefficient of 1.2×10^{-3} mm^2/sec, and heterogeneous contrast enhancement. Neither ovary was visualized separately. Infiltration of the posterior uterine wall, omental caking, and serosal deposits over the cecum and appendix were noted. No significant pelvic lymphadenopathy was seen (Fig. 1A–D).

Routine laboratory investigations, including a complete blood count, liver and renal function tests, coagulation profile, blood glucose testing, and viral serology, were within normal limits. Tu-

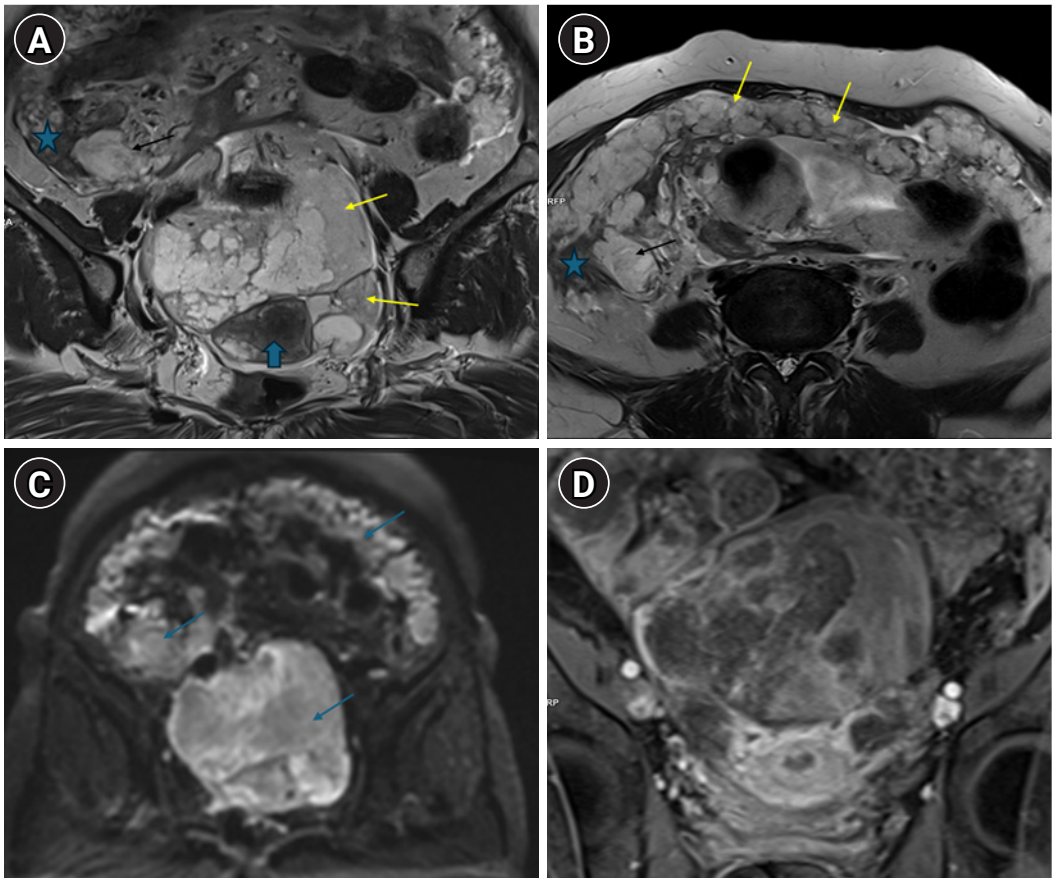

Fig. 1. Magnetic resonance imaging findings. (A) Coronal T2-weighted image showing bilateral T2-hyperintense ovarian mass lesions (yellow arrows). The mass (black arrow) infiltrates the cecum (blue asterisk). The appendix is not separately visualized. The blue block arrow indicates the uterus. (B) Axial T2-weighted image showing a tumor deposit (black arrow) infiltrating the cecum (blue asterisk), with omental deposits resulting in caking (yellow arrows). (C) Axial diffusion-weighted image at a high b-value of 1,000 s/mm^2 showing restricted diffusion in the omentum, ovarian mass lesions, and cecal deposit. (D) Coronal contrast-enhanced T1-weighted fat-saturated image showing heterogeneous enhancement of the ovarian mass.

mor markers showed elevated cancer antigen 125 (CA-125; 213 U/mL) and markedly elevated carcinoembryonic antigen (CEA; 144 ng/mL), whereas carbohydrate antigen 19-9 (CA 19-9) was normal (0.6 U/mL). The Pap smear was negative for intraepithelial lesions.

Management

In view of the findings suggestive of presumed FIGO stage IIIC ovarian malignancy, the patient was scheduled for endometrial biopsy and USG-guided biopsy of the abdominal lesion, followed by 3 cycles of neoadjuvant chemotherapy (NACT) and interval cytoreductive surgery. Histopathological examination of the endometrial biopsy showed atrophic endometrium, whereas biopsy of the abdominal lesion revealed mucin-secreting adenocarcinoma with signet-ring cells. To evaluate a possible GI primary tumor and rule out secondary ovarian involvement, upper GI endoscopy and colonoscopy were performed. Upper GI endoscopy demonstrated grade A esophagitis with gastric erythema, whereas colonoscopy was unremarkable, with no significant abnormalities detected. Immunohistochemical (IHC) analysis was not performed on the preoperative abdominal lesion biopsy specimen because the biopsy material was limited and the initial clinical-radiological impression favored advanced ovarian malignancy.

Moreover, the patient had large bilateral adnexal masses, elevated CA-125 levels, ascites, omental caking, and peritoneal carcinomatosis, all of which strongly suggested advanced epithelial ovarian cancer. Because endoscopic evaluation did not identify a definite GI primary lesion, the patient was started on NACT for presumed primary ovarian malignancy with paclitaxel 250 mg and carboplatin 400 mg every 21 days for 3 cycles. After the second chemotherapy cycle, she developed deep vein thrombosis (DVT) of the right lower limb. Rivaroxaban was initiated at 15 mg twice

daily for 21 days, followed by 20 mg once daily. After stabilization, the third chemotherapy cycle was administered as planned.

After completion of 3 cycles of NACT, the patient underwent reassessment. Routine laboratory investigations, including a complete blood count, liver and renal function tests, coagulation profile, and 2-dimensional echocardiography, were within acceptable limits. Venous Doppler examination of both lower limbs showed no residual thrombosis.

Tumor marker evaluation showed an increase in CA-125 to 404 U/mL, whereas CEA decreased to 55.35 ng/mL. Repeat pelvic USG demonstrated a solid, irregularly shaped, heterogeneously echogenic lesion measuring 13.9×9.7×13 cm in the suprapubic region. Nodular hypoechoic plaque-like thickening was noted along the anterior abdominal wall and periphery, suggestive of persistent omental caking. The uterus was visualized separately from the lesion, with an ET of 4 mm. Table 1 summarizes the clinical, radiological, and biochemical parameters evaluated before and after NACT.

Because no significant radiological response was observed and bulky disease persisted after NACT, interval cytoreductive surgery was planned.

Intraoperative assessment revealed multiple dense adhesions between the bowel loops and the pelvic mass. Mild-to-moderate ascites of approximately 150 mL was present, and approximately 10 mL of peritoneal fluid was aspirated and sent for cytological analysis. A large omental cake measuring approximately 20×18 cm, densely studded with tumor deposits, was adherent to the ovarian mass. A 15×10-cm solid mass was noted arising from the right ovary; it was densely adherent to the posterior uterine surface and adjacent bowel loops, with the right fallopian tube stretched over the mass. A separate 5×6-cm solid mass was identified arising from the left ovary and was densely adherent to the posterior uterine surface, bowel, and left lateral pelvic wall. The uterus appeared bulky, corresponding to approximately 8–10 weeks' gestational size, and contained a 4×3-cm fundal fibroid (Fig. 2A, B). Both round ligaments were thickened, and multiple metastatic deposits were observed over the parietal peritoneum, bowel serosa, appendix, pouch of Douglas, and undersurface of the liver and diaphragm.

Total abdominal hysterectomy with bilateral salpingo-oophorectomy, appendectomy, and infracolic omentectomy was performed. Maximal cytoreduction was performed by removing most visible tumor deposits, except for lesions that densely infiltrated the bowel and liver parenchyma.

Gross examination revealed an irregular, globular mass involving the right ovary and measuring 15×14×8 cm, with a yellow-to-mucoid cut surface and focal calcification. The left ovarian mass measured 9×7×4.5 cm and had a similar yellow-mucoid solid appearance, with focal hemorrhagic and calcific areas. Microscopic evaluation supported mucinous adenocarcinoma in-

Table 1. Comparison of investigational findings before and after neoadjuvant chemotherapy

Investigation	Pre-NACT findings	Post-NACT findings/reassessment	Inference/response
Pelvic USG	Large heterogeneously hypoechoic solid pelvic mass measuring 15.9×9.7×11 cm, with internal vascularity; ovaries not visualized separately; mild ascites	Solid, irregular, heterogeneously echogenic lesion measuring 13.9×9.7×13 cm; nodular plaque-like thickening suggestive of persistent omental caking; uterus visualized separately; ET 4 mm	No significant size reduction; persistent bulky disease
CECT of the abdomen and pelvis	Lobulated heterogeneously hypodense pelvic mass measuring 10.6×9.9×8.9 cm, with peripheral enhancement and necrotic areas; moderate ascites; omental caking; loss of fat planes; ovaries not visualized separately	Not repeated	Baseline advanced disease
MRI of the abdomen and pelvis	Large, irregular, lobulated, solid-cystic mass measuring 11.5×10×8.9 cm; T1 hypointense and T2 hyperintense, with diffusion restriction; posterior uterine wall infiltration; serosal deposits over the cecum and appendix; omental caking	Not repeated	Extensive baseline disease burden
CA-125	213 U/mL	Increased to 404 U/mL	Biochemical progression
CEA	144 ng/mL	Decreased to 55.35 ng/mL	Partial biochemical response; supports a GI primary
CA 19-9	Normal, 0.6 U/mL	Not repeated	-
Venous Doppler	Not applicable	No residual thrombosis after DVT treatment	Stabilized complication

NACT, neoadjuvant chemotherapy; USG, ultrasonography; ET, endometrial thickness; CECT, contrast-enhanced computed tomography; MRI, magnetic resonance imaging; CA-125, cancer antigen 125; CEA, carcinoembryonic antigen; GI, gastrointestinal; CA 19-9, carbohydrate antigen 19-9; DVT, deep vein thrombosis.

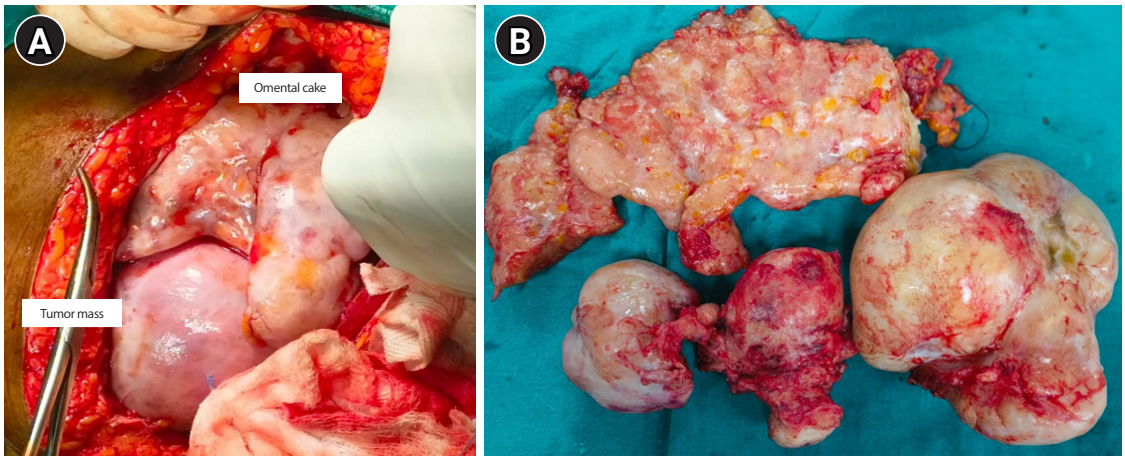

Fig. 2. Intraoperative and specimen findings. (A) Intraoperative finding showing a large omental cake and tumor mass. (B) Surgical specimen showing the uterus and cervix, bilateral ovarian masses, omental cake, and appendix.

volving both ovaries, with intact capsules.

The right fallopian tube measured 6×0.5 cm and showed serosal deposits without invasion of the tubal wall. The uterus measured 10.5×9×4 cm and had multiple serosal deposits; on cut section, the endometrium measured 2 mm in thickness, and the myometrium measured 2 cm in thickness. The external cervical surface also showed tumor deposits, although the cervical cut section was unremarkable. The left fallopian tube measured 7×0.5 cm and similarly showed serosal deposits without invasion of the tubal wall. A large omental cake measuring 24×14×3 cm was extensively infiltrated by tumor deposits and appeared grayish-yellow. The appendix showed tumor involvement with histological features similar to those of the ovarian masses (Fig. 3A–D). In addition, the parietal peritoneum, bilateral parametrium, and all excised deposits showed involvement by mucinous adenocarcinoma. Cytological examination of peritoneal fluid was positive for malignant cells.

On the basis of these findings, the initial histopathological diagnosis was mucinous adenocarcinoma, grade 2, International Federation of Gynecology and Obstetrics (FIGO) stage IIIC, involving both ovaries. To determine whether the tumor represented a primary ovarian malignancy or secondary ovarian involvement, IHC was performed. Tumor cells showed strong positivity for cytokeratin 20 (CK20), special AT-rich sequence-binding protein 2 (SATB2), and caudal-type homeobox 2 (CDX2), and were negative for cytokeratin 7 (CK7) and paired-box gene 8 (PAX8) (Fig. 4A–E). Together with the clinical and radiological findings and the absence of colorectal pathology on colonoscopy, these findings supported a diagnosis of metastatic mucinous adenocarcinoma involving both ovaries, most likely of appendiceal origin.

The patient was discharged in stable condition after suture removal and was subsequently started on 5-fluorouracil (5-FU), leucovorin, and oxaliplatin (FOLFOX) chemotherapy every 14 days. The regimen consisted of oxaliplatin 120 mg intravenously on day 1, leucovorin 550 mg intravenously on day 1, a 5-FU bolus of 550 mg intravenously on day 1, followed by a 5-FU infusion of 3,200 mg over 46 hours. A total of 12 cycles over 6 months was planned, with ongoing clinical and laboratory monitoring to assess tolerance and response. The patient is currently undergoing regular follow-up and has completed 9 cycles of FOLFOX chemotherapy. She is tolerating chemotherapy well, without major adverse effects, and has had significant improvement in abdominal symptoms and ascites. Positron emission tomography/computed tomography is planned after completion of the final chemotherapy cycle to evaluate treatment response and current disease status.

Ethics statement

According to institutional policy, ethical approval is not required for single case reports. Written informed consent was obtained for publication of this case and the accompanying clinical data and images.

Discussion

Metastatic tumors involving the ovary account for approximately 10%–25% of all ovarian malignancies [5]. They arise from a wide range of primary sites, most commonly the breast, colorectum, stomach, and endometrium, with less frequent origins including the small intestine, appendix, pancreas, biliary tract, and lung [6].

Appendiceal cancer is rare, with an incidence of 1–2 per mil-

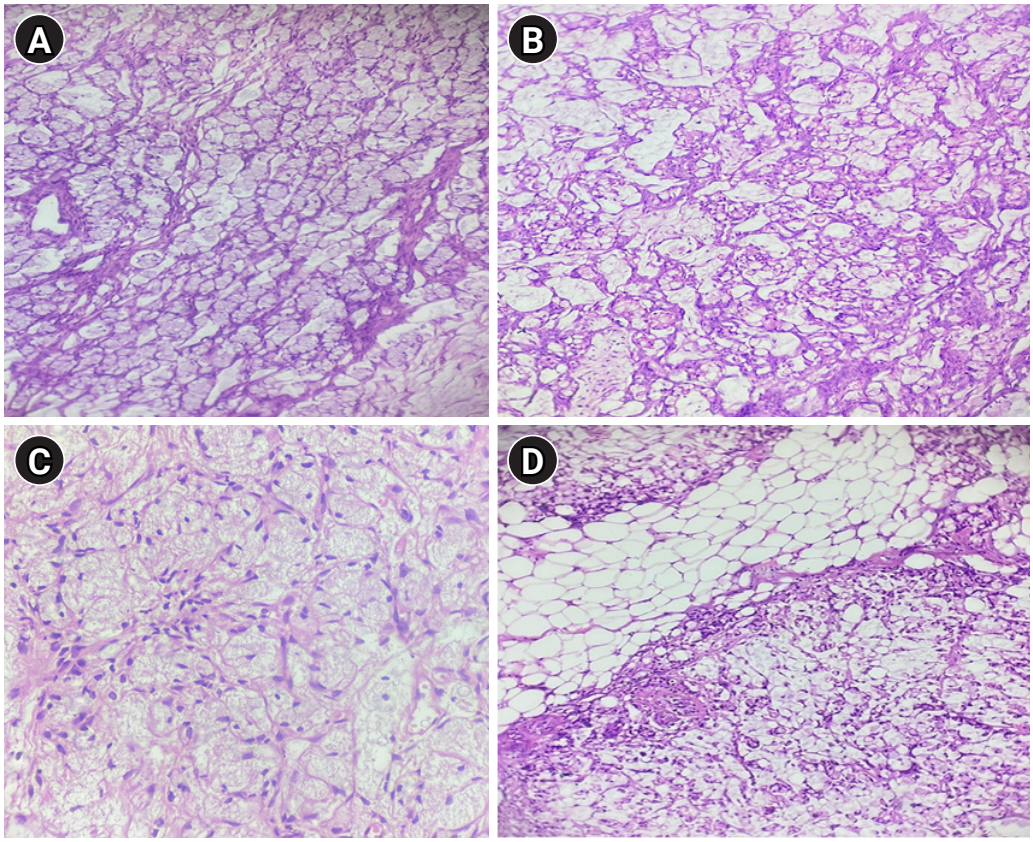

Fig. 3. Histopathological findings. (A) Mucinous adenocarcinoma involving the right ovary demonstrating intracellular mucin, marked nuclear atypia, prominent nucleoli, and abnormal mitotic activity in tumor cells (hematoxylin and eosin [H&E], ×10). (B) Section of mucinous adenocarcinoma involving the left ovary showing complex glandular architecture with stratified atypical mucin-secreting epithelial cells, nuclear pleomorphism, and stromal invasion (H&E, ×10). (C) Section of the appendix showing tumor cells with abundant intracellular and extracellular mucin and floating tumor cells with signet-ring cell morphology (H&E, ×10). (D) Section showing fibromuscular and collagenous omental tissue infiltrated by malignant tumor cells of mucinous adenocarcinoma (H&E, ×10).

lion, and encompasses a heterogeneous spectrum ranging from low-grade appendiceal mucinous neoplasms to high-grade adenocarcinomas [7,8]. According to the Surveillance, Epidemiology, and End Results (SEER) database, epithelial adenocarcinoma is the most frequent broad histologic category, with mucinous adenocarcinoma representing the predominant epithelial subtype (37%) [5,9]. In contrast, when all appendiceal neoplasms are considered irrespective of histology, carcinoid (neuroendocrine) tumors are the most common, accounting for approximately 66% of cases, followed by cystadenocarcinomas (20%) and adenocarcinomas (10%) [10].

The most frequent pattern of spread involves the peritoneal cavity, resulting in extensive mucinous dissemination and peritoneal metastases [11]. Clinically, appendiceal malignancies commonly present as acute appendicitis, although incidental detection during surgery, pelvic abscess, GI symptoms, and bowel obstruction have also been described [4,5]. In the present case, the patient had a prior history of acute appendicitis, for which appendiceal biopsy was performed; however, histopathological examination revealed only nonspecific inflammatory changes, with no evidence of malignancy. The original histopathology slides or blocks were unavailable for re-review; therefore, the possibility that an occult appendiceal malignancy was missed at that time cannot be completely excluded. This limitation illustrates an important diagnostic challenge associated with appendiceal neoplasms, particularly when they initially mimic benign inflammatory disease.

Bilateral ovarian involvement in appendiceal mucinous adenocarcinoma is well recognized and may closely resemble primary ovarian malignancy, creating substantial diagnostic difficulty [12]. Differentiating primary appendiceal mucinous neoplasms from primary ovarian mucinous tumors is particularly challenging in advanced or clinically complex cases. Preoperative evaluation is frequently inconclusive because GI endoscopy has limited sensitivity for appendiceal lesions [9,12], and currently available tumor

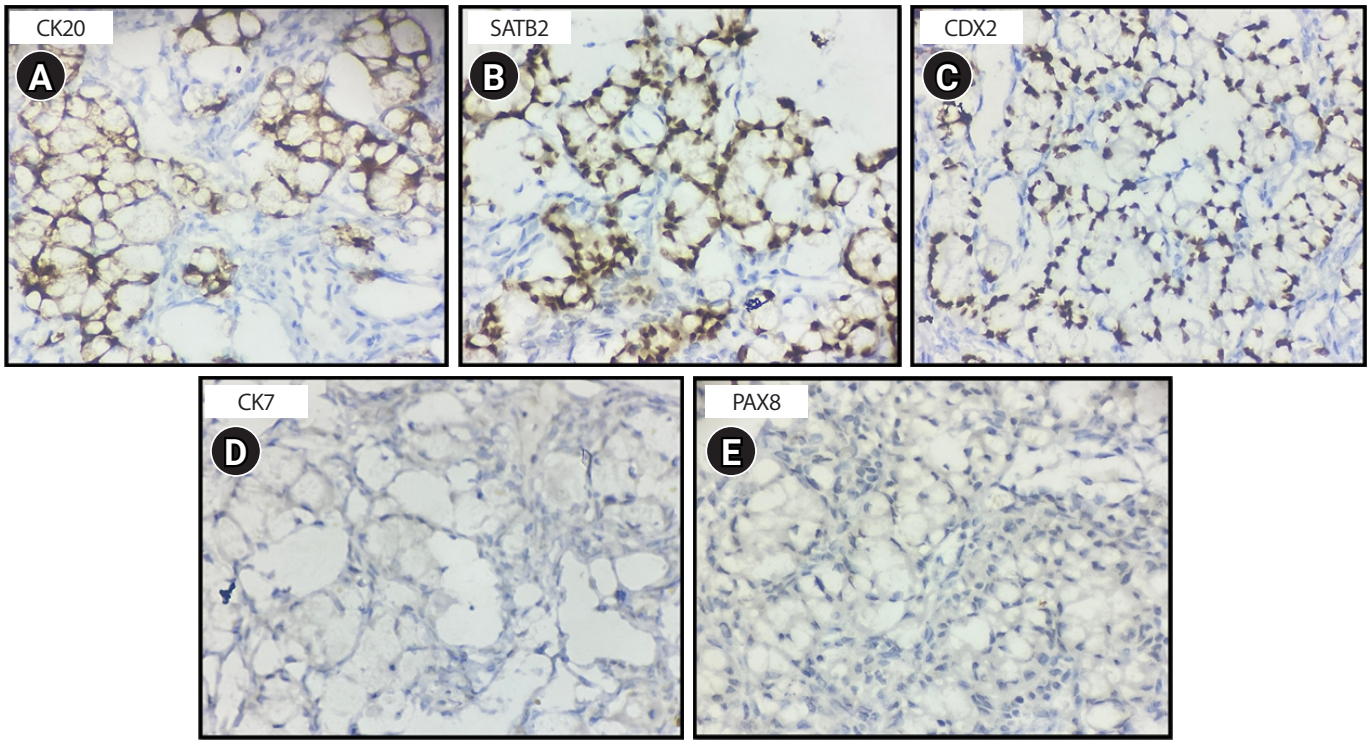

Fig. 4. Immunohistochemical analysis. (A) Immunohistochemical (IHC) staining showing diffuse cytoplasmic positivity for cytokeratin 20 (CK20). (B) IHC staining showing strong nuclear positivity for special AT-rich sequence-binding protein 2 (SATB2) in tumor cells. (C) IHC staining showing strong nuclear positivity for caudal-type homeobox 2 (CDX2) in tumor cells. (D) IHC staining showing absence of cytokeratin 7 (CK7) expression in tumor cells. (E) IHC staining showing absence of paired-box gene 8 (PAX8) expression in tumor cells.

biomarkers, including CEA, CA 19-9, and CA-125, lack specificity because they may be elevated in both GI and ovarian malignancies [4]. Moreover, metastatic appendiceal mucinous adenocarcinomas can mimic primary ovarian mucinous carcinomas in clinical presentation, imaging characteristics, and gross morphology, often requiring definitive histopathological and IHC evaluation for accurate diagnosis [4,12]. Notably, emerging evidence indicates that true primary mucinous ovarian carcinomas constitute only a small proportion, approximately 3%, of ovarian malignancies, supporting the view that many mucinous ovarian tumors are metastatic in origin [13].

Clinically, patients often present with vague, nonspecific abdominal symptoms and imaging findings suggestive of advanced ovarian cancer. These features further complicate preoperative differentiation because appendiceal primaries are rare and radiological findings are often nonspecific [4]. The absence of GI symptoms, together with abdominal distension and elevated CA-125 levels, may further favor an erroneous diagnosis of primary ovarian cancer [10]. In many cases, ovarian metastases become clinically apparent before the primary tumor is identified, which may delay determination of the tumor origin and selection of the most appropriate management strategy [5]. Typical presenting complaints include abdominal pain (42%), postmenopausal bleeding (18%), and abdominal bloating (15%), whereas only a minority of patients have symptoms directly attributable to the primary lesion [5,14]. Although bilateral ovarian masses may raise suspicion for metastatic disease, similar findings may also occur in some primary ovarian tumors, including undifferentiated and serous carcinomas, underscoring the need for comprehensive pathological evaluation [5,15,16].

In the present case, the patient presented with an abdominal mass accompanied by vague symptoms, including abdominal pain, distension, and loss of appetite, without altered bowel habits or rectal bleeding. The initial appendiceal biopsy showed only nonspecific inflammation, and both upper GI endoscopy and colonoscopy were unremarkable, further complicating preoperative diagnosis. Consequently, NACT followed by interval debulking surgery was considered, as is commonly recommended for advanced ovarian tumors [17]. However, the patient did not have a satisfactory response to neoadjuvant therapy, prompting further evaluation and revision of the diagnosis.

The presence of signet-ring cells in appendiceal tumors, even in

small proportions, has been consistently associated with aggressive tumor biology and poorer survival outcomes [18,19]. For appropriately selected patients with peritoneal dissemination, cytoreductive surgery combined with hyperthermic intraperitoneal chemotherapy (CRS-HIPEC) remains an important treatment strategy; outcomes are influenced by disease burden, completeness of cytoreduction, histological subtype, and tumor biology [7]. In the present case, surgery was performed for presumed advanced ovarian malignancy on the basis of the clinical, radiological, and intraoperative findings. Because the final histopathological diagnosis of appendiceal mucinous adenocarcinoma was not known at the time of surgery, CRS-HIPEC was not considered. After definitive histopathological and IHC confirmation, the patient was managed with systemic chemotherapy. Current systemic treatment for advanced appendiceal adenocarcinoma is largely extrapolated from colorectal cancer protocols and commonly includes regimens such as FOLFOX or FOLFIRI, with or without targeted agents such as bevacizumab or cetuximab [20].

In conclusion, this case highlights the diagnostic challenge posed by appendiceal mucinous adenocarcinoma presenting as bilateral ovarian masses and clinically mimicking advanced primary ovarian malignancy. The absence of GI symptoms, nonspecific imaging findings, and elevated CA-125 levels initially supported a gynecologic primary tumor, leading to NACT; however, the lack of therapeutic response prompted further evaluation. A definitive diagnosis was achieved only after histopathological examination and IHC supported a diagnosis of metastatic mucinous adenocarcinoma involving both ovaries, most consistent with an appendiceal primary. This case underscores the importance of considering secondary ovarian tumors in patients with bilateral mucinous ovarian masses, particularly when tumor markers such as CEA are markedly elevated or the clinical response is atypical.

ORCID

Naina Kumar: https://orcid.org/0000-0002-5970-6935
Gunvanti Rathod: https://orcid.org/0000-0002-1045-8707
Annapurna Srirambhatla: https://orcid.org/0000-0003-0164-5751
Mishu Mangla: https://orcid.org/0000-0003-0708-1037
Nireesha Bukke: https://orcid.org/0009-0000-8510-4594
Pooja T. Rathod: https://orcid.org/0009-0005-5709-3417

Authors' contribution

Conceptualization: NK. Literature search: NK. Data collection: NK, GR, AS, MM, NB, PTR. Formal analysis: NK, GR, AS, MM, NB, PTR. Writing–original draft: NK. Writing–review and editing: NK, GR, AS, MM, NB, PTR. Final approval of the manuscript: all authors.

Conflict of interest

No potential conflict of interest relevant to this article was reported.

Funding

None.

Data availability

Not applicable.

Acknowledgments

None.

Supplementary materials

None.

References

1. Dundr P, Singh N, Nožičková B, Němejcová K, Bártů M, Stružinská I. Primary mucinous ovarian tumors vs. ovarian metastases from gastrointestinal tract, pancreas and biliary tree: a review of current problematics. Diagn Pathol 2021;16:20. https://doi.org/10.1186/s13000-021-01079-2
2. Kawecka W, Pasnik I, Adamiak-Godlewska A, Semczuk M, Tyczynska M, Semczuk A. How to differentiate primary mucinous ovarian tumors from ovarian metastases originating from primary appendiceal mucinous neoplasms: a review. Pathol Oncol Res 2025;31:1612066. https://doi.org/10.3389/pore.2025.1612066
3. Yu Y, Wang T, Yuan Z, Lin W, Yang J, Cao D. Misdiagnosed appendiceal mucinous neoplasms and primary ovarian mucinous tumors present with different pre- and intraoperative characteristics. Front Oncol 2022;12:966844. https://doi.org/10.3389/fonc.2022.966844
4. Perivoliotis K, Christodoulidis G, Samara AA, Sgantzou IK, Floros T, Volakakis G, Karasavvidou F, Tepetes K. Low-grade appendiceal mucinous neoplasm (LAMN) primarily diagnosed as an ovarian mucinous tumor. Case Rep Surg 2021;2021:5523736. https://doi.org/10.1155/2021/5523736
5. Lin CW, Peng SL, Wang SH, Wu PY. A case report of appendiceal adenocarcinoma without gastrointestinal evidence mimicking primary ovarian cancer. J Int Med Res 2022;50:3000605221088559. https://doi.org/10.1177/03000605221088559
6. Zhang JJ, Cao DY, Yang JX, Shen K. Ovarian metastasis from nongynecologic primary sites: a retrospective analysis of 177 cases and 13-year experience. J Ovarian Res 2020;13:128. https://doi.org/10.1186/s13048-020-00714-8
7. Strach MC, Sutherland S, Horvath LG, Mahon K. The role of

chemotherapy in the treatment of advanced appendiceal cancers: summary of the literature and future directions. Ther Adv Med Oncol 2022;14:17588359221112478. https://doi.org/10.1177/17588359221112478

8. Dsouza R, Osueni A, Menon G. Appendiceal tumors [Internet]. StatPearls Publishing; 2025 [cited 2026 Feb 6]. Available from: https://www.ncbi.nlm.nih.gov/books/NBK555943/
9. Leonards LM, Pahwa A, Patel MK, Petersen J, Nguyen MJ, Jude CM. Neoplasms of the appendix: pictorial review with clinical and pathologic correlation. Radiographics 2017;37:1059-1083. https://doi.org/10.1148/rg.2017160150
10. Boyajian H, Majeski V, Flores A, Sturtz D, Baidoun F, Dughayli M. Clinicopathological and Perioperative Outcome of Appendiceal Tumors: Case Review of 31 Patients. Spartan Med Res J 2020;5:13487.
11. Carr NJ, Bibeau F, Bradley RF, Dartigues P, Feakins RM, Geisinger KR, Gui X, Isaac S, Milione M, Misdraji J, Pai RK, Rodriguez-Justo M, Sobin LH, van Velthuysen MF, Yantiss RK. The histopathological classification, diagnosis and differential diagnosis of mucinous appendiceal neoplasms, appendiceal adenocarcinomas and pseudomyxoma peritonei. Histopathology 2017;71:847-858. https://doi.org/10.1111/his.13324
12. Zhang W, Tan C, Xu M, Wu X. Appendiceal mucinous neoplasm mimics ovarian tumors: challenges for preoperative and intraoperative diagnosis and clinical implication. Eur J Surg Oncol 2019;45:2120-2125. https://doi.org/10.1016/j.ejso.2019.08.004
13. Yemelyanova AV, Vang R, Judson K, Wu LS, Ronnett BM. Distinction of primary and metastatic mucinous tumors involving the ovary: analysis of size and laterality data by primary site with reevaluation of an algorithm for tumor classification. Am J Surg Pathol 2008;32:128-138. https://doi.org/10.1097/PAS.0b013e3180690d2d
14. Lobo J, Machado B, Vieira R, Bartosch C. The challenge of diagnosing a malignancy metastatic to the ovary: clinicopathological characteristics vary and morphology can be different from that of the corresponding primary tumor. Virchows Arch 2017;470:69-80. https://doi.org/10.1007/s00428-016-2029-3
15. Foti PV, Attinà G, Spadola S, Caltabiano R, Farina R, Palmucci S, Zarbo G, Zarbo R, D'Arrigo M, Milone P, Ettorre GC. MR imaging of ovarian masses: classification and differential diagnosis. Insights Imaging 2016;7:21-41. https://doi.org/10.1007/s13244-015-0455-4
16. Willmott F, Allouni KA, Rockall A. Radiological manifestations of metastasis to the ovary. J Clin Pathol 2012;65:585-590. https://doi.org/10.1136/jclinpath-2011-200390
17. Vergote I, Coens C, Nankivell M, Kristensen GB, Parmar MKB, Ehlen T, Jayson GC, Johnson N, Swart AM, Verheijen R, McCluggage WG, Perren T, Panici PB, Kenter G, Casado A, Mendiola C, Stuart G, Reed NS, Kehoe S; EORTC; MRC CHORUS study investigators. Neoadjuvant chemotherapy versus debulking surgery in advanced tubo-ovarian cancers: pooled analysis of individual patient data from the EORTC 55971 and CHORUS trials. Lancet Oncol 2018;19:1680-1687. https://doi.org/10.1016/S1470-2045(18)30566-7
18. Levinsky NC, Morris MC, Wima K, Sussman JJ, Ahmad SA, Cloyd JM, Kimbrough C, Fournier K, Lee A, Dineen S, Dessureault S, Veerapong J, Baumgartner JM, Clarke C, Zaidi MY, Staley CA, Maithel SK, Leiting J, Grotz T, Lambert L, Hendrix RJ, Ronnekleiv-Kelly S, Pokrzywa C, Raoof M, Eng OS, Johnston FM, Greer J, Patel SH. Should we be doing cytoreductive surgery with HIPEC for signet ring cell appendiceal adenocarcinoma?: a study from the US HIPEC Collaborative. J Gastrointest Surg 2020;24:155-164. https://doi.org/10.1007/s11605-019-04336-4
19. Solomon D, DeNicola N, Feingold D, Liu PH, Aycart S, Golas BJ, Sarpel U, Labow DM, Magge DR. Signet ring cell features with peritoneal carcinomatosis in patients undergoing cytoreductive surgery and hyperthermic intraperitoneal chemotherapy are associated with poor overall survival. J Surg Oncol 2019;119:758-765. https://doi.org/10.1002/jso.25379
20. Hoehn RS, Rieser CJ, Choudry MH, Melnitchouk N, Hechtman J, Bahary N. Current management of appendiceal neoplasms. Am Soc Clin Oncol Educ Book 2021;41:1-15. https://doi.org/10.1200/EDBK_321009

eISSN: 2234-2591
Open Access

Case report

Ewha Med J 2026;49(3):e23
https://doi.org/10.12771/emj.2026.01459

The Ewha Medical Journal

Pneumocephalus with suspected cerebrospinal fluid leakage after epiduroscopic epidural neuroplasty: a case report

Min Jeong Kang, Bo Kyung Kang, Seung Hee Yoo, Won-joong Kim*

Department of Anesthesiology and Pain Medicine, Ewha Womans University Mokdong Hospital, Ewha Womans University College of Medicine, Seoul, Korea

Pneumocephalus is a rare complication of neuraxial procedures and is usually associated with inadvertent dural puncture or the use of air during epidural space identification. Epiduroscopic epidural neuroplasty (EEN) is performed without air injection and permits direct visualization of the epidural space; therefore, pneumocephalus after this procedure is extremely uncommon. A 71-year-old woman with a history of lumbar spine surgery underwent EEN via a caudal approach without sedation. No dural puncture was identified during the procedure. Approximately 12 hours later, she developed a non-orthostatic headache. Brain computed tomography revealed pneumocephalus in the basal cistern and left lateral ventricle. Her symptoms improved with oxygen therapy but worsened 5 days later despite radiologic resolution of the pneumocephalus. Suspected cerebrospinal fluid (CSF) leakage was treated with an epidural blood patch, which resolved her symptoms. Pneumocephalus may occur after EEN without clinically or endoscopically recognized dural injury and may coexist with CSF leakage; an occult microdural defect cannot be excluded as the underlying mechanism. Prompt imaging should be considered in patients who develop early or atypical postprocedural headache.

Keywords: Pneumocephalus; Neuroplasty; Epidural space; Cerebrospinal fluid leakage; Epidural blood patch; Case reports

Introduction

Pneumocephalus is a rare but recognized complication of neuraxial procedures and is most often associated with inadvertent dural puncture or the use of air during epidural space identification with the loss-of-resistance technique. Most reported cases have occurred after epidural anesthesia or epidural steroid injection when air was introduced into the epidural space [1-6].

Epiduroscopic epidural neuroplasty (EEN) differs from conventional epidural techniques because it is typically performed without air injection and permits direct visualization of the epidural space during catheter manipulation and adhesiolysis [7]. Accordingly, pneumocephalus after EEN is considered extremely uncommon, particularly when no dural puncture is recognized.

Only a limited number of reports have described pneumocephalus after epiduroscopic procedures [8], and most previously reported cases involved identifiable procedural factors, such as suspected dural violation or air entry during epidural space localization.

Here, we report a case of early-onset headache associated with intracranial pneumocephalus after EEN in a patient with multiple prior lumbar spine surgeries. No dural puncture was identified during epiduroscopic or fluoroscopic evaluation, and the patient subsequently required an epidural blood patch, suggesting concurrent cerebrospinal fluid (CSF) leakage.

Case presentation

Ethics statement

Informed consent for publication was obtained from the patient.

Patient information

A 71-year-old woman with a medical history of hypertension, diabetes mellitus, and thyroid cancer presented with chronic low back pain and persistent bilateral radicular symptoms that were

*Corresponding email: ickypoo@ewha.ac.kr
Received: May 4, 2026 Revised: June 17, 2026 Accepted: July 3, 2026

refractory to conservative treatment. She had undergone 3 prior lumbar spine surgeries, the most recent of which had been performed 2 years earlier.

Clinical findings

Lumbar spine magnetic resonance imaging showed postoperative changes after posterior decompression at L4–5 and lumbar scoliosis, along with multilevel degenerative changes. Diffuse disc bulging was observed at L1–2 and L3–4. At L2–3, a moderate left central-to-subarticular disc protrusion was identified, with associated left lateral recess stenosis. At L4–5, a presumed right subarticular disc herniation had decreased in size and T2 hyperintensity, with persistent right lateral recess stenosis. Facet joint arthropathy and thickening of the ligamentum flavum were also noted throughout the lumbar spine. Based on these findings and the clinical suspicion of epidural adhesions related to prior surgeries, EEN was planned.

Timeline

The procedure was performed without sedation to permit continuous communication with the patient and to monitor for signs of dural irritation. It was conducted via a caudal approach under fluoroscopic guidance. An epiduroscope was advanced into the epidural space, and bilateral adhesiolysis was performed at L3–5. Medication and saline were administered through the working channel. Saline was delivered intermittently by hand injection at approximately 1 mL/sec, with a total volume of less than 100 mL, including both intraoperative irrigation and postprocedural catheter injection, over a total procedure time of 45 minutes. No loss-of-resistance technique using air was employed, and no definite dural puncture was identified on epiduroscopic or fluoroscopic evaluation. The procedure was completed as planned, and the patient reported no headache or discomfort during the procedure.

Approximately 12 hours later, the patient developed a severe, non-orthostatic headache that persisted even in the supine position. Brain computed tomography (CT) was performed to differentiate CSF leakage from other intracranial complications and revealed intracranial air in the basal cistern and left lateral ventricle, consistent with pneumocephalus (Fig. 1). The patient was treated with supplemental oxygen, hydration, and urinary Foley catheterization for close urine-output monitoring. Her symptoms gradually improved without neurologic sequelae, and she was discharged after clinical improvement.

Follow-up and outcomes

Five days after the procedure, the patient returned to the emergency department with worsening headache. The headache was diffuse, involved the entire head, and had a pressing and lancinating quality, with a numeric rating scale score of 8/10. The pain did not clearly improve in the supine position and showed no definite positional variation. Associated symptoms, including neck stiffness, nausea, tinnitus, and dizziness, were absent. Follow-up brain CT demonstrated resolution of the pneumocephalus (Fig. 2). Conservative management was attempted initially; however, because the headache persisted and CSF leakage was suspected, an

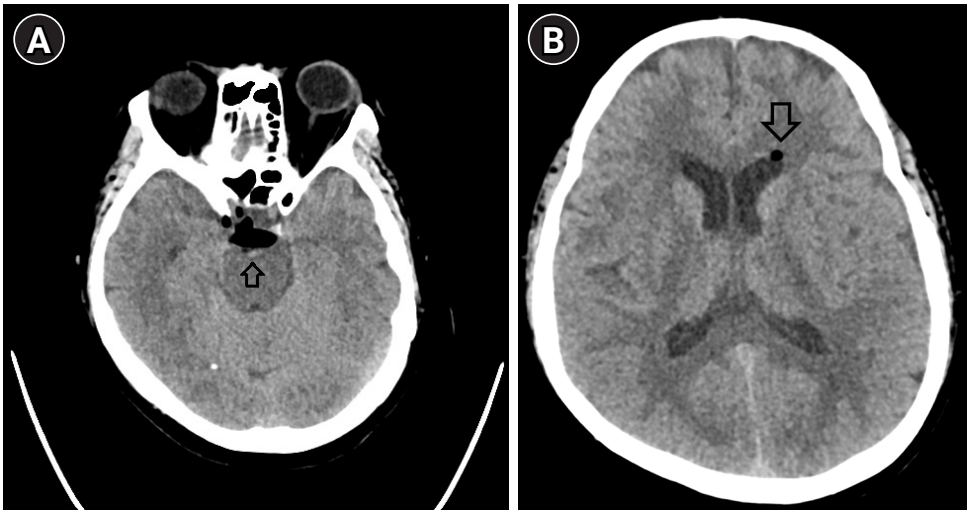

Fig. 1. Brain computed tomography (CT) obtained approximately 12 hours after epiduroscopic epidural neuroplasty. (A) Axial CT at the level of the basal cistern showing hypodense air collections in the interpeduncular cistern, consistent with pneumocephalus (arrow). (B) Axial CT at the level of the lateral ventricles showing a small hypodense air bubble in the anterior horn of the left lateral ventricle (arrow).

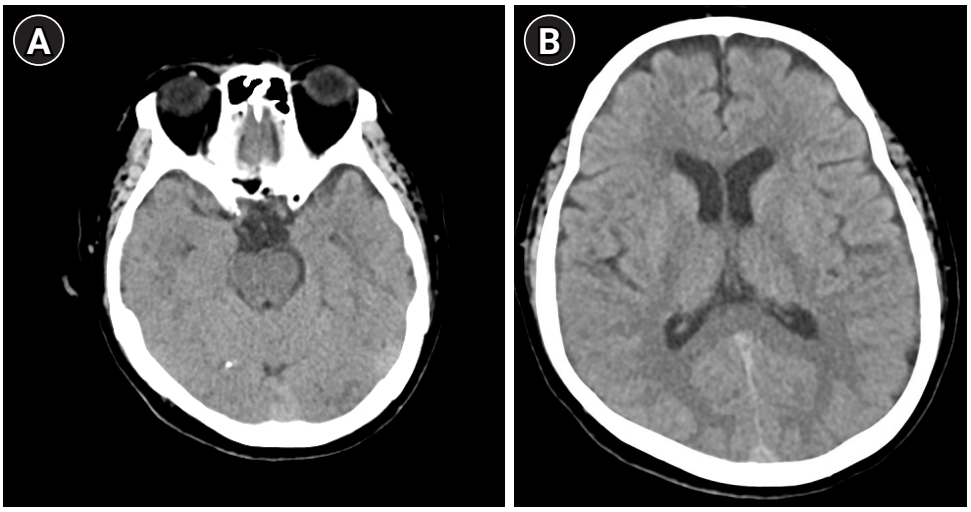

Fig. 2. Follow-up brain computed tomography (CT) obtained 5 days after the initial study. (A) Axial CT at the level of the basal cistern showing complete resolution of the previously noted pneumocephalus. (B) Axial CT at the level of the lateral ventricles showing resolution of the intraventricular air at the corresponding level.

epidural blood patch was performed via a lumbar approach targeting the L5–S1 interspace with approximately 20 mL of autologous blood, resulting in symptom improvement.

Discussion

Pneumocephalus after EEN is extremely uncommon, and very few cases have been described in the published literature. To the best of our knowledge, the most relevant prior publication is a review with an accompanying case report by Marchesini et al. [8].

A distinguishing feature of this case, compared with previous reports [8], is the absence of sedation and intraoperative symptoms. Sedation, such as propofol, may mask patient responses to dural irritation; however, the patient remained fully awake and reported no discomfort during the procedure. This finding suggests that a microdural defect, possibly caused by increased mechanical resistance from prior surgical adhesions, may allow air migration without immediate clinical signs [8,9]. Although no dural puncture was identified on epiduroscopic or fluoroscopic evaluation, an occult microdural defect below the detection limits of these modalities cannot be excluded and may represent the shared pathway through which both intracranial air migration and CSF leakage occurred in this case.

The patient had undergone 3 prior lumbar spine surgeries and demonstrated multilevel degenerative changes with suspected epidural fibrosis. Extensive epidural adhesions may increase mechanical resistance during catheter manipulation and adhesiolysis, thereby increasing the risk of microscopic dural injury even when no dural puncture is visible. Previous studies have suggested that epidural fibrosis after repeated spinal surgery alters normal epidural anatomy and increases procedural difficulty during epiduroscopy, potentially predisposing patients to unintended dural microinjury [8,10].

Unlike previously reported cases associated with air use, the present case occurred without any air-based technique. Residual air in the epiduroscope working channel or irrigation system may have entered the subarachnoid space through an occult microdural defect that was undetectable by endoscopy or fluoroscopy. Even a small volume of air can migrate intracranially because of pressure gradients generated during saline irrigation, particularly during multilevel adhesiolysis [8,9]. The epiduroscope working channel and irrigation system were flushed with saline before the procedure to remove residual air; however, complete air elimination cannot be guaranteed. The use of hand-injected saline irrigation and the possibility of residual air despite preprocedural flushing are consistent with the hypothesis that even small volumes of residual air, when delivered under intermittent pressure during multilevel adhesiolysis, may be sufficient to produce intracranial pneumocephalus. Conservative management with supplemental oxygen is commonly recommended because increasing the fraction of inspired oxygen accelerates nitrogen resorption and facilitates resolution of intracranial air [6].

Another notable feature of this case was delayed worsening of the headache several days after initial improvement. Follow-up imaging demonstrated decreased intracranial air, suggesting that pneumocephalus alone could not explain the recurrent symptoms. The recurrent headache lacked a definite orthostatic component and was not accompanied by neck stiffness, nausea, or tin-

nitus, which are features typically associated with intracranial hypotension. However, postural headache characteristics may be absent or atypical in intracranial hypotension [11]. The subsequent response to an epidural blood patch strongly supports the possibility of concomitant CSF leakage with intracranial hypotension [12]. Therefore, pneumocephalus and CSF leakage may coexist after EEN, even when no dural puncture is recognized endoscopically or fluoroscopically, and an occult microdural defect may serve as a shared pathway for both complications.

Postprocedural headache after EEN is commonly attributed to intracranial hypotension secondary to CSF leakage. However, this case demonstrates that pneumocephalus should also be considered, particularly when headache develops early or persists in the supine position [5]. In such cases, early brain imaging may be required to differentiate pneumocephalus from post-dural puncture headache [8].

This case also underscores the importance of close postprocedural monitoring after epiduroscopic adhesiolysis, especially in patients with multiple prior lumbar spine surgeries and suspected severe epidural fibrosis. Although EEN is generally considered safe and minimally invasive, unexpected complications, including intracranial air migration and CSF leakage, may occur even without recognized dural puncture [8]. Therefore, short-term inpatient observation may facilitate early detection and timely management of these complications. A key limitation of this case is that CSF leakage was not objectively confirmed by imaging or direct CSF pressure measurement; the diagnosis was based on clinical suspicion and the favorable response to the epidural blood patch.

ORCID

Min Jeong Kang: https://orcid.org/0009-0008-2378-9741
Bo Kyung Kang: https://orcid.org/0000-0003-2744-1044
Seung Hee Yoo: https://orcid.org/0009-0003-6152-6620
Won-joong Kim: https://orcid.org/0000-0003-2046-8690

Authors' contribution

Conceptualization: WK. Methodology: BKK, WK. Formal analysis: WK. Validation: WK. Project administration: SHY, WK. Writing–original draft: MJK. Writing–review & editing: WK.

Conflict of interest

No potential conflict of interest relevant to this article was reported.

Funding

None.

Data availability

Not applicable.

Acknowledgments

None.

Supplementary materials

None.

References

1. Singh S, Thakur H. Pneumocephalus after lumbar epidural. Med J Armed Forces India 2018;74:397-399. https://doi.org/10.1016/j.mjafi.2017.09.011
2. Kim WJ, Park HG, Park YH, Shin MR, Koo GH, Shin HY. Pneumocephalus during cervical transforaminal epidural steroid injections: a case report. Am J Phys Med Rehabil 2015;94:63-69. https://doi.org/10.1097/PHM.0000000000000165
3. Kasai K, Osawa M. Pneumocephalus during continuous epidural block. J Anesth 2007;21:59-61. https://doi.org/10.1007/s00540-006-0446-1
4. Park SK, Park SH, Lee BW, Cho WJ, Choi YS. Pneumocephalus following fluoroscopy-guided lumbar epidural injection in elderly patients: two cases report and a review of Korean literatures - Two cases report -. Anesth Pain Med (Seoul) 2020;15:492-497. https://doi.org/10.17085/apm.19087
5. Kim YD, Lee JH, Cheong YK. Pneumocephalus in a patient with no cerebrospinal fluid leakage after lumbar epidural block: a case report. Korean J Pain 2012;25:262-266. https://doi.org/10.3344/kjp.2012.25.4.262
6. Castedo J, Ferreira AP, Camacho Ó. Hyperbaric oxygen therapy in the treatment of pneumocephalus associated with epidural block: case report. Braz J Anesthesiol 2021;71:295-298. https://doi.org/10.1016/j.bjane.2021.02.058
7. Yıldırım HU, Akbas M. Percutaneous and endoscopic adhesiolysis. Agri 2021;33:129-141. https://doi.org/10.14744/agri.2020.70037
8. Marchesini M, Flaviano E, Bellini V, Baciarello M, Bignami EG. Complication of epiduroscopy: a brief review and case report. Korean J Pain 2018;31:296-304. https://doi.org/10.3344/kjp.2018.31.4.296
9. Farshad M, Schader JF, Stauffer A, Zipser CM, Kheram N, Spirig JM, Fasser MR, Widmer J, Hagel V. Intra-, epidural and intracranial pressure changes during interlaminar endoscopy, with and without dural tear. Neurospine 2025;22:583-591. https://doi.org/10.14245/ns.2550456.228
10. Bosscher HA, Heavner JE. Incidence and severity of epidural fi-

brosis after back surgery: an endoscopic study. Pain Pract 2010; 10:18-24. https://doi.org/10.1111/j.1533-2500.2009.00311.x
11. Kang K, Kim BK. Neurological symptoms of intracranial hypotension. J Korean Neurol Assoc 2019;37:117-122. https://doi.org/10.17340/jkna.2019.2.1
12. Safa-Tisseront V, Thormann F, Malassiné P, Henry M, Riou B, Coriat P, Seebacher J. Effectiveness of epidural blood patch in the management of post-dural puncture headache. Anesthesiology 2001;95:334-339. https://doi.org/10.1097/00000542-200108000-00012

eISSN: 2234-2591
Open Access

Images and solution

Ewha Med J 2026;49(3):e24
https://doi.org/10.12771/emj.2026.01445

The Ewha Medical Journal

Unrecognized tooth aspiration mimicking a hilar lesion in a patient with COVID-19 pneumonia

Pang-Yen Chen[1,2,3,4,5], Chien-Wei Chen[6,7], Yu-Jang Su[1,2,3,4,8*]

[1]*Department of Emergency Medicine, MacKay Memorial Hospital, Taipei, Taiwan*
[2]*Department of Nursing, Yuanpei University of Medical Technology, Hsinchu, Taiwan*
[3]*MacKay Junior College of Medicine, Nursing, and Management, Taipei, Taiwan*
[4]*Department of Medicine, MacKay Medical University, New Taipei City, Taiwan*
[5]*Institute of Biomedical Engineering, National Tsing Hua University, Hsinchu, Taiwan*
[6]*Department of Medical Imaging and Intervention, Linkou Chang Gung Memorial Hospital, Linkou, Taiwan*
[7]*College of Medicine, Chang Gung University, Taoyuan, Taiwan*
[8]*Toxicology Division, Emergency Department, MacKay Memorial Hospital, Taipei, Taiwan*

A 77-year-old nursing home resident with hypertension and chronic obstructive pulmonary disease presented to the emergency department with fever and dyspnea of 2 days' duration. No choking episode had been witnessed, and SARS-CoV-2 (severe acute respiratory syndrome coronavirus 2) testing was positive. On examination, he was tachypneic, with a respiratory rate of 32 breaths/min, an oxygen saturation of 88% on room air, and markedly diminished breath sounds over the left hemithorax.

Laboratory tests showed a white blood cell count of 6,900/μL with 15% band forms, a C-reactive protein level of 163 mg/L, and a procalcitonin level of 0.05 ng/mL. Arterial blood gas analysis while the patient was receiving 10 L/min of oxygen showed alkalemia, with a pH of 7.55, $PaCO_2$ of 43 mm Hg, and HCO_3^- of 36.5 mmol/L, as well as hypoxemia, with a PaO_2 of 71 mm Hg. A portable chest radiograph showed bilateral infiltrates and pleural effusions; it also showed hyperinflation of the left lung (Fig. 1). This unilateral hyperinflation was later attributed to a check-valve mechanism caused by the aspirated tooth in the left main bronchus: airflow entered the distal airways through the partially obstructed bronchus during inspiration, but expiratory airflow was impeded, causing air trapping. This radiographic pattern is a characteristic clue to foreign body aspiration. Thoracentesis yielded a sterile, lymphocyte-predominant transudative effusion, consistent with viral pleuritis and volume overload rather than empyema.

Despite treatment for coronavirus disease 2019 (COVID-19), severe hypoxemia and left-sided hypoventilation persisted. On hospital day 23, re-evaluation of the admission radiograph revealed a subtle radiopaque structure superimposed on the left hi-

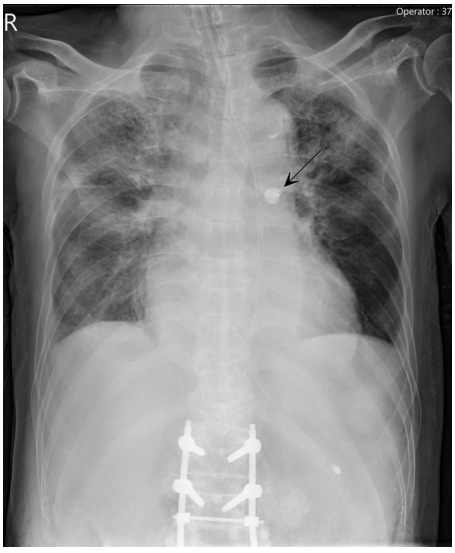

Fig. 1. A portable anteroposterior chest radiograph showing bilateral infiltrates and pleural effusions. A radiopaque foreign body (arrow) is visible over the left hilum, with hyperinflation of the left lung due to distal air trapping.

*Corresponding email: yjsu.5885@mmh.org.tw
Received: April 24, 2026 Revised: June 10, 2026 Accepted: July 3, 2026

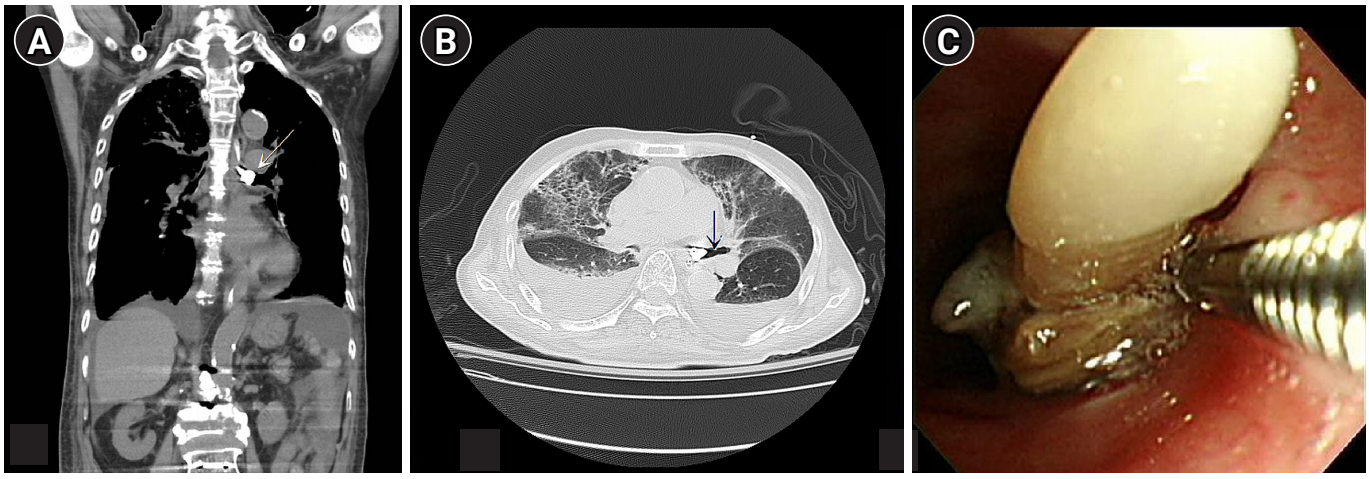

Fig. 2. Coronal chest computed tomography shows a tooth (arrow) causing complete obstruction of the left main bronchus with distal lung collapse (A). Lung-window imaging demonstrates air trapping compatible with a check-valve mechanism caused by the aspirated tooth (arrow) (B). Flexible bronchoscopy shows the tooth embedded in granulation tissue during retrieval (C).

lum (Fig. 1, arrow) that had initially been dismissed as benign calcification. Subsequent chest computed tomography showed an aspirated tooth in the left main bronchus, causing complete obstruction and atelectasis (Fig. 2A). Lung-window images demonstrated distal air trapping compatible with a check-valve mechanism caused by the aspirated tooth (Fig. 2B). Flexible bronchoscopy revealed the tooth embedded in granulation tissue (Fig. 2C). Removal briefly improved oxygenation, but the clinical course was complicated by postobstructive pneumonia, methicillin-resistant *Staphylococcus aureus* bacteremia, and multidrug-resistant *Acinetobacter baumannii* infection. The patient died on hospital day 106.

The requirement for informed consent was waived by the Institutional Review Board (IRB No. 202501221B0).

Foreign body aspiration in adults is frequently unwitnessed and may be diagnosed without a history of choking, particularly in older adults with dentures or diminished airway reflexes [1]. In this case, the aspirated tooth mimicked a calcified hilar lesion: projectional superimposition on a portable radiograph made the tooth resemble a calcified hilar lymph node.

The diagnostic delay was likely amplified by anchoring bias. After COVID-19 was confirmed, persistent hypoxemia was attributed to viral pneumonia, and the discordant bedside finding of asymmetric breath sounds was rationalized rather than investigated [2]. Persistent unilateral hypoventilation that is disproportionate to radiographic findings should prompt urgent evaluation for bronchial obstruction [3]. When clinical improvement stalls, deliberate repeat review of the initial imaging—with contrast and window settings adjusted to assess the central airways—may reveal a reversible cause before fatal complications develop.

ORCID

Pang-Yen Chen: https://orcid.org/0000-0002-5933-5820
Chien-Wei Chen: https://orcid.org/0000-0002-5085-9919
Yu-Jang Su: https://orcid.org/0000-0003-0218-1944

Authors' contribution

Conceptualization: PYC, YJS. Data curation: PYC, CWC. Investigation: PYC, CWC. Methodology: PYC. Validation: CWC. Project administration: YJS. Resources: CWC. Visualization: YJS. Supervision: YJS. Writing–original draft: PYC, CWC. Writing–review & editing: YJS.

Conflict of interest

No potential conflict of interest relevant to this article was reported.

Funding

None.

Data availability

Not applicable.

Acknowledgments

None.

Supplementary materials

None.

References

1. Hewlett JC, Rickman OB, Lentz RJ, Prakash UB, Maldonado F. Foreign body aspiration in adult airways: therapeutic approach. J Thorac Dis 2017;9:3398-3409. https://doi.org/10.21037/jtd.2017.06.137
2. Croskerry P. The importance of cognitive errors in diagnosis and strategies to minimize them. Acad Med 2003;78:775-780. https://doi.org/10.1097/00001888-200308000-00003
3. Pinto A, Scaglione M, Pinto F, Guidi G, Pepe M, Del Prato B, Grassi R, Romano L. Tracheobronchial aspiration of foreign bodies: current indications for emergency plain chest radiography. Radiol Med 2006;111:497-506. https://doi.org/10.1007/s11547-006-0045-0

eISSN: 2234-2591
Open Access

Correspondence

Ewha Med J 2026;49(3):e25
https://doi.org/10.12771/emj.2026.01158

The Ewha Medical Journal

Artificial intelligence as a pragmatic adjunct to molecular classification in endometrial cancer

Gunvanti Rathod[1*], Pragnesh Parmar[2]

[1]*Department of Pathology and Laboratory Medicine, All India Institute of Medical Sciences, Bibinagar, India*
[2]*Department of Forensic Medicine and Toxicology, All India Institute of Medical Sciences, Bibinagar, India*

If molecular classification defines the future of endometrial cancer (EC) care, artificial intelligence (AI) may determine how equitably that future is realized.

The advent of molecular classification has transformed the diagnosis and prognostication of EC. The 4 molecular subtypes defined by the Cancer Genome Atlas—*POLE* ultramutated, mismatch repair–deficient, p53-abnormal (p53abn), and no specific molecular profile (NSMP)—have substantial prognostic significance and are incorporated into the current World Health Organization and International Federation of Gynecology and Obstetrics classification systems [1,2]. Despite its clinical value, the implementation of molecular subtyping remains uneven, largely because of barriers to genetic testing in resource-limited settings, particularly in low- and middle-income countries [2].

In this context, AI applied to hematoxylin and eosin (H&E)–stained histopathological slides may serve as an effective bridge between morphology and molecular characterization. Advances in deep learning enable algorithms to identify complex architectural and cytological patterns associated with specific genomic alterations. Recent studies have demonstrated that AI can predict molecular subtypes from routine histopathology, indicating that morphologic correlates of genomic changes are reproducible and detectable [1,3]. Notably, these models extend beyond classification, showing potential to identify novel subgroups within established categories, particularly within the NSMP subtype [2,4]. However, the clinical utility of AI in EC depends not only on predictive performance but also on its integration into real-world workflows. To date, most studies have emphasized algorithmic accuracy, whereas implementation strategies remain insufficiently explored. To address this gap, we propose a structured approach in which AI is used to triage EC cases through computational pathology as a decision-support layer.

Under this framework, all EC cases would undergo an initial AI-based assessment of digital H&E-stained slides would generate outputs including probable molecular subtype and key biomarker status, such as mismatch repair status. Based on these outputs, cases can be stratified operationally according to prediction confidence. For cases with high-confidence predictions (probability >0.85), a provisional diagnosis may be assigned, with confirmatory testing reserved for situations in which treatment decisions require validation. For cases with intermediate confidence (0.60–0.85), targeted diagnostic testing, such as immunohistochemistry for mismatch repair deficiency and p53, can be performed. For cases with low-confidence predictions (probability <0.60), AI-based classification should be considered indeterminate, and comprehensive molecular evaluation using standard diagnostic methods should be undertaken to establish the molecular subtype.

Tiered diagnostic strategies offer several advantages, including more efficient resource allocation, reduced use of unnecessary tests, and shorter turnaround times. Importantly, diagnostic accuracy is preserved by ensuring that indeterminate cases undergo comprehensive molecular evaluation. Preliminary evidence suggests that such triage approaches may substantially reduce the number of molecular tests required without compromising clinical accuracy, particularly in high-volume centers [5-7].

*Corresponding email: gunvanti.path@aiimsbibinagar.edu.in
Received: February 5, 2026 Revised: April 20, 2026 Accepted: April 24, 2026

Table 1. Representative studies on AI-assisted molecular classification in endometrial cancer

Author (year)	Study design/cohort	AI approach	Molecular target	Key findings	Clinical implication
Qi et al. [1] (2025)	Multicenter cohort study (China)	Clinical-grade deep learning on whole-slide images	TCGA molecular subtypes	Achieved high accuracy for molecular subtyping using routine H&E slides	Demonstrates the feasibility of AI-assisted triage before molecular testing
Darbandsari et al. [2] (2024)	Multi-institutional retrospective study	AI-based histopathological image analysis	AI-defined molecular subsets	Identified a distinct, prognostically relevant AI-defined EC subgroup	Suggests that AI may uncover novel biological risk groups
Hong et al. [3] (2021)	Retrospective cohort	Multi-resolution deep learning models	Molecular features and EC subtypes	Successfully predicted molecular features from histopathological images	Provides early evidence supporting morphology-based molecular inference
Umemoto et al. [4] (2024)	Diagnostic accuracy study	Deep learning–based slide analysis	MMR status	Reliably predicted MMR deficiency from H&E slides	May serve as a screening tool for Lynch syndrome and molecular testing prioritization
Fremond et al. [6] (2023)	Multi-institutional validation study	Interpretable deep learning model	TCGA molecular classification	Generated explainable AI predictions from H&E slides	May improve clinical trust and adoption

AI, artificial intelligence; TCGA, The Cancer Genome Atlas; H&E, hematoxylin and eosin; EC, endometrial cancer; MMR, mismatch repair.

This framework may be particularly applicable in resource-constrained healthcare systems, where AI could function as a cost-effective gatekeeper by selectively directing the use of expensive molecular diagnostics. Implementation could involve a digital pathology platform integrated with a cloud-based AI system. In addition, affordable imaging solutions, such as portable slide scanners, may help address infrastructure limitations [8,9].

Several challenges must be addressed before clinical implementation of AI. First, the predominantly retrospective design of existing studies limits generalizability. Prospective multicenter trials are needed to validate real-world performance. Second, variability in tissue processing, staining, and slide digitization can introduce distributional shifts that adversely affect model performance on external datasets. Finally, model interpretability remains a critical concern [8,10]. Many deep learning systems function as "black boxes," generating predictions without transparent reasoning. Recent developments in interpretable AI aim to address this limitation and may facilitate clinical adoption [6].

Ethical and regulatory considerations are equally important. The use of AI in clinical diagnosis necessitates clear frameworks for accountability, validation, and oversight. The role of the pathologist must remain central, with AI functioning strictly as a decision-support tool rather than a replacement. Furthermore, equitable access to AI technologies must be ensured to prevent widening disparities based on patients' financial resources. Table 1 summarizes representative studies evaluating the role of AI in EC classification [1-4,6].

The proposed probability thresholds in this triage system should be considered flexible rather than fixed. These thresholds should be calibrated using institution-specific datasets that reflect local tumor characteristics and technical factors. Integration of AI algorithms with laboratory information systems and multidisciplinary tumor boards may further enhance diagnostic utility and facilitate clinical decision-making.

In summary, AI represents a promising and pragmatic adjunct to molecular classification in EC. Its primary value lies in enabling scalable, cost-effective risk stratification, particularly in settings where molecular testing is limited. A structured AI-assisted triage approach may optimize diagnostic workflows without compromising accuracy. Future efforts should prioritize implementation strategies that ensure equitable access and avoid exacerbating disparities in cancer care.

ORCID

Gunvanti Rathod: https://orcid.org/0000-0002-1045-8707
Pragnesh Parmar: https://orcid.org/0000-0002-8402-8435

Authors' contribution

Conception and design of the work: GR, PP. Conceptualization: GR. Literature review: GR, PP. Writing–original draft: GR, PP. Writing–review & editing: GR, PP. Accountability: GR, PP. Final approval of the article: GR, PP.

Conflict of interest

No potential conflict of interest relevant to this article was reported.

Funding

None.

Data availability

Not applicable.

Acknowledgments

None.

Supplementary materials

None.

References

1. Qi P, Yao T, Li H, Zhu J, Li J, Luo X, He Q, Li Y. Clinical-grade AI model for molecular subtyping of endometrial cancer: a multi-center cohort study in China. Mol Biomed 2025;6:102. https://doi.org/10.1186/s43556-025-00341-z
2. Darbandsari A, Farahani H, Asadi M, Wiens M, Cochrane D, Khajegili Mirabadi A, Jamieson A, Farnell D, Ahmadvand P, Douglas M, Leung S, Abolmaesumi P, Jones SJ, Talhouk A, Kommoss S, Gilks CB, Huntsman DG, Singh N, McAlpine JN, Bashashati A. AI-based histopathology image analysis reveals a distinct subset of endometrial cancers. Nat Commun 2024;15:4973. https://doi.org/10.1038/s41467-024-49017-2
3. Hong R, Liu W, DeLair D, Razavian N, Fenyö D. Predicting endometrial cancer subtypes and molecular features from histopathology images using multi-resolution deep learning models. Cell Rep Med 2021;2:100400. https://doi.org/10.1016/j.xcrm.2021.100400
4. Umemoto M, Mariya T, Nambu Y, Nagata M, Horimai T, Sugita S, Kanaseki T, Takenaka Y, Shinkai S, Matsuura M, Iwasaki M, Hirohashi Y, Hasegawa T, Torigoe T, Fujino Y, Saito T. Prediction of mismatch repair status in endometrial cancer from histological slide images using various deep learning-based algorithms. Cancers (Basel) 2024;16:1810. https://doi.org/10.3390/cancers16101810
5. Li L, Wang P, Geng C, Wang J, Cao L, Gao Y, Chen D, Qiao G, Zhang S, Feng N, Liu M, Li X, Ma Y, Zhang S, Xiao H, Jiang Z, Liu X, Ma W, Qi L. Histopathology images-based deep learning prediction of histological types in endometrial cancer. Cancer Med 2026;15:e71509. https://doi.org/10.1002/cam4.71509
6. Fremond S, Andani S, Barkey Wolf J, Dijkstra J, Melsbach S, Jobsen JJ, Brinkhuis M, Roothaan S, Jurgenliemk-Schulz I, Lutgens LC, Nout RA, van der Steen-Banasik EM, de Boer SM, Powell ME, Singh N, Mileshkin LR, Mackay HJ, Leary A, Nijman HW, Smit VT, Creutzberg CL, Horeweg N, Koelzer VH, Bosse T. Interpretable deep learning model to predict the molecular classification of endometrial cancer from haematoxylin and eosin-stained whole-slide images: a combined analysis of the PORTEC randomised trials and clinical cohorts. Lancet Digit Health 2023;5:e71-e82. https://doi.org/10.1016/S2589-7500(22)00210-2
7. Collins GS, Moons KG. Reporting of artificial intelligence prediction models. Lancet 2019;393:1577-1579. https://doi.org/10.1016/S0140-6736(19)30037-6
8. Bera K, Schalper KA, Rimm DL, Velcheti V, Madabhushi A. Artificial intelligence in digital pathology: new tools for diagnosis and precision oncology. Nat Rev Clin Oncol 2019;16:703-715. https://doi.org/10.1038/s41571-019-0252-y
9. Guo Q, Cui H, Zhang Y, Tang S, Yan W, Zhou X, Ding H, Zhou J, Ju X, Feng Z, Zhu J, Bai F, Zhong Y, Li H, Xu J, Wu X, Wang X, Wen H. An interpretable deep learning model for predicting endometrial cancer molecular subtypes from H&E-stained slides. NPJ Precis Oncol 2026;10:71. https://doi.org/10.1038/s41698-026-01280-w
10. Whangbo J, Lee YS, Kim YJ, Kim J, Kim KG. Predicting mismatch repair deficiency status in endometrial cancer through multi-resolution ensemble learning in digital pathology. J Imaging Inform Med 2024;37:1674-1682. https://doi.org/10.1007/s10278-024-00997-z